NTNU – Trondheim
Norwegian University of
Science and Technology

Calorimetry and exergy analysis in the context of renewable energy devices:

Supercapacitors and Solid State
Thermoelectric Devices

Hans Henrik R Hauge

Chemical Engineering and Biotechnology
Submission date: February 2014
Supervisor: Signe Kjelstrup, IKJ
Co-supervisor: Odne S. Burheim, HiST

Norwegian University of Science and Technology
Department of Chemistry

Declaration

I hereby declare that the work presented in this thesis has been produced independently by me in its entirety, and in agreement with the valid regulations given by the Norvegian University of Science and Technology (NTNU). I have also aknowledged all the sources of information which has been used in the thesis.

Trondheim, 18^{th} of February 2014

Hans Henrik Hauge

“ *You can’t be neutral on a moving train.* ”

Howard Zinn (1922 – 2010),

Abstract

The motivation for this master thesis is to establish methods for thermal characterization of technological devices necessary in a renewable energy society. More specifically in this thesis supercapacitors and thermoelectric generators have been investigated, using irreversible thermodynamics to descibe the observed device features.

In the experimental work regarding the analysis of supercapacitors, stacks of four Maxwell PC10 series supercapacitors, connected in series, were examined by means of isothermal calorimetery, measurements of the thermal conductivity of the constituent materials, and dissecations. Using a stack of four supercapacitors, instead of a single supercapacitor, gave access to the internal temperature gradient, without having to alter the internal configuration. Two models were developed in order to determine the effective thermal conductivity of the stack. The first model is based on the second degree temperature gradient, measured by thermocouples embedded between the supercapacitors, resulting in an effective thermal conductivity between $0.5\,\mathrm{WK^{-1}m^{-1}} < \lambda_{stack} < 1.0\,\mathrm{WK^{-1}m^{-1}}$, depending on the compaction pressure. The second model, based on summing the thermal resistivities of the constituent materials, revealed an effective thermal conductivity of $\lambda_{stack} = 0.53 \pm 0.06\,\mathrm{WK^{-1}m^{-1}}$. Studying the entropy production of the supercapacitors, the effective thermal conductivity, λ_{stack}, is found to be the decisive constructional factor, for minimizing the entropy production. The activated carbon material of the electrodes, was determined to be the constituent material with the highest contribution to the effective thermal resistivity of the device, and hence the loss of exergy in the energy storing process.

In the experimental procedures of thermoelectric modules, TEP-1264-1.5 modules supplied by Thermo-Gen AB, were investigated. In the experimental procedures, the obtainable temperature gradient within the calorimeter proved to be too small for load experiments, and polarization of the heat was found to cause uncompensatable uncertainty in the measurement of the heat fluxes through the device, thereby making e.g. the figure of merit an unobtainable value. From the experiments the Seebeck coefficient of the module was found to be $\eta_S = 37 \pm 7\,\mathrm{mVK^{-1}}$, and the isothermal ohmic resistance of the device was determined to increase linearly with the average temperature, described by $R = 1.394 \pm 0.007\,\overline{T}$, where the unit of the ohmic resistance is [Ω], and $\overline{T}$ is the average temperature across the device, in [$^\circ\mathrm{C}$]. Both results are in accordance with values obtained by Takla [2].

The most important mean, in order to further improve this type of experimental investigations of the energy devices, is to obtain higher precision in the heat flux through the interface between the calorimeter, and the respective devices.

Sammendrag

Motivasjonen for denne masteroppgaven er å etablere metoder for termisk karakterisering av teknologiske innretninger, som er nødvendige i et samfunn basert på fornybar energi. Mer spesifikt fokuserer denne oppgaven på å studere superkondensatorer og termoelektriske generatorer, ved å bruke irreversibel termodynamikk som beskrivelsesgrunnlag for de eksperimentelle observasjonene.

I den eksperimentelle analysen av superkondesatorer, ble sett på fire Maxwell PC10 serie superkondensatorer loddet sammen i serie, og deretter studert ved hjelp av isoterm kalorimetri, bestemmelse av den termiske ledningsevnen til superkondensatorenes delmaterialer, og dissekasjoner av enhetene. Ved å bruke fire superkondensatorer koblet i serie, ble tilgang på de interne temperaturgradientene til superkondensatorene oppnådd, uten å måtte endre den indre konfigurasjonen til de respektive kondensatorene. To modeller ble utviklet med hensyn på å bestemme den effektive termiske ledningsevnen til superkondensatorsettene. Den første modellen baserer seg på å bruke superkondensatorenes temperaturgradient i den aksiale retningen, til å finne den effektive termiske ledningsevnen, ved hjelp av en regressiv sum av minste kvadraters metode. Avhengig av kompresjonstrykket, ble den effektive termiske ledningsevnen til superkondensatorsettene, λ_{stack}, funnet å variere mellom $0.5\,\mathrm{WK^{-1}m^{-1}}$ og $1.0\,\mathrm{WK^{-1}m^{-1}}$, ved hjelp av denne metoden. Den andre modellen for bestemmelse av den effektive termiske ledningsevnen til superkondensatorsettene, baserer seg på å summere alle bidragene til den totale termiske resistansen til superkondensatorenes materialer. Den effektive termiske ledningsevnen til superkondensatorsettene ble med denne metoden bestemt til å være lik $\lambda_{stack} = 0.53 \pm 0.06\,\mathrm{WK^{-1}m^{-1}}$. Ved å studere entropiproduksjonsprosessene i superkondensatorene ble det dedusert at den termiske ledningsevnen til superkondensatormaterialene er den største bidragsyteren til entropiproduksjonen, med hensyn på superkondensatorenes design. Videre ble det funnet at det aktiverte karbonlaget, som utgjør superkondensatorenes elektroder, er det materialet som har det største bidraget til den termiske resistansen, og dermed også til tapet av eksergi i superkondensatorenes energilagringsprosess.

I den eksperimentelle analysen av termoelekriske generatorer ble TEP-1264-1.5 moduler, fra ThermoGen AB, benyttet. Den eksperimentelle analysen viste at den maksimalt oppnåelige temperaturgradienten inne i kalorimeteret var for liten til å kunne utføre eksperimenter med eksterne laster. Videre viste det seg at varmepolariseringen førte til en ukalibrerbar usikkerhet i bestemmelsen av varmestrømmene gjennom de termoelekriske generatorene. Dette medførte at effektivitetsenheter, som for eksempel "kvalitetsenheten"[1], Z, ikke kunne bestemmes. Fra eksperimenter ble Seebeck koeffisienten bestemt til å være lik $\eta_S = 37 \pm 7\,\mathrm{mVK^{-1}}$, og den isoterme interne ohmske motstanden ble funnet å variere lineært i henhold til likningen $R = 1.394 \pm 0.007\,\overline{T}$, der R er den ohmske motstanden i [Ω] og $\overline{T}$ er gjennomsnittstemperaturen på tvers av enheten i [$^\circ$C]. Begge resultatene samstemmer med tidligere bestemte verdier av Takla [2].

[1]= 'figure of merit'

Det viktigste tiltaket for å forbedre denne typen eksperimentelle studier av energienheter, har vist seg å være ved å øke presisjonen av bestemmelsen av varmestrømmen gjennom grenseflaten mellom kalorimeteret, og de respektive enhetene.

Project background

The overall goal of this master thesis is to investigate the heat and work produced by a supercapacitor stack, consisting of four Maxwell PC10-series supercapacitors, and a Be-Te Thermoelectric generators from Thermo-Gen AB. The work linked to the supercapaitors will be aimed at continuing, and improving, the experimental methods for studying the energy storing process of the respective devices, initiated by Hauge et al. [1]. The thermal conductivities of the activated carbon electrode material will also be studied, which is regarded a field of high novelty. The work concerning the thermoelectric generators, will consist in further investigating the calorimetric experiments described by Takla [2], though with higher precision and error estimates. Both experiments were to be conducted in a calorimeter designed by Burheim [3], and the theory is to be investigated using irreversible thermodynamics, as described by Kjelstrup et. al. [4].

Acknowledgements

In the context of the work related to the master thesis, there are several people I would like to thank. First, I would like to thank prof. Signe Kjelstrup, for being my superviser, and for her inputs on the theoretical aspects of the thesis. I would like to thank Roger Aarvik, for his exceptional help, supplying experimental equipment, and ordering the supercapacitors. I would like to thank Marit Takla Børset, for ordering the thermoelectric generators. Finally, but not least, I woluld like to thank my co-supervisor, dr. Odne S. Burheim, for all the coffee and time he has shared with me over the last year, and also for always being there for me when I have needed his expertise, regarding both theoretical approaches, and experimental procedures.

In the context of getting to a point where the master thesis could be written, there are some people that deserve a special thanks. First, I would like to thank my family for all their support up through the years. Secondly, I would like to thank all my fantastic friends, and also all the other interesting people I have gotten to know during the last 5.5 years, here in Trondheim. You have all made these years a joyful time.

List of Symbols

Table 1: List of Symbols (Part 1/2)

Roman symbols		
Symbol	Definition	Units
A	Area	m^2
C_1	Integrational constant	$-$
E	Electric field	$V\,m^{-1}$
h	Height	m
H_j	Partial molar enthalpy	$J\,mol^{-1}$
I	Current	A
j	Current density	$A\,m^{-2}$
J_j	Flux of component j	$mol\,m^{-2}\,s^{-1}$
J'_q	Flux of measurable heat	$J\,m^2\,s^{-1}$
J_q	Flux of internal energy	$J\,m^2\,s^{-1}$
J_s	Flux of entropy	$J\,K^{-1}\,m^2\,s^{-1}$
L_{ij}	Onsager coefficient	$-$
p	Pressure	bar
P	Effect	$J\,s^{-1}$
N_j	Number of moles of component j	mol
N	Number (constant)	$-$
q	Heat delivered to the system	J
q_0	Heat delivered to the surroundings	J
Q_{total}	Total heat	J
Q_{in}	Entering heat	J
$\dot{Q}$	Heat flux	$J\,s^{-1}$
r	Thermal resistance	$K\,m\,W^{-1}$
r_{total}	Total thermal resistance	$K\,m\,W^{-1}$
R	Ohmic resistance	Ω
s	Entropy per volume	$J\,K^{-1}\,m^3$
S	Entropy	$J\,K^{-1}$
$S*$	Transported entropy	$J\,K^{-1}\,mol^{-1}$
t	Time	s
T	Temperature	$K\,/^{\circ}\mathrm{C}$
T_i	Temperature at specified location	$K\,/^{\circ}\mathrm{C}$
T_0	Boundary temperature	$K\,/^{\circ}\mathrm{C}$

Table 2: List of Symbols (Part 2/2)

Symbol	Definition	Units
T_h	Hot temperature	K /°C
T_c	Cold Temperature	K /°C
$\overline{T}$	Average temperature	K /°C
u	Internal energy per volume	$J\,m^{-3}$
U	Potential energy density	J
$\dot{U}$	Internal energy flux	$J\,s^{-1}$
V	Volume	m^{-3}
w	width	m
w	Work	J
w_{ideal}	Ideal work	J
x	Axial location	m
X_i	Thermodynamic driving force	$-$
Z	Figure of merit	$-$
Greek symbols		
Symbol	Definition	Units
β	Compression factor	$-$
δ	Thickness	m
δ_i	Component thickness	m
η_S	Seebeck coefficient	$V\,K^{-1}$
η_I	First law efficiency	$-$
η_{II}	Second law efficiency	$-$
ϕ	Electric potential	V
γ	Factor for figure of merit	$-$
λ	Thermal conductivity	$W\,K^{-1}\,m^{-1}$
λ_i	Component material thermal conductivity	$W\,K^{-1}\,m^{-1}$
λ_{stack}	Effective thermal conductivity of stack	$W\,K^{-1}\,m^{-1}$
κ	Electric conductivity	$S\,m^{-1}$
Ω	Cross sectional area	m^2
π	Peltier heat	J
μ	Chemical potential	$J\,mol^{-1}$
μ_j	Component chemical potential	$J\,mol^{-1}$
σ	Entropy production	$J\,s^{-1}\,K^{-1}\,m^{-3}$
Σ	Sum	$-$
Thermodynamic expressions		
Symbol	Definition	Units
ΔS	Entropy change of the system	$J\,K^{-1}$
ΔS_0	Entropy change of the surroundings	$J\,K^{-1}$
ΔT_i	Change in temperature at interstitial position	K/°C
$\Delta T(x)$	Modelled change in temperature	K/°C
ΔT	Change in temperature	K/°C
$\left(\frac{dS_{irr}}{dt}\right)$	Total entropy production	$J\,K^{-1}\,s^{-1}$
$\Delta\phi$	Potential difference	V
$\Delta\phi_{j=0}$	Emf	V

Table 3: Symbols related to the basic physics of supercapacitors presented in section (2.1.1)

Symbol	Definition	Units
A	Area	m^2
C	Capacitance	F
d	Distance	m
E	Electric field	$V\,m^{-1}$
q	Charge	C
Q	Charge	C
U	Potential energy	J
V	Potential	V
ϵ	Permitivity	$F\,m^{-1}$
σ_s	Surface charge density	$C\,m^{-2}$

Constants

The Faraday constant: $F = 96\,485\,\mathrm{C\,mol^{-1}}$

The permitivity of empty space; $\epsilon_0 = 8.85 \times 10^{-12}\,\mathrm{F\,m^{-1}}$

Contents

List of Figures

List of Tables

Chapter 1

Introduction

Energy has always been, and will always be, an important part of people lifes. In order to understand the importance of the development of renewable energy devices, they will have to be put into context. The worlds population passed 7 billion people in 2012, is steadily increasing, and is estimated to pass 9 billion by year 2050 [8]. As more people are inhabiting the planet, the resources are also getting more scarce, and the effects of human influence is getting more pronounced. One of the most profound effects of anthropogenic activity follows the effects of the emissions of greenhouse gases, predominantly CO_2, into the atmosphere, as will be further enlighted in the following paragraphs. A dynamic relationship between population growth and CO_2 emissions is present [9]. As the world is steadily developing in terms of income per capita, the emissions of CO_2 show a corresponding positive trend. However, despite this positive trend it seems that countries in which the GDP per capita is accellerating, the corresponding emissions of CO_2 tend to decellerate. This could indicate that countries in which the income is high, the feeling of a need to do something about the emissions of greenhouse gases is greater, than in in countries that are still developing [10]. Another secondary problem about fossil fuels is that they will run out some time, as the resources are consumed faster than they are recreated. Hydrocarbon resources, such as natural gas, petroleum and coal, has historically constituted a major part of the global energy consumption, and this trend is expected to continue in the future, according to Papavinasam et al. [5].

The fifth assessment report on climate change developed by the United Nations Intergovermental Panel on Climate Change (IPCC) [7] is based on observational and model studies of temperature change, climate feedback, and changes in the Earth's energy budget which together provide confidence in the magnitude of global warming in responce to past and future radiative forcing. It states a number of climate effects clearly induced by human activity, and due to its importance some of the main results are presented in the following. One of the most pronounced effects of human ac-

tivity is the effect of our emissions of greenhouse gases has on the climate system. Our emissions cause a positive total radaitive forcing, leading to an uptake of energy by the ecosystem. The atmospheric concentration of CO_2 has increased with about 40 % since 1750, at the beginning of the Industrial Revolution. The increase in CO_2 concentration in primarely due to fossil fuel emissions and secondarily due to net land use change emissions. Together with methane and nitrous oxide the concentration of CO_2 are unprecedented in at least the past 800,000 years.

Since the 1950s many of the observed changes are unprecedented over the past decades to millenia. Each of the last three decades has been successively warmer global surface temperature than the preceding decade since 1850. The global combined land and ocean temperature has increased with about $0.89 \pm 0.19\,^{\circ}\mathrm{C}$ over the period from 1901 to 2012, and about $0.72 \pm 0.23\,^{\circ}\mathrm{C}$ over the period from 1951 to 2012. To put things in perspective the period from 1983 to 2012 was likely the warmest 30-year period over the last 1400 years in the Northern Hemisphere. However, most of the accumulated energy in the climate system is stored in the ocean, accounting for about 93 % of the energy accumulated between 1971 and 2010. Melting ice and warming of the continents both count for 3 % while warming of the atmosphere makes up for the remaining 1 %. Its regareded as virtually certain that the upper ocean, from the surface down to $700\,\mathrm{m}$, has warmed from 1971 to 2010, and it is likely that it has warmed between the 1870s and 1971. The warming of the ocean causes the ocean water to expand and, together with the melting of solid water, stored in glaciers, and ice sheets, it constitutes one of the two main contributions to the rise of sea level. Glaciers and ice sheets make part of the cryosphere, which is also changing dramatically. Over the last two decades some very evident changes has appeared; the Greenland and the Antarctic ice sheets have been loosing ice, Greenland so in an accellerating manner. Glaciers are melting all over the world, and the extent of both the arctic sea ice, and the snow cover in the Northern Hemisphere, has decreased. The rate of sea level rice the last 60 years exceeds the mean rate during the previous two millenia. The global mean sea level has rose by $0.19 \pm 0.02\,\mathrm{m}$ over the period 1901-2010.

The ocean has absorbed about 30 % of the emitted antropogenic CO_2, causing gradual ocean acidification, decreasing the pH of the ocean by 0.1 since the beginning of the Industrial Era. The decreased pH caused by the increased CO_2 concentration in the atmosphere also reduce the saturation state of bilogically important calcium carbonate, $CaCO_3$, especially argonite and calcite. Calcium carbonate is cruscial for calcifying organisms such as coral reef organisms, bivalves and picturesque plaktonic pteropods, and also mussels, oysters and clams, that use it to build their skeletons. This will lead to a change in habitat, favouring sea grass and non-calcifying algae beacause ocean accidification will make them grow faster, and generally outcompete other habitate-forming organisms. Another severe effect of ocean acidification is seen in tropical reef fish, showing indicatins of loss of the senses of sight, smell, and touch; leading to reduced survival. If this effect can be extrapolated to comercially important fish species, like e.g. cod and tunar, this could have a tremendous effect on the human food supply [11].

This is where we stand now, and the changes are still happening. Continued emissions of greenhouse gases will cause furter warming through all the parts of the climate system. In order to limit the climate change, substantial and sustained reductions in greenhouse gases are required. The downside is that even if we manage to stop the emissions of greenhouse gases, most of the aspects of climate change will persist for many centuries. During the 21^{st} century the ocean will continue to warm, and the warming will penetrate to deeper water, the sea level will continue to rise, and ocean acidification will also carry on. The Arctic sea ice cover, the snow cover in the Northern Hemisphere, and the global glacier volume will continue to decrease. As a last remark it should also be mentioned that the contrast in precipitation is expected to increase, making dry regions dryer and wet regions wetter, although there are some exceptions [7].

In other words; great damage has already been afflicted upon our living habitate - our task is to make the effect as small as possible. At the end of the movie *Chasing Ice* the fotographer and scientist James Balog states the following, after observing the rapid changes of the Greenland glaciers over several years: *You can't divorce civilization from nature - we totally depend on it*. In table (1.1) the estimated global mean surface temperature changes and the global mean sea level rise for various so-called Representative Concentration Pathways (RCPs) are displayed. All RCPs presented are considered possible, depending on how much greenhouse gases are emitted (their numbers refer to their corresponding radiative forcing values in 2100, relative to pre-industrial values, given in Wm^{-2}. For example if the continued emissions prove to follow the path leading to greenhouse gas concentrations corresponding to an increased radiative forcing of $6.0\,\mathrm{Wm}^{-2}$ in 2100 (relative to the pre-industrial values) a mean surface temperature change in the range $1.4 - 3.1\,^{\circ}\mathrm{C}$, and a global mean sea level rise in the range $0.33 - 0.62\,\mathrm{m}$, by the end of the century, is to be expected.

An important question is the following: Where do we turn to find better solutions for the future? The Earth has many sources of energy, and the way they are exploited depend on the nature of the source. Most of the energy sources derive from the sun, except for geothermal energy that originates from the formation of the planet and radioactive decay of minerals. Fossile fuels like oil, natural gas and coal derive from plants and animals that once inhabited the surface of the earth many million years ago. There are mainly two big problems with fossile fuels. The first problem is that we are consuming the resources faster than the resources are being recreated making this a unsustainable energy source, and secondly the combustion of hydrocarbons, creating water and CO_2 as the main products, has an undesirable effect on the climate. Much more renewable and green energy, with a much smaller impact on our surroundings, can be extracted from wind, waves, solar power, salt power, hydropower, geothermal energy, and some would also add nuclear power. Nuclear power generation remains a dominationg electricity source in many countries. The main problem with nuclear power is the danger these power plants constitute while operating, as experienced at Three Mile Island (USA) in 1979, in Tsjernobyl (Ukraine) in 1986 and in Fukuhima (Japan) in 2011. Other problems involve its economic necessity, the nuclear waste disposal and the proliferation risk increasing the possibility

Table 1.1: Projected change in global mean surface air temperature and global mean sea level rise for the mid- and late 21^{st} century. All RCPs presented are considered possible, depending on how much greenhouse gases are emitted (their numbers refer to their corresponding radiative forcing values in 2100, relative to pre-industrial values, given in Wm^{-2} [7].

Variable	**Scenario**	**2046–2065**		**2081–2100**	
		Mean	Likely range	Mean	Likely range
Global Mean Surface Temperature Change [$^{\circ}$C]	RCP 2.6	1.0	0.4–1.6	1.0	0.3–1.7
	RCP 4.5	1.4	0.9–2.0	1.8	1.1–2.6
	RCP 6.0	1.3	0.8–1.8	2.2	1.4–3.1
	RCP 8.5	2.0	1.4–2.6	3.7	2.6–4.8
Global Mean Sea Level Rise [m]	RCP 2.6	0.24	0.17–0.31	0.40	0.26–0.54
	RCP 4.5	0.26	0.19–0.33	0.47	0.32–0.62
	RCP 6.0	0.25	0.18–0.32	0.47	0.33–0.62
	RCP 8.5	0.29	0.22–0.37	0.62	0.45–0.81

of nuclear warfare and de-stabilizing international relations. In Asia, and other developing regions in which the energy demand growth is rapid, and alternative energy sources are scarce, the energy supply security may be a high priority. Nuclear power can in such situations prove to be a decisive factor in maintaining a steady energy supply, and may also help reducing air pollution and greenhouse gas emissions, if the alternative is power plats, with fossil fuel as the energy source [12].

As energy is limited it is important to find better ways in which we use the energy to cover our needs. This implies both finding new solutions, but also making excisting solutions more effective, which will be uncovered in the following relevant examples regarding transportation and energy recouperation in industry.

Transportation today is largely dominated by combustion of fossil fuel as the energy source. Finding alternatives to fossil fuel would therefore have a tremendous effect on CO_2 emissions. Many alternatives have been tried out like e.g. biofuel, batteries, hybrids, and hydrogen. Two of these alternatives are especially interesting; battery electricity and hydrogen electricity, where the energy to the electric engine is obtained from batteries and hydrogen fuel cells, respectively. Fuel cell vehicles are believed to take a bigger share of the market as battery electric vehicles are taking a bigger and bigger market share from vehicles driven by internal combustion engines, and thereby forming a bridge for fuel cell vehicles [13]. Regarding battery electrical vehicles, a study using car trip diaries was carried out in 6 European countries, showing that the average driven distance ranged from 40 km (UK) to 80 km (Poland), and that the parking time after the last trip of the day reached more than 16 hours per day [14]. This is good news for the compatability of battery electric vehicles to the mobility patterns

of the potential users, as batteries require time to recharge. In Norway the trend seems to have started already, at least when studying the sales of new cars. Two battery electric cars made really good sales in 2013: Nissan Leaf was the third most sold car of the year, and Tesla Model S was the most sold car in December [15].

One obvious advantage of using electricity, depending on how you generate it, is that it has potential to be much cleaner with respect to emissions of CO_2, than corresponding vehicles driven on hydrocarbons. Another big advantage of using an electrical engine is that it can also be used as a generator, which is one of the applications supercapacitors are very well suited for. Supercapacitors are able to handle larger current densities than batteries, making them an excellent choice for recouperating the breaking energy of a vehicle, which in turn can be used for other means later, like e.g. to accellerate. When breaking the electric motor does most of the deceleration. Instead of a conventional friction-based breaking, the motor is running in a reverse mode, creating resistance that slows the vehicle down in a process similar to shifting down in a standard transmission vehicle. As the motor is running backwards it is also acting as an energy generator, converting the kinetic energy into electrical energy that can be stored in supercapacitors for future use. The use of regenerative breaking also reduces the load off mechanical breakes, reducing their maintenance costs [16].

Experiments have also been done, exploring using only supercapacitors as the energy source for the vehicle. One of these is projects take place in Shanghai, China, where 40 buses are equipped with supercapacitors. These supercapacitors are rapidly charged at each bus stop, through a connector in the roof, while the passangers are boarding the bus. The buses travel around a loop in the city and when fully charged, which takes couple of minutes at each bus stop, a bus is able to travel about $5\,\mathrm{km}$ at a maximum speed of $44\,\mathrm{km/h}$. This means that this technology is not yet applicable for large distances between the charging stations, but for urban purposes they are very well suited. The buses are of course also eqipped with a regenerative breaking system recovering up to $40\,\%$ of the breaking energy. Compared to conventional diesel buses the supercapacitor buses are expected to have one-tenth the energy cost and save up to $200,000\,\$$ on fuel during their 12 year lifetime (based on the prices on electricity and diesel in 2009) [17, 18].

Ragone plots are very well suited for comparing energy storage devices like batteries and capacitors. In a Ragone plot the energy storage devices are plotted in log-log diagram with the power density (in W/kg) and the energy density (in Wh/kg) available for a load along the primary and secondary axis, respectively. As can be seen from figure (1.1) batteries and capacitors prove to be diametrically opposite. Batteries have high energy densities (about $10^5\,\mathrm{Wh/kg}$) but low power densities ($100\,\mathrm{W/kg}$), while capacitors have low energy density (about $100\,\mathrm{Wh/kg}$) but high power density ($10^6\,\mathrm{W/kg}$). In this plot supercapacitors, also known as ultracapacitors or double layer capacitors, form a bridge between batteries and conventional capacitors, as they can store more energy per unit mass than the conventional capacitors, but still just a tiny fraction of the energy per unit mass of a battery [6, 19].

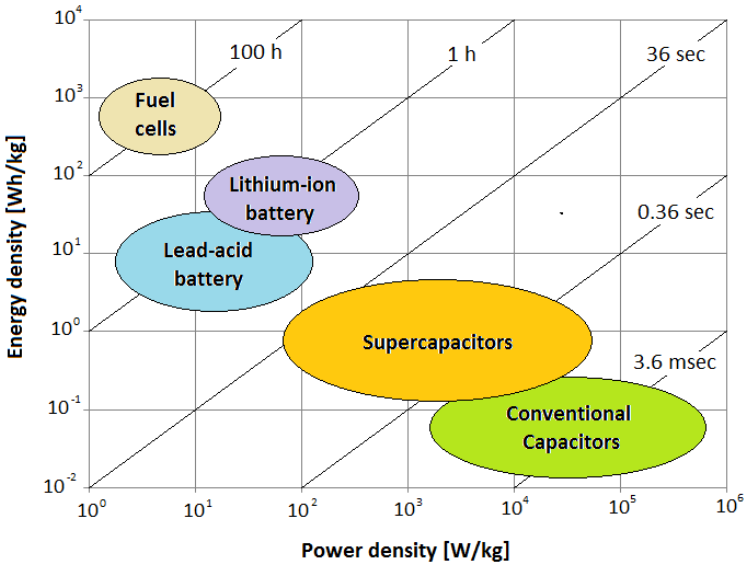

Figure 1.1: Ragoneplot of various energy storage devices, based on similar plots by e.g. [6]

Supercapacitors are used in many daily life devices, such as supplying everything from cellphones to computers with backup power for the memory. Supercapacitors may also replace the battery in vehicles driven by internal combustuion engines, as supercapacitors are functioning well even at temperatures as low as $-40\,^{\circ}\mathrm{C}$, where batteries are at their worst, but also at higher temperatures up to around $60\,^{\circ}\mathrm{C}$. The reason for this is that batteries rely on a chemical reaction to generate energy to deliver cranking power, whereas supercapacitors are storing the energy electrostatically, and can therefore deliver the power burst needed to start the engine, much less dependent on the temperature. Supercapacitors mainly find their use in devices that require rapid recharging, high power output and repetitive cycling. Which can be anything from a flashlight, recharged between each time its used, to cranes capturing energy during decent, through regenerative breaking, in a bank of supercapacitors. This energy can later be used to help heave other loads later on. In renewable energy generating devices, such as wind turbines and solar panels, supercapacitors can be used for storing energy to accellerate the turbine after a period with little wind and to prevent electrical dropouts in the solar panels [20, 21].

The application of thermoelectric generators is practically different from supercapacitors, as they are energy generators, and not energy storage devices. However, they also have applications for energy recouperation. Thermoelectric generators find their use where a temperature gradient is present. Energy dissipated as heat into the surroundings is considered lost work for a process, as it is no longer utilizable for practical means [22]. In the metalurgical industry major temperature gradients are present,

and recouperating even a fraction of the wast amounts of energy that goes into producing metals such as aluminium could prove valuable, both economically and environmentally.

Aluminium is a very handy material used for everything from packaging to parts in vehicles. The main reactant in the process of making aluminium is alumina, refined from bauxite mainly through the Bayer process. The Hall–Héroult electrochemical process was invented in 1886, and still remains the only industrial process used to produce the more than 40 million annual tons of pure aluminium, which exceeds that of all other nonferrous metals combined. In order to produce one kg of aluminium $13\,\mathrm{kWh}$ of energy is required, while recycling aluminium requires only $2.8\,\mathrm{kWh}$, accounting for only $5\,\%$ of the energy requried to make primary aluminium. Recycling of aluminium constitute about $20-25\,\%$ of the current aluminium demand, and saves the environment from about 90 million metric tons of CO_2 and over $100,000\,\mathrm{GWh}$ of electrical energy annually, compared to production of primary aluminium. However further energy savings are still possible. Aluminium has a melting point of $660\,^{\circ}\mathrm{C}$, and during the calcination in the Bayer process a temperature of $960\,^{\circ}\mathrm{C}$ is reached, giving great temperature gradients compared to room temperature [23, 24]. These temperature gradients represent energy sources applicable for energy recouperation, and can therefore serve as an example of where the thermoelectric generator can find their use. During the master thesis of Takla [2], a thermoelectric power generator demonstration unit was constructed, in collaboration with Thermo-Gen AB. The test unit was expected to be tested at Elkem Salten's aluminium production plant in Salten, but due to a delay in the delivery of the test unit, resuts from these experiments are still not available. However, this study could be the beginning of an energetical improvement of the aluminium business.

Thermoelectric generators can also be used for other means, such as e.g. recovering some of the heat released in the exhaust system of vehicles with an internal combustion engine. When operating a combustion engine only about 30 % of the energy latent in the fuel goes into the propelling force, moving the vehicle forward, while the remaining 70 % is goes into the exhaust and the cooling system. By implementing a thermoelectric generator inside the exhaust pipe with the exhaust as the heat source and a water cooling system as the heat sink, a temperature difference is obtained, with conversion efficincies ranging from approxiamtely 1 to 3 % [25–27]. By stacking 16 thermoelectric generators inside the exhaust pipe of a 2 L passenger car, Matsubara [28] obtained a power output of $266\mathrm{W}$, from a $475\,^{\circ}\mathrm{C}$ temperature difference. Thermoelectric generators also find their use in equipments where high precision temperature control is essential, like in e.g. medical or scientific apparatus. Also for pure cooling purposes thermoelectric generators are applicable, and could compete against the traditional vapour compression cooling systems, found in e.g. portable or domestic refridgerators, air-conditioning systems, vending machines, etc. [29].

In this master thesis both supercapacitors and thermoelectric generators will be investigated, as described in the project background. Supercapacitors and thermoelectric generators represent inde-

pendent technologies, due to their physical and theoretical obvoius differences. Their presentation will therefore also be devided into two separate, and mostly independent chapters; each with theory, experimental description, results, discussion and conclusions, for the respective devices.

Chapter 2

Supercapacitors

2.1 Theory

Supercapacitors, also known as ultracapacitors or electrical double layer capacitors (EDLC), store the energy electrostatically through polarization of an electrolyte solution. There is no chemical reaction taking place, and the net charge across the supercapacitor is zero. What determines the capacity of the supercapacitor is the distance between the electrodes, and the area of the electrode surfaces. The electrodes are made out of activated carbon which makes it possible to fold them, giving supercapacitors a major advantage over conventional capacitors with respect to electrode area per volume, and thereby also the capacitance per volume, which is why they have higher energy density than conventional capacitors. The activated carbon material also provides the supercapacitor with fairly good conductivity, electrochemically inertness, and lightweight properties [30]. An illustration of the internal mechanismisms in the electrolyte of supercapacitors during cycling is provided in figure (2.1). When charging a supercapacitor, the positively charged ions of the electrolyte move to the negative electrode, while the negative ions travel to the positive electrode. While when discharging the supercapacitor, the ions travel back into the solvent. The separator serve to electrically isolate the electrodes from each other. General aspects of capacitors are provided in the following section.

2.1.1 How does a capacitor work?

To perform this experiment it is important to understad how a capacitor (e.g. a supercapacitor) works. This section is dedicated to describing the basic concepts of the capacitor based on standard physics,

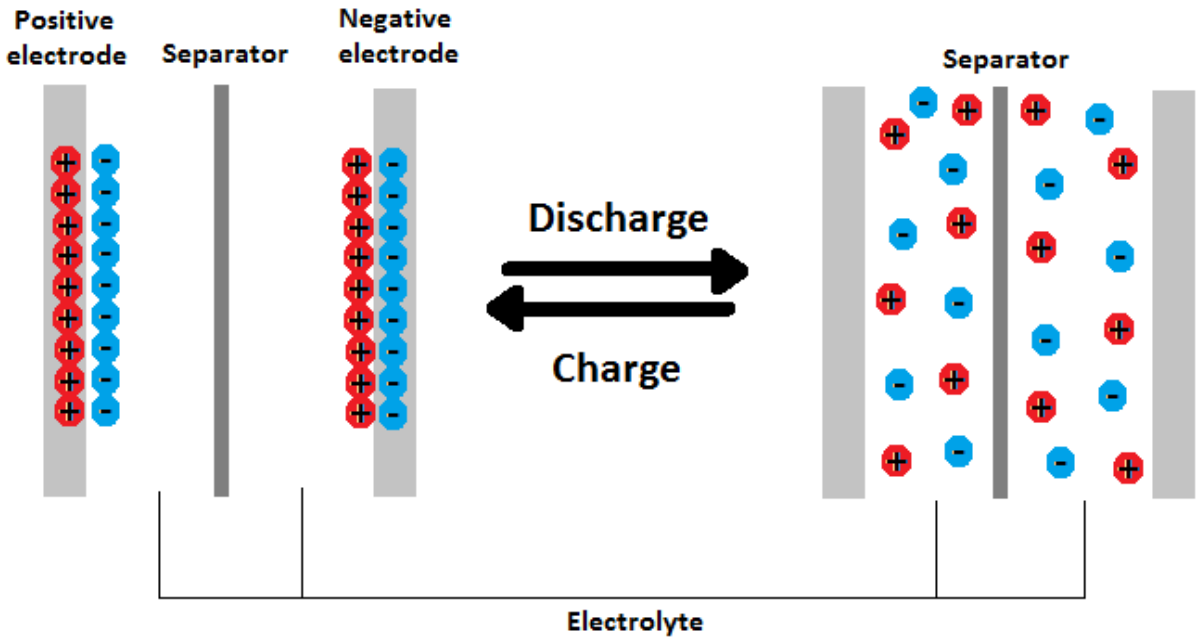

Figure 2.1: Charging and discharging mechanismis of the electrolyte in a supercapacitor.

retreiveable from Tipler and Mosca [31] and Ohanian [32][1].

Capacitance, C, is a measure of the capacity to store charge, Q, for a given potential difference, V, between two conductors, and equal to the ratio between the two be conductors, as shown in equation (2.1). The unit of capacitance is farad (F), or coulomb per volt (C/V) in SI units.

$$C = \frac{Q}{V} \tag{2.1}$$

A capacitor can be any arrangement of conductors that can be used to store electric charge. The capacitor is charged by transfering charge, Q, from one conductor to the other, giving a positively, +Q, and a negatively charged conductor, -Q, with equal absolute value. This is done by transferring electrons from the positively charged conductor to the negatively charged conductor, giving rise to an electron deficiency on the positively charged conductor and an electron surplus on the negatively

[1]The symbols used in section (2.1.1) serve only as an introduction to the basics of supercapacitors, and are only valied in in this respective section

charged conductor. To make this happen work must be done to charge a capacitor with electrostatic potential energy. In a supercapacitor the electrolyte serve medium for the transfer of electrons from the one electrode to the other.

Supercapacitors are in practice parallel-plate capacitors. When charging a parallel-plate capacitor, the charged plates attract each other and become uniformely distributed on the inside surfaces of the plates. Between the plates the electric field is uniform and can be calculated from equation (2.2):

$$E = \frac{\sigma_s}{\epsilon_0} \tag{2.2}$$

where σ_s is the surface charge density, and ϵ_0 is the permitivity of empty space. Because the electrical field, $\overrightarrow{E}$, is uniform between the plates, the potential difference beween the plates equals the field strength, E, multiplied with the plate separation, d, as shown in equation (2.3)

$$V = Ed = \frac{\sigma_s}{\epsilon_0} d = \frac{Qd}{\epsilon_0 A} \tag{2.3}$$

where the charge density, σ_s, is replaced by $\frac{Q}{A}$, where A is the area of the plates where they face each other. Substituting the potential difference from equation (2.3) into equation (2.1) generates a new expression for the capacitance of the parallel-plate capacitor, displayed in equation (2.4)

$$C = \frac{\epsilon_0 A}{d} \tag{2.4}$$

It can be noted that because the charge, Q, is proportional to the potential difference, V, the capacitance, C, does not depend on either Q or V. In general the capacitance depends only on the size, the shape, and the geometrical arrangement of the conductors, and also on the properties of the insulating medium between the conductors.

If the initial potential difference in the capacitor is given by $V = \frac{q}{C}$, an additional transfer of charge, dq, will increase the electrical potenial energy by an amount described by equation (2.5):

$$dU = V dq = \frac{q}{C} dq \tag{2.5}$$

The total change in potential energy, U, is therefore given by the integral of dU as q increases from zero charge to its final value Q, as presented in equation (2.6)

$$U = \int dU = \int_0^Q \frac{q}{C} dq = \frac{1}{C} \int_0^Q q dq = \frac{1}{2} \frac{Q^2}{C} \tag{2.6}$$

Inserting the expression for capacitans given in equation (2.1) into equation (2.6) gives a possibility of describing the potential energy, U, in terms of either Q and V, C and V, or Q and C, as shown in equation (2.7)

$$U = \frac{1}{2} \frac{Q^2}{C} = \frac{1}{2} QV = \frac{1}{2} CV^2 \tag{2.7}$$

Combining Capacitors

When two, or more, capacitors are connected together they can either be connected in parallel or in series. When coupled in parallel the devices would share a common potential difference, V, and the equivalent capacitance, C_{eq} is equal to the sum of the individual capacities, as seen from equation (2.8):

$$C_{eq} = \sum_{i=1}^{n} C_i = \sum_{i=1}^{n} \frac{Q_i}{V} \tag{2.8}$$

If the capacitors are connected in series on the other hand, they will have the same charges at the conductors in all the devices, and the equivalent capacitance, C_{eq}, is given by equation (2.9):

$$\frac{1}{C_{eq}} = \sum_{i=1}^{n} \frac{1}{C_i} = \sum_{i=1}^{n} \frac{V_i}{Q} \tag{2.9}$$

In other words, the equivalent capacitance, C_{eq} of capacitors connected in series will be less than the capacitance of capacitors connected in parallel, and in fact also less than the capacitance of either capacitor. This is caused by an increase in the plate separation, requiring a greater potential difference to store the same amount of charge. In the isothermal calorimeteric study, four supercapacitors will be connected in series, and in this way they are expected to behave as one capacitor with equal processes taking place in each supercapacitor as an equal amount of charges will residate on the electrodes at al time. As stated in the experimental section, the supercapacitors used each have a capacity of $10\,\mathrm{F}$ and a maximum applicable voltage of $2.70\,\mathrm{V}$, according to the manufacturer. Using equation (2.9), the corresponding capacitance of the supercapacitor stack is $2.5\,\mathrm{F}$, and the maximum applicable voltage is $10.80\,\mathrm{V}$.

2.1.2 Thermal Conductivity

In order to determine the thermal conductivity of the supercapacitors, λ, two models will be used, both in accordance with theory on transport phenomena described by Bird et al. [33]. The first (in situ) model, model I, seeks to determine the overall thermal conductivity of the supercapacitor stack using a sum of least squares method to fit the thermal conductivity to the internal temperature gradient, the ohmic resistance and the geometry of the stack. The second (ex situ) model, model II, uses a well established experimental method already by Burheim et al. through several experiments on material through-plane thermal conductivity [34–36]. Model II will serve to determine the thermal conductivity of the supercapacitor constituing materials, which in turn will serve to deduce the overall conductivity of the capacitors, providing a reference for model I.

Thermal Conductivity Model I: The Sum of Least Squares Method

This section is dedicated to finding a way to define the thermal conductivity, λ, from the stack of supercapacitors used in the isothermal calorimetric study. The flux of internal energy from the stack of supercapacitors, $\dot{U}$, is defined according to the first law of thermodynamics by equation (2.10):

$$\dot{U} = \bigtriangledown(\lambda \bigtriangledown T) + \dot{Q} = 0 \tag{2.10}$$

where λ is the thermal conductivity, $\dot{Q}$, is the ohmic heat flow, and $\bigtriangledown$ indicates the double deriviative in x, y and z direction. Because of the radial isolation, the system is treated in a one-dimensional way, and hence the double derivative, $\bigtriangledown$, will only be valid in one direction, $\bigtriangledown \rightarrow \frac{\partial}{\partial x}$.

In figure (3.3) the numbering of the various temperature measurements are indicated from T_1 through T_5, with the maximum temperature measured at T_3. Because the temperature profiles displayed in the results, in section (**??**), are distributed symmetrically at both sides of the maximum temperature, its geometrical position is set to zero in this model: $x(T_3) = 0$. The total thickness of the stack of supercapacitors is represented by the greek letter δ. As illustared in figure (2.2), the measurement points of the temperatures T_1 through T_5, are set at equal distances of $\frac{\delta}{4}$ apart from each other, ranging from $x = -\frac{\delta}{2}$ at T_1, to $x = \frac{\delta}{2}$ at T_5.

Due to the symmetrical nature of the temperature profiles, the two boundary conditions in equation (2.11) and (2.12) are assumed to be valid:

$$x(T = T_0) = \pm\frac{\delta}{2} \tag{2.11}$$

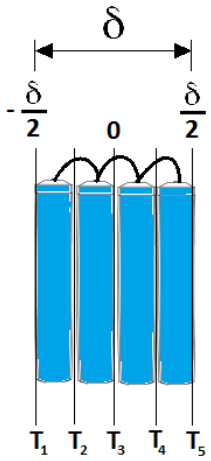

Figure 2.2: Cross-section of the capacitor stack

$$\frac{\partial T(x=0)}{\delta x} = 0 \tag{2.12}$$

where T_0 is the reference temperatures measured by the thermocouples at T_1 and T_5.

The ohmic heat flow generated in the supercapacitor stack is defined in equation (2.13):

$$\dot{Q} = \frac{Q_{total}}{V} = \frac{RI^2}{wh\delta} \tag{2.13}$$

where Q_{total} is the total heat generated by the supercapacitors, V is the volume of the supercapacitor stack, R is the electrical resistivity of the stack, I is the current entering the stack from the cycling unit, and w and h represent the width, and the height of the supercapacitor stack, respectively.

With the assumption of a one-dimensional system, equation (2.10) can be rearranged into equation (2.14):

$$\frac{\partial}{\partial x}\left(\lambda \frac{\partial T}{\partial x}\right) = -\dot{Q} \tag{2.14}$$

Since the distances between the measurement points are measured at intervals of $\frac{\delta}{4}$, and by assuming an uniform conduction through the capacitors, $\partial x \rightarrow dx$ and $\partial T \rightarrow dT$ can also be assumed.

Combining equation (2.13) and (2.14) and taking the integral of the $\dot{Q}$ term gives equation (2.15):

$$\lambda \frac{dT}{dx} = -\int \frac{RI^2}{wh\delta} dx = -\frac{RI^2}{wh\delta} x + C_1 \tag{2.15}$$

where C_1 is a constant from the indefinite integration. Using the boundary condition from equation (2.12), C_1 can be set equal to zero, $C_1 = 0$. By taking account for this, and rearranging equation (2.15) it turns into equation (2.16):

$$\int_{T(x)}^{T\left(\frac{\delta}{2}\right)} dT = -\frac{RI^2}{\lambda wh\delta} \int_{x}^{\left(\frac{\delta}{2}\right)} x dx \tag{2.16}$$

Integrating both sides of equation (2.16) gives equation (2.17):

$$T\left(\frac{\delta}{2}\right) - T(x) = -\frac{RI^2}{2\lambda wh\delta} \left(\frac{\delta^2}{4} - x^2\right) \tag{2.17}$$

Recognising that $T\left(\frac{\delta}{2}\right)$ in equation (2.17) is the reference temperature from the boundary condition of equation (2.11) at the intersection between the calorimeter and the stack, equation (2.18) is obtained:

$$\Delta T(x) = \frac{RI^2}{2\lambda wh\delta} \left(\frac{\delta^2}{4} - x^2\right) \tag{2.18}$$

By fitting the point of the temperature measurement from the experimental data to the expected temperature difference in equation (2.18), the termal conductivity, λ is found by minimalizing the sum of least squares, SoLS, of the difference between the experimental and modelled temperature difference by changing the thermal conductivity, according to equation (2.19)

$$SoLS = \frac{\partial \Sigma \left(\Delta T_i - \Delta T(x)\right)^2}{\partial \lambda} = 0 \tag{2.19}$$

where ΔT_i indicates the difference between the experimental temperature measurements at T_1 through T_5 and the referece temperature set equal to the average between T_1 and T_5, and $\Delta T(x)$ are the corresponding modelled temperature differences relative to the reference temperature.

Thermal Conductivity Model II: Obtaining the Thermal Conductivity from the Components

As mentioned earlier, the theory of this model is based on an already well established method, which has been used to determine the thermal through-plane conductivity of similar sample materials earlier, like e.g. fuel cell materials [34–36]. The apparatus used for the experimental procedure is described in section (2.2.3), and illustrated in figure (2.8).

This model uses an induced known heat flux through the steel steel cyclinders of the apparatus, sandwiching the sample, to determine the thermal conductivity. The apparatus provides a vertical 1D heat flux from the top to the bottom of the apparatus, through the steel cylinders and the sample, both with a diameter of $21.0 \pm 0.1\,\mathrm{mm}$. Temperatures are measured at three positions in each of the steel cylinders, at T_1 - T_3 and T_6 - T_8 in the upper and the lower cylinder, respectively, in order to ensure and determine the presence of the 1D heat flux, as illustrated in figure (2.8). Additionally the temperature at each side of the sample, at T_4 and T_5, is measured in order to determine the temperature drop across the sample. As described in the experimental section, the apparatus enables measurement of the sample thickness at applied compaction pressures, which makes it possible to recreate the expected compaction pressure within supercapacitors. The thickness of the samples, relative to the absence of samples, is varied by stacking sample layers on top of each other inside the apparatus.

Each of the two cylinders are workin as a kind of heat flux meter. The heat flux through the steel is obtained from the known thermal conductivity of the steel used in the construction, together with the change in temperature between the outermost temperature measurements, T_1 and T_3, and T_6 and T_8, as displayed in equation (2.20) and (2.21), for the upper and lower cylinder, respectively.

$$\dot{Q}_{upper} = \frac{\lambda_{steel}\,(T_1 - T_3)}{\delta_{1-3}} \tag{2.20}$$

$$\dot{Q}_{lower} = \frac{\lambda_{steel}\,(T_6 - T_8)}{\delta_{6-8}} \tag{2.21}$$

The heat flux through the sample is set equal to the average of the two heat fluxes, $\dot{\mathrm{Q}}_{\mathrm{lower}}$ and $\dot{\mathrm{Q}}_{\mathrm{upper}}$, as shown in equation (2.22).

$$\dot{Q}_{sample} = \frac{\dot{Q}_{upper} + \dot{Q}_{lower}}{2} \tag{2.22}$$

Having determined the heat flux through the sample, the thermal resistance, r, can be calculated from the temperature drop from T_4 to T_5 divided by the heat flux, from equation (2.23).

$$r_{sample} = \frac{T_4 - T_5}{\dot{Q}_{sample}} \tag{2.23}$$

Using the geometric proportions of the sample, namly the thickness at a given compaction pressure, δ_{sample}, and the area, $\mathrm{A_{sample}}$, and the thermal resistance, $\mathrm{r_{sample}}$, the thermal conductivity of the sample is obtained from equation (2.24).

$$\lambda_{sample} = \frac{\delta_{sample}}{r_{sample}\, A_{sample}} \tag{2.24}$$

This metod will be used to obtain the thermal conductivitis and resistivities of all the materials constituing the supercapacitor, λ_{i} and $\mathrm{r_i}$. When all the sample thermal conductivities are obtained, the total resisantance of the supercapacitor stack can be calculated from the total thickness of each constituent in the supercapacitor stack using equation (2.25).

$$r = \sum_i r_i = \sum_i \frac{\delta_i}{\lambda_i\, A_i} \tag{2.25}$$

To obtain the overall thermal conductivity, λ, the total thickness of the supercapacitor stack, δ, the axial area (corresponding to the area facing the aluminium plate in the calorimeter), A, and the total thermal resistance, r, are inserted in equation (2.26).

$$\lambda = \frac{\delta}{r\, A} \tag{2.26}$$

The value for the thermal conductivity from equation (2.26) will be compared to the value with the smallest sum of least squares in equation (2.19), and from that the validity of the two models will be determined.

2.1.3 Entropy Production

The entropy production is an important aspect in energy processes, as it is an important measure of the energy lost in industrial processes. Using non-equilibrium thermodynamics an expression for the entropy production of a supercapactor will be derived based on the theory of Kjelstrup et. al. [4]. To obtain an expression for the entropy production, one first set out to obtain an expression for the balance equations to be inserted in the Gibbs equation (2.27)

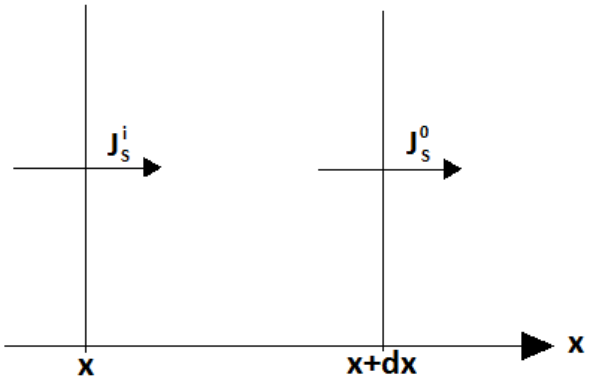

Figure 2.3: Entropy flux in one dimention

$$dU = TdS - pdV + \Sigma_{j=1}^{n} \mu_j dN_j \tag{2.27}$$

where T is the temperature, p is the preassure, μ_j is the chemical potential of compound j, and N_j is the number of moles of compound j. However since there is no change in volume during the cycling of the capacitors, and no change in the concentraton of the compounds of the system is assumed, the Gibbs equation of the system can be defined as in equation (2.28):

$$dU = TdS \tag{2.28}$$

The entropy production, σ, is defined in equation (2.29), and the entropy flux in one dimension is illustated in figure (2.3). The volume element between x and $x + dx$ represent a volume element cross-sectioning the plannar conductors of the supercondensator.

$$\sigma = \Sigma_i J_i X_i \geq 0 \tag{2.29}$$

In the system local equilibrium is assumed, and its state is given by the temperature, $T(x)$. The change in entropy in this volume element is assumed to be equal to the the entropy flux into the volume element minus the entropy flux out of the element, plus the entropy production inside the volume element, as described in equation (2.30):

$$\frac{dS}{dt} = -\Omega[J_s(x+dx) - J_s(x)] + V\sigma \tag{2.30}$$

where $\frac{dS}{dt}$ is the total change in entropy per time interval, Ω is the cross-section area of the volume element perpendicular to the x-direction, J_s is the entropy flux, V is the volume of the element and σ is the entropy production in the volume element.

Using the definition of the volume ($V = dx\Omega$) the cross-section area can be defined as $\Omega = \frac{V}{dx}$, and equation (2.30) can be redefined as equation (2.31)

$$\frac{dS}{dt} = -V\frac{[J_s(x+dx) - J_s(x)]}{dx} + V\sigma = -V\frac{dJ_s(dx)}{dx} + V\sigma \tag{2.31}$$

Dividing both sides of equation (2.31) by the volume, V, the entropy density in the region is obtained, as descibed in equation (2.32):

$$\frac{\partial s}{\partial t} = -\frac{\partial J_s}{\partial x} + \sigma \tag{2.32}$$

The change in the internal energy density of the system is given by equation (2.33):

$$\frac{\partial u}{\partial t} = -\frac{\partial}{\partial x}J_q + Ej \tag{2.33}$$

where J_q is the energy flux, and E is the electric field, which can be replaced by the minus the electric potential, as shown in equation (2.34):

$$E = -\frac{\partial \phi}{\partial x} \tag{2.34}$$

Equation (2.33) can thus now be converted into equation (2.35):

$$\frac{\partial u}{\partial t} = -\frac{\partial}{\partial x}J_q - \frac{\partial \phi}{\partial x}j \tag{2.35}$$

The energy flux, J_q, is defined in equation (2.36)

$$J_q = J_q^{'} + \Sigma_{J=1}^{n} H_j J_j \tag{2.36}$$

where $J_q^{'}$ is the measurable heat flux, and H_j and J_j are the partial molar enthalpy and the component flux of compound j, respectively. In the particular case of the supercapacitors, however, the last term of equation (2.36) can be terminated because there is no net flux of components, and the energy flux, J_q can be set equal to the measurable heat flux, J_q', as displayed in equation (2.37):

$$J_q = J_q^{'} \tag{2.37}$$

In order to convert equation (2.28) into its local form the internal energy, U, and the entropy, S, is replaced by their densities, $u = \frac{U}{V}$, and $s = \frac{S}{V}$, respectively. Doing this and assumning a constant volume in the capacitor, generates eqation (2.38):

$$du = Tds \tag{2.38}$$

By rearranging equation (2.38) and implementing the time derivative makes it possible to express the local entropy density on the form dispalyed in equation (2.39):

$$\frac{\partial s}{\partial t} = \frac{1}{T}\frac{\partial u}{\partial t} \tag{2.39}$$

Inserting the expression for $\frac{\partial u}{\partial t}$ from equation (2.35) gives equation (2.40):

$$\frac{\partial s}{\partial t} = \frac{1}{T}\left[-\frac{\partial}{\partial x}J_q - \frac{\delta\phi}{\delta x}j\right] \tag{2.40}$$

In equation (2.40) the expression for the heat flux, J_q can be differentiated using the product rule, as described in equation (2.41):

$$\frac{\partial}{\partial x}\left(\frac{1}{T}J_q\right) = J_q\frac{\partial}{\partial x}\left(\frac{1}{T}\right) + \frac{1}{T}\frac{\partial}{\partial x}(J_q) \tag{2.41}$$

Reinserting equation (2.41) back into equation (2.40) and rearranging it gives equation (2.42):

$$\frac{\partial s}{\partial t} = -\frac{1}{T}\frac{\partial}{\partial x}(J_q) + J_q\frac{\partial}{\partial x}\left(\frac{1}{T}\right) + j\left(-\frac{1}{T}\frac{\partial\phi}{\partial x}\right) \tag{2.42}$$

The entropy flux, J_s, is identified as equation (2.43), due to the assumtion of no change in concentration.

$$J_s = \frac{1}{T} J_q \tag{2.43}$$

Identifying and inserting for the entropy flux, J_s from equation (2.43) into equation (2.42), substituting the energy flux, J_q, with the measurable heat flux,J'_q, due to equation (2.37) reveals equation (2.44)

$$\frac{\partial s}{\partial t} = -\frac{\partial}{\partial x} J_s + J'_q \frac{\partial}{\partial x}\left(\frac{1}{T}\right) + j\left(-\frac{1}{T}\frac{\partial \phi}{\partial x}\right) \tag{2.44}$$

From equation (2.30) the entropy production, σ, can be identified as the equal to the two last terms of equation(2.44), revealing equation (2.45):

$$\sigma = J'_q \frac{\partial}{\partial x}\left(\frac{1}{T}\right) + j\left(-\frac{1}{T}\frac{\partial \phi}{\partial x}\right) = J'_q\left(-\frac{1}{T^2}\frac{\partial T}{\partial x}\right) + j\left(-\frac{1}{T}\frac{\partial \phi}{\partial x}\right) \tag{2.45}$$

Equation (2.45) represents a theoretical description of the system, but it is not yet applicable to the experimental data. This will be done in the next section using theory based on the Onsager reciprocal relations.

Fluxes and Forces

In irreversible thermodynamics a linear relationship between the forces and fluxes is assumed, as described in equation (2.46):

$$J_i = \Sigma_{j=1}^{n} L_{ij} X_j \tag{2.46}$$

, where L_{ij} are the so-called phenomenological coefficients, also known as the Onsager coefficients, which reduce the total number of indendent coeffi. The Onsager coefficients reduce the number of independent coefficients in the system and makes it possible to relate due to the relation described in equation (2.47):

$$L_{q\phi} = L_{\phi q} \tag{2.47}$$

Using the linear relation between the fluxes and the forces given in equation (2.46), the flux equations for the measurable heat flux and the electric current density can be derived as in equation (2.48), and (2.49), respectively:

$$J_q^{'} = L_{qq}\left[\frac{\partial}{\partial x}\frac{1}{T}\right] + L_{q\phi}\left[-\frac{1}{T}\frac{\partial \phi}{\partial x}\right] = -L_{qq}\frac{1}{T^2}\frac{\partial T}{\partial x} - L_{q\phi}\frac{1}{T}\frac{\partial \phi}{\partial x} \tag{2.48}$$

$$j = L_{\phi q}\left[\frac{\partial}{\partial x}\frac{1}{T}\right] + L_{\phi\phi}\left[-\frac{1}{T}\frac{\partial \phi}{\partial x}\right] = -L_{\phi q}\frac{1}{T^2}\frac{\partial T}{\partial x} - L_{\phi\phi}\frac{1}{T}\frac{\partial \phi}{\partial x} \tag{2.49}$$

At constant temperature the first part of the expression for the electric current, in equation (2.49), can be eliminated, and we are left with equation (2.50):

$$j = -L_{\phi\phi}\frac{1}{T}\frac{\partial \phi}{\partial x} \tag{2.50}$$

When combining equation (2.50) with Ohm's law, given in in equation (2.51)

$$j = -\kappa\frac{\partial \phi}{\partial x} \tag{2.51}$$

an expression for the electrical conductivity, κ , can be extracted, as done in equation (2.52):

$$\kappa = \frac{L_{\phi\phi}}{T} \tag{2.52}$$

The thermal conductivity, λ, at zero electric current, j, is defined in equation (2.53):

$$\lambda \equiv -\left[\frac{J_q^{'}}{\frac{\partial T}{\partial x}}\right]_{j=0} = \frac{1}{T^2}\left[L_{qq} - \frac{L_{\phi q}L_{q\phi}}{L_{\phi\phi}}\right] \tag{2.53}$$

The Peltier coefficient, π, is related to the Seebeck coefficient through the Onsager reciprocal relations. It is defined as the heat being transfered, reversibly, per unit charge with the electric current at constant temperature, and is defined in equation (2.54):

$$\pi \equiv F\left[\frac{J_q^{'}}{j}\right]_{dT=0} = F\frac{L_{q\phi}}{L_{\phi\phi}} \tag{2.54}$$

Now equation (2.52), (2.53) and (2.54) will be implemented in equation (2.48) and (2.49). To do this equation (2.49) will first be solved for $\frac{\partial \phi}{\partial x}$, as shown in equation (2.55):

$$\frac{\partial \phi}{\partial x} = -\frac{L_{\phi q}}{L_{\phi\phi}}\frac{\partial T}{\partial x} - \frac{T}{L_{\phi\phi}}j \tag{2.55}$$

When the expression for $\frac{\partial \phi}{\partial x}$, obtained in equation (2.55), is inserted into equation (2.48) to replace the corresponding factor, we obtain equation (2.56):

$$J_q^{'} = -\left[L_{qq} - \frac{L_{q\phi}L_{\phi q}}{L_{\phi\phi}}\right]\frac{1}{T^2}\frac{\partial T}{\partial x} + \frac{L_{q\phi}}{L_{\phi\phi}}j \tag{2.56}$$

Now equation (2.56) can be transformed by replacing $\frac{1}{T^2}[L_{qq} - \frac{L_{q\phi}L_{\phi q}}{L_{\phi\phi}}]$ by the thermal conductivity, λ, as described in equation (2.53), $L_{\phi\phi}$ by κT, as described in equation (2.52), and by using the Onsager reciprocal relations and equation (2.53) combined with equation (2.52) $L_{q\phi}$ can be expressed as $\frac{\kappa\pi T}{F}$, and from this equation (2.57) is obtained:

$$J_q^{'} = -\lambda\frac{\partial T}{\partial x} + \frac{\pi}{F}j \tag{2.57}$$

In equation (2.49) $L_{\phi q}$ and $L_{\phi\phi}$ can be replaced by the same values as in equation (2.57), and equation (2.58) is obtained:

$$j = -\frac{\kappa\pi}{FT}\frac{\partial T}{\partial x} - \kappa\frac{\partial \phi}{\partial x} \tag{2.58}$$

When solving equation (2.57) with respect to $\frac{\partial T}{\partial x}$ and equation (2.58) with respect to $\frac{\partial \phi}{\partial x}$ and inserting these expressions into equation (2.45) a new equation for the entropy production arises. In equation (2.59) the entropy production is defined as a function of the two adjustable parameters in our model, namely the temperature, T, and the current density, j:

$$\sigma = \frac{\left(J_q' - \frac{j\pi}{F}\right)^2}{T^2\lambda} + \frac{j^2}{T\kappa} \tag{2.59}$$

The electric conductivity is defined in equation (2.60).

$$\kappa = \frac{\delta}{R\,A} \tag{2.60}$$

In the case of the supercapacitors, the electic conductivity concerns the total thickness of activiated carbon layer on the two carbon/aluminium electrodes and the separator, which is assumed to be saturated with electrolyte, sandwiched between the respective electrodes. By taking account for this, equation (2.60) can be re-expressed as equation (2.61).

$$\kappa = \frac{\delta_{sep.} + 2\,\delta_{el.}}{R\,A} \tag{2.61}$$

where R is the ohmic resistanceof the device, A is the equi-sized area of the unfolded separator and electrodes, and $\delta_{\mathrm{sep.}}$ and $\delta_{\mathrm{el.}}$ are the thicknesses of the separator and each of the separators, respectively. By inserting the expression for the electric conductivity, in equation (2.61), back into equation (2.59), a final model equation for the entropy production is obtained, as displayed in equation (2.62).

$$\sigma = \frac{\left(J'_q - \frac{j\pi}{F}\right)^2}{T^2\lambda} + \frac{R\,A\,j^2}{T\left(\delta_{sep.} + 2\,\delta_{el.}\right)} \tag{2.62}$$

Regarding the acquisition of the experimental parameters of the electrical contribution to the entropy production in equation (2.62); the ohmic resistance, R, is obtained from measurements prior to the cycling, the area of the separator and the electrodes, A, and their respective thicknesses, $\delta_{\mathrm{sep.}}$ and $\delta_{\mathrm{el.}}$, are obtained from dissecations of the devices, j is the current density defined as the current applied devided by the unfolded equi-sized area of the separator and the electrodes, and T is average temperature measured at interface of the superacapacitor stack facing the calorimeter.

Equation (2.62) basically states that the entropy produced by the supercapacitors is due to generated heat, and internal ohmic resistance. To test its validity the entropy production will have to be compared to the entropy delivered from the system (the supercapacitor stack) to the environment, in this case through the aluminium plates sandwiching the stack. The classical expression of the second law of thermodynamics is stated in equation (2.63).

$$\Delta S + \Delta S_0 \geq 0 \tag{2.63}$$

where $\Delta\mathrm{S}$ is the entropy change of the process, and $\Delta\mathrm{S}_0$ is the entropy change in the environment. Meaning that the total entropy change is positive, and for a completely reverible process the entropy change would be zero. For an irreversble process the sum of the entropies can be used to define the

the average total entropy production, $\frac{\mathrm{dS_{irr}}}{\mathrm{dt}}$ in a time interval of a stationary process, $\Delta\mathrm{t}$, displayed in equation (2.64)

$$\left(\frac{dS_{irr}}{dt}\right)\Delta t \equiv \Delta S + \Delta S_0 \tag{2.64}$$

As illustrated in figure (2.1) the process within the supercapacitors consist in moving the positive and negative ions from the solvent to the electrodes when charging, and the opposite process when discharging. This means that the entropical contributions from the systems internal process cancel out, and the entropy delivered to the environment remains the only contribution to the entropy production. When assuming that the environment behaves reversibly, the entropy change in the surroundings is $\Delta\mathrm{S_0} = \frac{\mathrm{q_0}}{\mathrm{T_0}}$. The resulting equation for the entropy production of the irreversible process therefore can be expressed as equation (2.65).

$$\left(\frac{dS_{irr}}{dt}\right)\Delta t \equiv \frac{q_0}{T_0} \tag{2.65}$$

where $\mathrm{q_0}$ is the heat delivered to the calorimeter from the supercapacitors, and $\mathrm{T_0}$ is the environment temperature at interface between the supercapacitors and the calorimeter.

2.2 Experimental

In these experiments the Maxwell PC10 Series supercapacitors have been selected to be investigated. They were chosen in order to fit into the calorimeter designed by Burheim [3], although it should be mentioned that their shapes are not ideal, as they are not perfectly cubic, and they do not cover the entire interface of the internal aluminium plates. In these experiments four supercapacitors are connected in series with wires, as shown in figure (2.4). In this way they are expected to behave as one single supercapacitor, while giving access to the internal temperature gradients of the stack, that would otherwise be difficult to obtain. The thermal and electric conductivity of the supercapacitors is also to be investigated, for which two models have been proposed for the thermal conductivity and one for the electric conductivity, as previously described in the theory. For finding the thermal and electric conductivity of the supercapacitors both a calorimeter and an apparatus for specifically designed for thermal conductivity measurements of material samples will be used, in addition to dissications of the devices. In the following a few of the specifics of the supercapacitors, given by the manufacturer [37], are given:

Capacity: $10\,\mathrm{F}$

Absolute maximum voltage: $2.70\,\mathrm{V}$

Applicable temperature range: $-40\,^{\circ}\mathrm{C}$ to $70\,^{\circ}\mathrm{C}$

Lifetime: 500,000 charge/discharge cycles

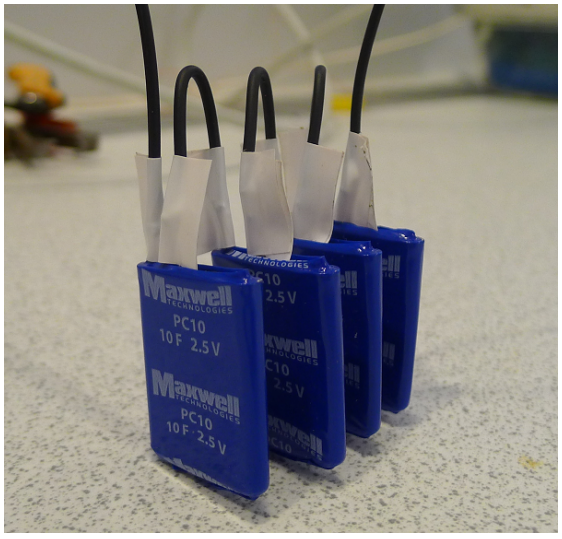

Figure 2.4: Four Maxwell PC10 Series supercapacitors coupled in series.

2.2.1 Experiment I: Isocalorimetric Study of a Supercapacitor Stack

In order to test the efficiency of the supercapacitor stack during use, the stack was cycled by charging and discharged it repeatedly leading to a stationary thermal state. The isocalorimetric experiment was carried out at $30 \pm 0.1\,^{\circ}\mathrm{C}$ in a calorimeter, which will be descibed in detail later on in this section, using a Princeton Applied Research 263A Potentiostat/Galvanostat (PAR 263A) to charge and discharge the stack while logging the heat and temperature gradients produced. The PAR 263A was controlled by a computer through a Corrware software operating in a galvanostatic mode, which also recorded the cycling data of the applied currents and voltages every second. The supercapacitor stack was cycled stepwise at currents from $0\,\mathrm{A}$ to $2\,\mathrm{A}$, with current intervals of $0.125\,\mathrm{A}$, charging and discharging between voltages of $0\,\mathrm{V}$ and $2\,\mathrm{V}$ (safely within the $2.70\,\mathrm{V}$ maximum voltage given by the maufacturer) for 100 charge/discharge cycles per current level. In this way a stationary state of the consecutive current level was reached in a fast and smooth way. The circuit scheme of the supercapacitor stack is displayed (to the right) in figure (2.5), together with a photo of the supercapacitor stack (to the left). In the coupling scheme the four supercapacitors are marked with the conventional capacitor sign, and additionally the letter C. The working, counter and reference electrodes are indicated by WE, CE and RE, respectively, indicating the connection to the PAR 263A.

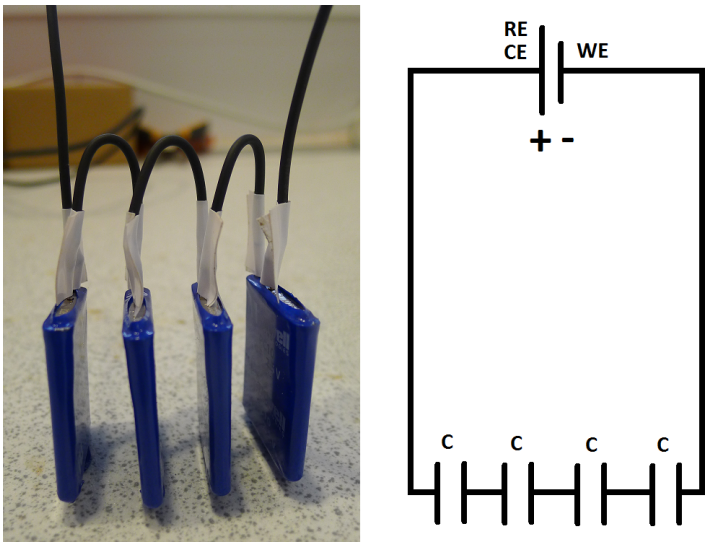

Figure 2.5: Image of one of the Maxwell PC10 supercapacitor stacks with four supercapacitors coupled in series (to the right), and the corresponding coupling scheme (to the left). The supercapacitors are indicated with the conventional capacitor sign (and additionally the letter C), and the working electrode, WE, and the counter and reference electrodes, CE and RE, are marked at the negative and positive output of the PAR 263A, respectively.

The heat produced by the supercapacitor stack was measured by a calorimeter designed by Burheim for his doctoral thesis [3], originally designed for measuring the heat leaving the catode and anode side of a fuel cell. The calorimeter was later modified for the master thesis of Takla [2] in 2010, in order to fit the shape of $40\,\mathrm{mm} \times 40\,\mathrm{mm}$ thermoelectric generators, which is also the same version of the apparatus used in this experiment. An overview of a cross section of the calorimeter experimental setup is given in figure (2.6).

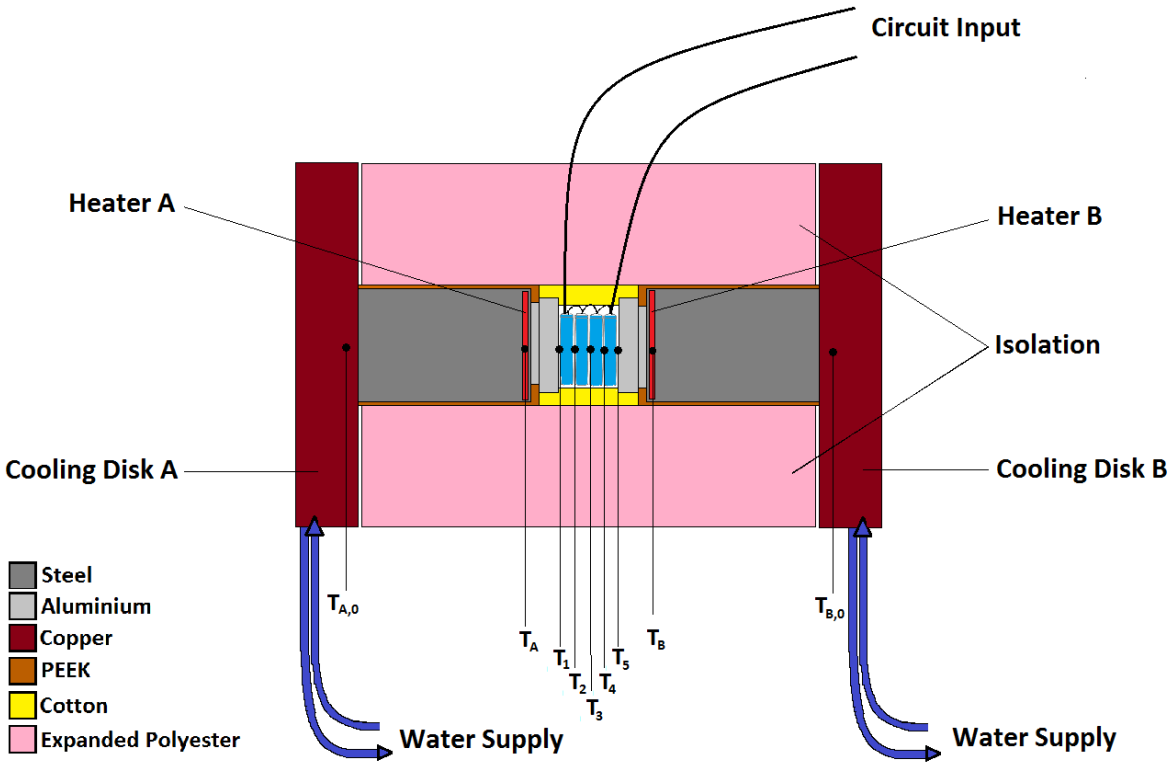

Figure 2.6: Experimental set-up of the supercapacitor stack sandwiched in the calorimeter. The supercapacitor stack is sandwiched between two aluminium plates of the calorimeter, and a heat flux is generated from the heaters (Heater A and B) to the copper cooling disks (Cooling Disk A and B), through the steel cylinders. The housing of the two symmetrical parts of the calorimeter is made from PEET, and the radial isolation is made from expanded polyester. The effect from the heaters and the temperatures indicated, which are measured with K-type thermocouples, are logged in a LabView setup. The cycling is carried out using a PAR 263A.

The calorimeter is constructed as a cyclinder with insulation at the radial walls and heat transport in the axial directions. The calorimeter consists of two symmetrical pieces making it possible to distinguish between heat leaving at eighter side of the supercapacitor stack. This is done by generating a heat flux from the heaters two heaters in the direction to the cooling disks. The calorimeter is built primarely in steel, copper, aluminium, poly ether ether ketone (PEEK), and expanded polyester. The stainless steel cylinders, with their intermediate thermal conductivity, serve to create a significant temperature gradient between the heaters and the cooling disks. The cooling disks are made from copper, due to its high thermal conductivity, which is well suited for applying the cooling from the waterbath through copper pipes soldered onto the copper disks. The cooling liquid (water doped with glycolic antifreeze) is supplied from a Grant R1 Low Temperature Bath/Circulator set to a temperature of $8\,^{\circ}\mathrm{C}$, giving temperatures of approximately $10\,^{\circ}\mathrm{C}$ at the cooling disks. Due to the high thermal conductivity of copper, it was also used in the heaters as housing for $10\,\Omega$ resistive heating wires. High conductivity is also required at the interface facing the device to be tested; therefore aluminium is the building material of the $40\,\mathrm{mm} \times 40\,\mathrm{mm}$ plates facing the supercapacitors. The housing of the two symmetrical parts of the calorimeter is made from PEEK, due to its thermal and electric insulation properties, and its mechanical strength. The radial insulation between the copper cooling plates are made of expanded polyester, and additional cotton was placed around the supercapacitor stack, in order to maximize the insulation in the radial directions. In order to maximize thermal conductivity in the axial direction, thermally conductive paste was greased at all axial inerfaces of the supercapacitors, and also between all connecting axial interfaces in the calorimeter itself. Four screws running through the calorimeter in the axial direction was additionally tightened in a symmetrical way, using an electric hand drill.

The heat from the heaters and the temperatures were logged using a LabView setup. The temperatures at the heaters, the cooling disks, and at interfaces of the supercapacitors were measured using K-type thermocouples at the positions indicated in figure (2.6). The temperature at the heaters and the cooling disks, $\mathrm{T_A}$ and $\mathrm{T_B}$, and $\mathrm{T_{A,0}}$ and $\mathrm{T_{B,0}}$, respectively, served to control that a temperature gradient was present through the steel cyclinders. The heaters were controlled using two Eurotherm thermostatic PID-controllers, regulating the effect applied to the resistive heating wires relative to the temperature measured at $\mathrm{T_A}$ and $\mathrm{T_B}$. In order to be sure to have the wanted temperature at the interface between the supercapacitor and the calorimeter, the temperature setpoint of the heaters were adjusted in order to obain a temperature of $30 \pm 0.1\,^{\circ}\mathrm{C}$ at either side of the supercapacitor stack, at $\mathrm{T_1}$ and $\mathrm{T_5}$. In order to be able to determine the effect applied to the supercapacitors, by using Ohm's law, the ohmic resistance was measured during an initial calibration before the cycling was initiated. Measuring the ohmic resistance during cycling was attemped in a project by Hauge [1], but proved to interfere in the cycling process, and was therefore avoided here. The reduction in effect from the heaters during cycled is interpreted as the heat produced by the supercapacitors, which is to be compared to the effect applied. The thermocuples measuring the temperatures at the

interstitial positions of the supercapacitor stack, T_1 - T_5, serve to prove that a temperature gradient is present inside a supercapacitor while in use. The temperature gradient is also used to find the thermal conductivity of the stack as a unit, using the model described in section (2.1.2). The thermal conductivity of the supercapacitor materials was also determined using the model desctribed in section (2.1.2), as will be described in section (2.2.3).

A schematic summary and description of the experimental setup is displayed in figure (2.7). In the figure five units are presented, numbered from 1 to 5 indicating the calorimeter unit, the heater controller, the waterbath, and cycling and recording unit 1 and 2, respectively. The calorimeter unit consists of the calorimeter sandwiching the Maxwll PC10 Series supercapacitors. The circuits of the resistive heating wires inside of the two heaters are indicated with orange lines, and the fluxes of water doped with glycolic antifreeze from the Grant R1 Low Temperature Bath/Circulator is indicated by purple lines Cycling and recording unit 1 contains an Agilent 4338B Milliohmmeter and computer with a LabView software recording experimental data from the calorimeter unit. The acquistation of data from the experiment is indicated with green lines. Cycling and recording unit 2 consists of a PAR 263A controlled by a computer through a CorrWare software for control and recording of the applied voltages and currents. The circuit of the cycling from the PAR 263A through the supercapacitor stack is indicated with black lines.

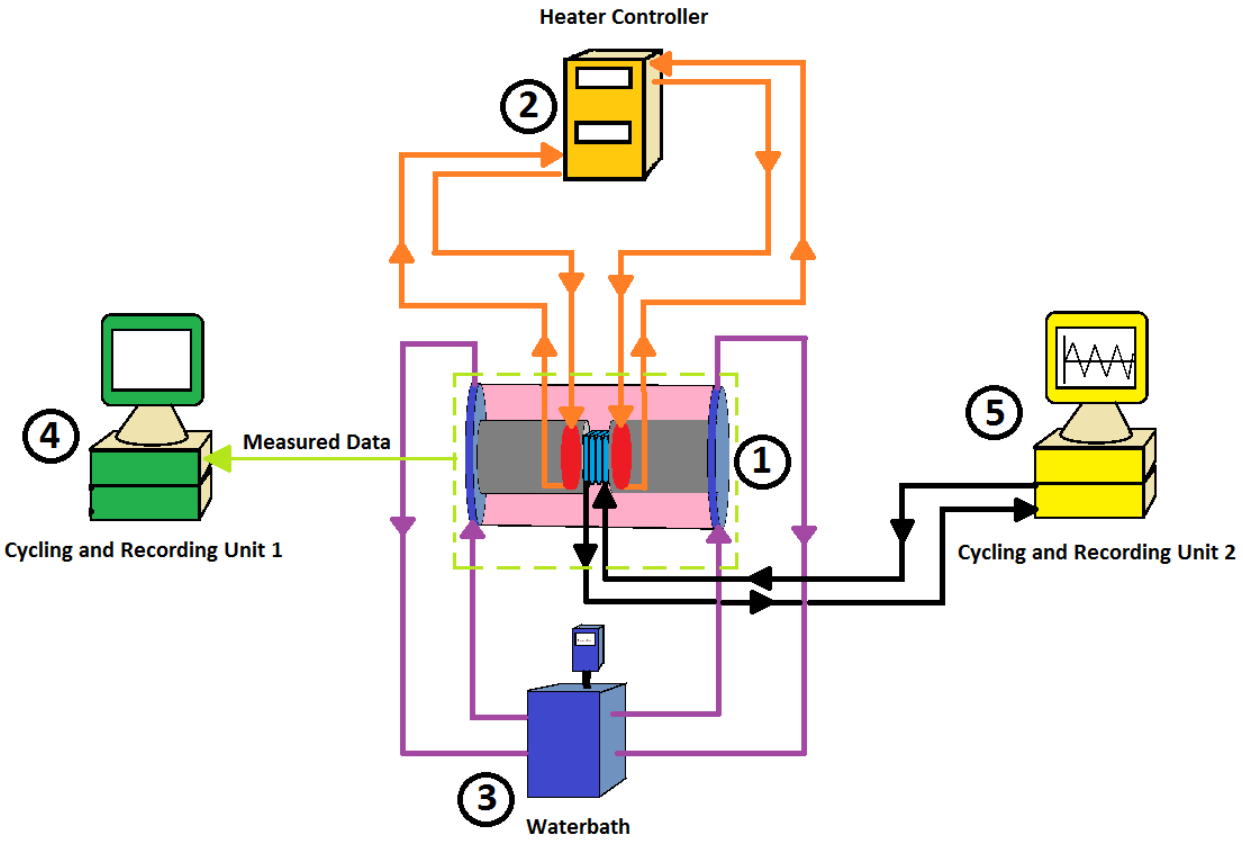

Figure 2.7: Experimental set-up of the caliorimetric studies of supercapacitor stack. In the figure the five experimental units used during the experiments are presented. (1) The calorimeter unit: Consisting of a a stack of four Maxwell PC10 Series supercapacitors sandwiched between the two symmetrical parts of the calorimeter designed by Burheim [3]. (2) Heater controller: A double Eurotherm PID-controller controlling the effect delivered to two resistive heating wires inside the calorimeter by keeping their temperature constant during measurements. The circuits of the resistive heating wires inside of the two heaters are indicated with orange lines. (3) Waterbath: A Grant R1 Low Temperature Bath/Circulator containing water doped with glycolic antifreeze delivering a flux of cold liquid to the external copper cooling disks of the calorimeter. The two fluxes of water doped with glycolic antifreeze is indicated by purple lines. (4) Recording and Cycling Unit 1: Consisting of an Agilent 4338B Milliohmmeter and computer with a LabView software recording experimental data from the calorimeter unit. The acquistation of data from the experiment is indicated with green lines. (5) Recording and Cycling Unit 2: Consisting of a Princeton Applied Research 263A Potentiostat/Galvanostat connected with a computer with a CorrWare software for control and recording of the applied voltages and currents. The circuit of the cycling from the Potentiostat/Gavvanostat is indicated with black lines.

2.2.2 Experiment II: Dissecation and Determination of the Internal Structural Conformation of the Supercapacitors

In order to obtain materials for Experiment III, and for determining the electric conductivity of the electrodes, dissecations of the supercapacitors had to be carried out. A scalpel was used to remove the external plastic coating, and a hacksaw was then used to open the steel housing. Measurements of the thickness of the components was obtianed with a Multoyo thickness micrometer, with an accuracy of $0.001\,\mathrm{mm}$. The carbon electrolytic layer was removed from the underlying aluminium, mechanically using a scalpel, in order to obtain its thickness. The dissecation also revealed the internal conformation of the carbon electrodes, the saparator and the aluminium current collectors.

2.2.3 Experiment III: Measurement of the Thermal Conductivity of Supercapacitor Materials

In section (2.1.2) a model for obtaining the thermal conductivity of the supercapacitor materials are presented. Materials obtianed from the dissecation in experiment III was investigated using an apparatus previously used by Burheim, Kjelstrup and Vie in numerous experiments on thermal through-plane conductivity [34–36, 38], depicted in figure (2.8). The apparatus is designed to generate a constant 1D heat flux through the sample of a cylindrical geometry. As displayed in the figure the samples are sandwiched between the two symmetrical metal cylinders (with a $21\,\mathrm{mm}$ diameter). The samples to be tested were be inserted as both single layers and then stacked on top of each other in increasing numbers in order to vary the sample thickness. The sample thicknesses were measured as a function of the compression pressure applied vertically from the bottom to the top of the apparatus. The thickness of the sample was measured using two Mitutoyo Digimatic Indicator ID-C Series 543, attached to the upper flange touching down onto the lower flange with the measuring tip, as illustrated in the figure. The change in distance, relative to calibrations done without samples inside the apparatus, is interpreted as the thickness of the sample, at the given compaction pressure.

The mobile parts of the appartus are confined between two steel plates attached to each other with four bolts. The compaction pressure is applied from a gas bottle, containing compressed air, which is led into a pneumatic piston located at the bottom steel plate, through a nylon coilhose. The pneumatic piston pushes the internal cylinders upwards against a steel ball held back by the upper steel plate, compressing the sample between the cylinders. The heat flux is generated by two fluxes of hot water and cold water passing through the top and bottom end of the internal cylinders, respectively. The cold water flux (doped with glycolic antifreeze) was obtained from a Grant R2 Low Temperature Bath/Circulator, and the hot water flux from a home-made heating bath, consisting of a Eurotherm

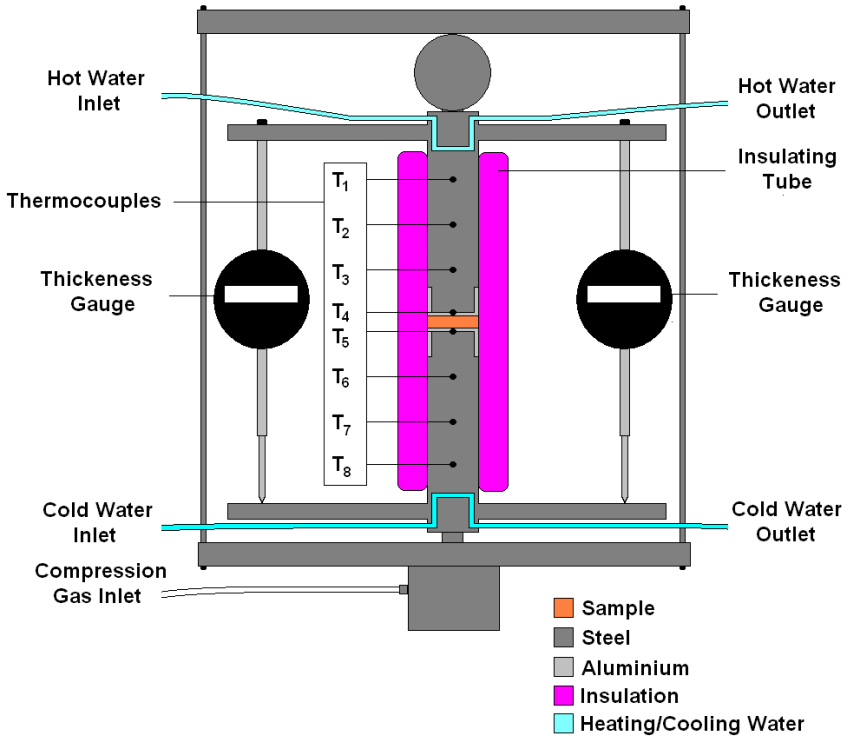

Figure 2.8: Apparatus for experiments on sample thermal through-plane conductivity, λ.

PID-controller regulating the effect given to a resistive heating wire inside a steel container, circulating the water with a Biltema 12 V pump. The temperature of the cold and hot water was regulated to $5\,^{\circ}\mathrm{C}$ and $40\,^{\circ}\mathrm{C}$, respectively, which proved to give a fair temperature gradient through the cylinders and the sample. The temperatures fitting the model described in section (2.1.2) are measured using eight K-type thermocouples, indicated with T_1 through T_8 in the figure. All eight temperatures were recorded using an Agilent Acquisition Switch Unit 34970A. Radial insulation is assured with a double-walled evacuated glass tube, coated with silver at the inside walls and further isolated with a polymer insulation material on the outside.

The two symmetrical cylinders are made from steel from the flanges to the interface towards the sample, which is coated with a thin aluminium layer. The relatively low thermal conductivity of steel makes it a suitable material to achieve a thermal gradient, giving the heat flux a high resolution. The cap facing the sample is made out of highly conductive aluminium because an isothermal region adjacent to the sample is needed in order to determine the temperature drop across the sample. Three thermocouples are placed inside the upper and lower steel cylinders, measuring the temperature at

T_1 - T_3 and T_6 - T_8, respectively, in order to assure the presence of a linear temperature profile through the steel sections. From these temperature measurements the heat fluxes through the upper and lower cylinders are determined. Thermocouples were also placed at each interface between the steel and aluminium cap, at T_4 and T_5, thus making the cap behave as a thermometer disk, yielding the temperature drop across the sample.

The samples of the separators, the carbon/aluminium electrodes, the aluminium current collectors and the plastic coating were cut into $21\,\mathrm{mm}$ disks, fitting the surface of the aluminium cap of the steel cylinders. The samples of the separator and the electrodes were also soaked in 1 M tetraethylammonium-tetrafluoroborate ($TEA - BF_4$) solved in acetonetrile, in order to reproduce the electrolytic conditions inside the supercapacitors. This is in accordance with similar experiments previously carried out by Burheim et al. [36]. The experiments started with a single layer, and then three more sample thicknesses were tested by stacking an increasing number of sample layers on top of each other. The thickness of the samples was measured every at $2.3\,\mathrm{bar}$ intervals, by first compressing the samples from $2.3\,\mathrm{bar}$ to $16.1\,\mathrm{bar}$, and then decompressing the samples back down to from $2.3\,\mathrm{bar}$. The temperature measurements were carried out every 15 seconds for 15 minutes at $4.6\,\mathrm{bar}$, $9.2\,\mathrm{bar}$, $13.6\,\mathrm{bar}$ and $16.1\,\mathrm{bar}$ during compression, and at $4.6\,\mathrm{bar}$ during decompression. Only the last 5 minutes of the temperature measurements were used for determining the thermal conductivity, in order to be sure to have stationary conditions within the apparatus. Among the five compaction pressures at which the temperature was measured, $4.6\,\mathrm{bar}$ during compression is expected to be the best reproduction of the conditions inside the supercapacitors.

2.3 Results and Discussion

In the following the results from the experiments described in the experimental section (2.2) are presented as average values, with 95 % confidence intervals, in accordance with the theory on error estimates described in appendix A. All raw data, and graphs of the corresponding experiments examplified in the figures, are presented in appendix B.1.

2.3.1 Supercapacitor Geometry

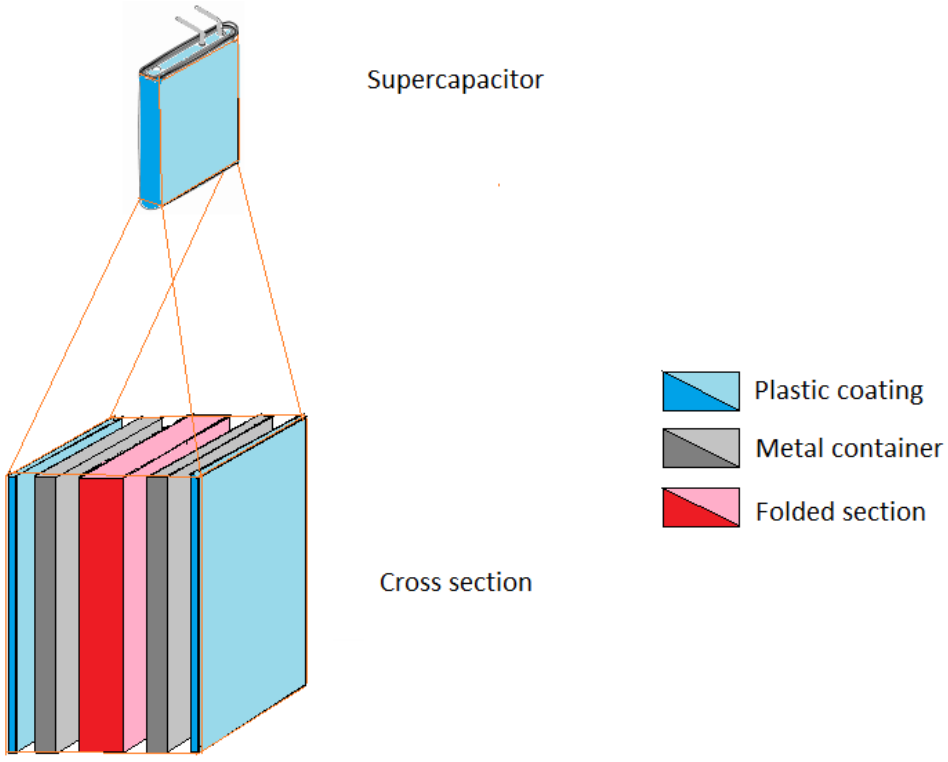

Figure 2.9: Cross section of a supercapacitor: The plastic coating is indicated in blue, the metal container in grey, and the folded capacitor section is indicated in red/pink in the middle of the cross section.

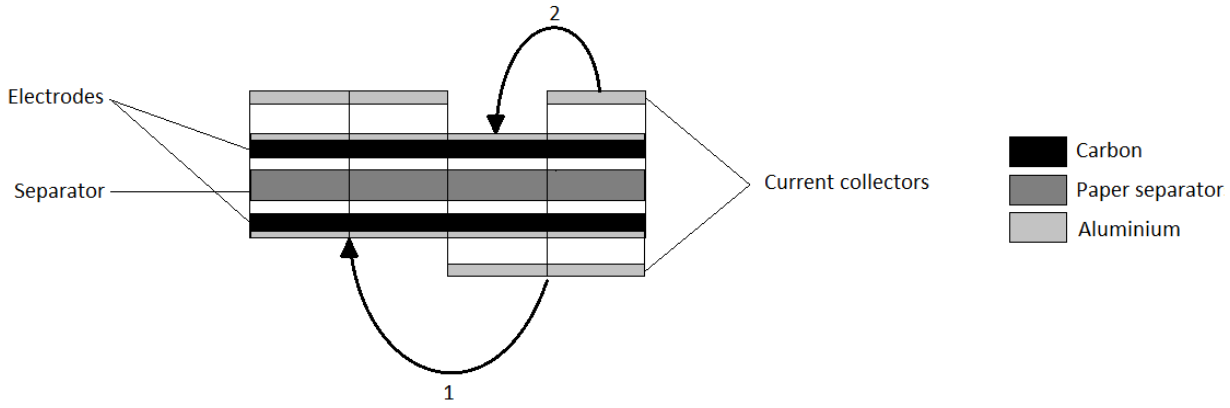

Figure 2.10: Illustration of the folded capacitor section, consisting of aluminium current collectors, a separator, and carbon/aluminium electrodes. The vertical lines illustrates where the folds are, and the numbered arrows indicate the order in which the folding is performed.

In order to determine the current density, measure the conductivity of the components, and examine the inside of the supercapacitors dissications of three supercapacitors were executed. In figure (2.9) the cross section of the supercapacitor is displayed. The folded section represent the capacitor section of the supercapacitor unit, and is illustrated in more detail in figure (2.10). The main componens in the capacitor section are the aluminium current collectors, the paper separator, and the carbon/aluminium electrodes. The vertical lines in the figure illustate where the folds are, and the numbered arrows indicate the order in which the folding is performed. In table (2.1) the thicknesses of the supercapacitor components and the number of layers through the supercapacitor stack, in the axial direction, are presented. The area of the electrodes was found to be $\mathrm{A}_{\mathrm{electrode}} = 2.5 \pm 0.05\,\mathrm{cm} \times 7.2 \pm 0.05\,\mathrm{cm} = 18.00 \pm 0.73\,\mathrm{cm}^2$.

2.3.2 Isothermal Calorimetry

In the following, the results from the isothermal calorimery of the supercapacitors, carried out at a reference temperature of $30 \pm 0.1\,^{\circ}\mathrm{C}$, are presented. Three supercapacitor stacks were tested, each for three cycling experiments, cycling the supercapacitor stacks between positive and negative potentials of $2\,\mathrm{V}$, increasing the applied current stepwise, with intervals of $0.125\,\mathrm{A}$, from no applied current (during calibration), to a maximum current of $2.000\,\mathrm{A}$. As seen from the graphs in figure (2.11), where a current of $1.000\,\mathrm{A}$ is applied while alternating the voltage between $-2\,\mathrm{V}$ and $2\,\mathrm{V}$, the applied currents and voltages are very accurate. Their errors have therefore been neglected in the

Table 2.1: The number of layers of each component material, the average thicknesses of the supercapacitor materials, and the total thickness of each material component in the axial dirction of the supercapacitor stack.

Material	Number of Axial Layers	Layer Thickness $[mm]$	Total Thickness $[mm]$
Plastic Coating	8	0.108 ± 0.026	0.862 ± 0.205
Steel Housing	8	0.331 ± 0.111	2.648 ± 0.886
Big Aluminium Current Collectors	16	0.057 ± 0.013	0.910 ± 0.213
Small Aluminium Current Collectors	4	0.041 ± 0.006	0.165 ± 0.025
Separator	16	0.066 ± 0.015	1.052 ± 0.233
Carbon/Alumininum Electrodes	32	0.223 ± 0.008	7.120 ± 0.258
Electrode Aluminium Layer	32	0.040 ± 0.016	1.280 ± 0.504
Electrode Activated Carbon Layer	32	0.183 ± 0.018	5.840 ± 0.563

error estimates in the following models. In practice, cycling the supercapacitors between positive and negative potentials means changing the charge of the electrodes, forcing the ions of the electrolyte to travel back and forth from the electrodes. A slight drop in potential is observed as the current changes direction, but its effect is consedered to be insignificant. The experimental procedures are described in section (2.2.1), and the results from these experiments are used to determine the the temperature gradient, the entropy production, σ, and the thermal conductivity, λ, according to thermal condudctivity model I.

Temperature Profiles

The temperature profiles obtained during the cycling of the supercapacitors showed a clear second degree trend, as is to be expected from the theory of model I for obtaining the thermal conductivity of the supercapacitor stack. From figure (2.13) it is evident that the temperature increases in response to the increase in applied current. The temperature profiles obtained in the experimental series for a single supercapacitors stack (in experiment A1 to A3, B1 to B3, and C1 to C3), show almost no deviations within each series. No mechanical adjustments were carried out between each experiment in an experimental series for, which is most likely the reason why the temperature profiles are as reproducible as displayed in figure (2.12), for the B series experiements. The temperature profiles of the A and C series experiments showed similar reproducibility. When changing the supercapacitor stack, sandwiched in the calorimeter, the temperature profiles are lower for the B and C series than for the A series, and the C series temperature profiles are lower than temperature profiles of the B series. The temperature profiles of experiment A1, B1 and C1 is presented in figure (2.13). Possible

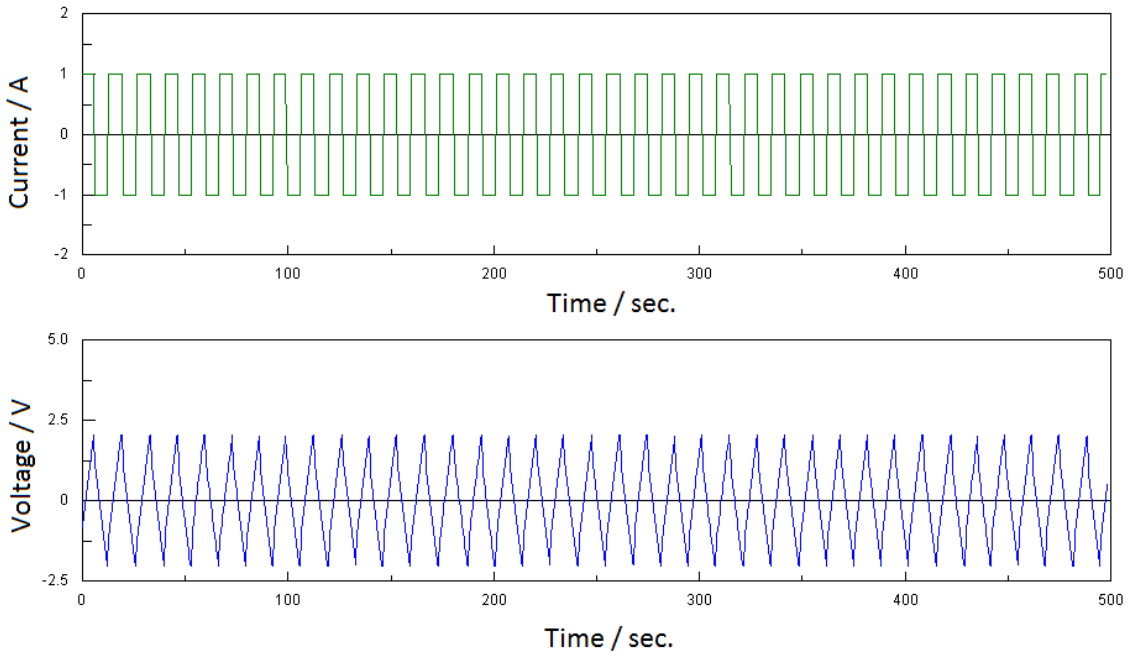

Figure 2.11: Example of the applied currents and voltages during the first 500 seconds of cycling of the supercpacitor stack. Here for cycling between positive and negative voltages of $2.000\,\mathrm{V}$, and corresponding positive and negative currents of $1.000\,\mathrm{A}$ (corresponding to a current density of approximately $j = 56\,\mathrm{mAcm}^{-2}$).

reasons for the decreasing trend in the temperature profiles of the B and C series experiments is not known, but is assumed to be due to either a decrease compression of the stack between the calorimer, or the fact that the ohmic resististance of the supercapacitor stacks in the B and C series experiments are lower than the ohmic resistance of the stack used in the A series experiments. The slight decrease in the ohmic resistance of the B and C series supercapacitor stacks, compared to the A series stacks, does not explain the decrease in temperature profiles between the respective stacks. Therefore the compation pressure is assumed to be the decisive factor.

The temperature at the interface between the supercapacitor stack and the aluminium plates of the calorimeter calibrated to be $30 \pm 0.1\,^{\circ}\mathrm{C}$ during the calibration at zero current. As the applied current is increased the temperature at the respective interface has typically increased to approximately $0.4\,^{\circ}\mathrm{C}$ to $0.6\,^{\circ}\mathrm{C}$ higher than the initial temperature, when reaching $2.000\,\mathrm{A}$. This could indicate that the calorimeter is not able to accept all the heat produced by the supercapacitors. This effect related to the sensibility of the heat measurement has been calibrated for, as described in appendix C.2.

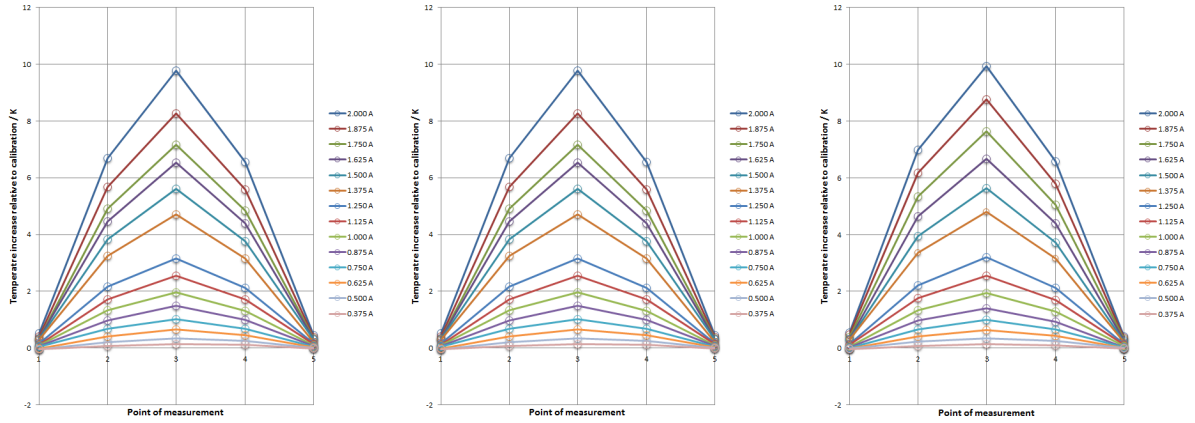

(a) Experiment B1 (b) Experiment B2 (c) Experiment B3

Figure 2.12: Heat production from the supercapacitors in in the first experiments of the A, B and C series experiments.

Therefore the heat produced is expected to be accurate enough for the modelling of the supercapacitor stack system. The increase in temperature at the interface is also taken account for both in the approximation of the thermal conductivity in model I, and when calculating the entropy production of the supercapacitor stack. When compared to the temperature increase in the intrinsic positions, between the supercapacitors, this temperature increase can anyway be considered to be negligible. The inaccuracy in the symmetry of the temperature profiles is directly linked to the positioning of the thermocouples between the supercapacitors. In the introductory project carried out by Hauge [1], less care was taken when positioning the thermocouples at the center of the interfaces between the supercapacitors, and hence even less symmetrical temperature profiles, than the profiles obtained in the experimental series described in this thesis, were obtained.

The symmetry of the temperature profile is an important parameter when calculating the thermal conductivity, using model I. The second degree symmetry of the temperature profiles become even more evident when the maximum temperature measured at thermocouple position T_3 is plotted as a function of the applied current squared, I^2, as presented in figure (2.14). In this plot it is clear that a significant change in temperature takes place as the cycling current exceeds $1.375\,\mathrm{A}$. This phenomenon is also observed when modelling the thermal conductivity, using model I described in section (2.1.2), and the generated heat, presented in the next section. The thermal conductivity, λ, reaches a steady value, and the generated heat increases linearly when exceeding this current level, indicates that at the current levels below $1.375\,\mathrm{A}$, the generated heat can be considered to be insignificant for the models presented in this chaper.

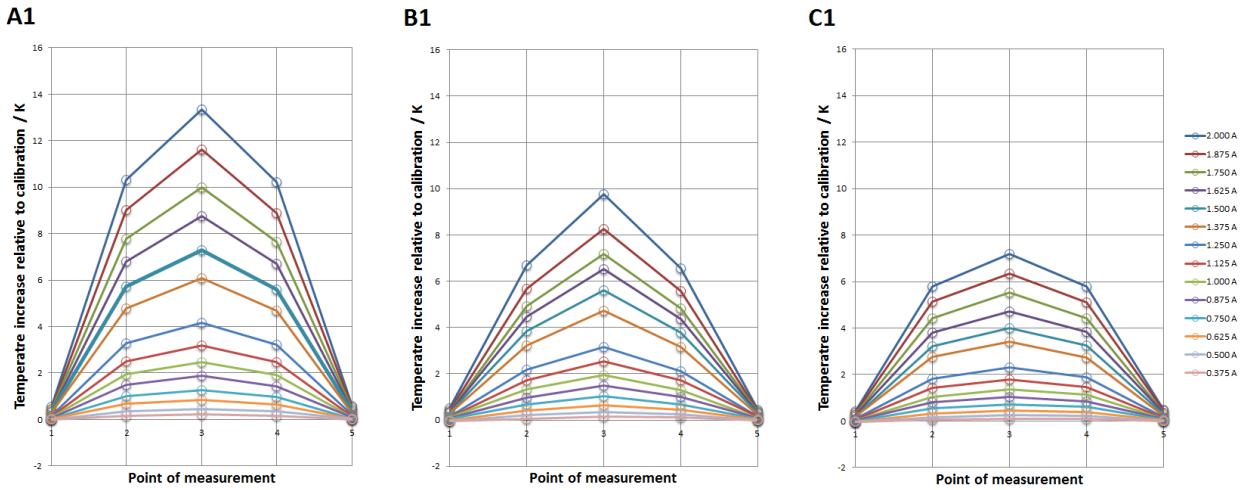

Figure 2.13: Temperature profiles of experiment A1, B1 and C1.

Heat and Entropy Production

In figure (2.15) the ohmic heat expected from passing current through the device, RI^2, and the heat produced by the thermoelectric device are plotted as a function of the applied current squared, I^2, for experiment A1, B1 and C1, respectively. The heat produced by the supercapacitor stack seem to fit relatively well with the corresponding ohmic heat. The fact that the values for the generated heat exceeds the values of the ohmic heat, weakens the credibility of these values to a certain extent. Another contributing factor that also weakens the the credibility of these results is that the generated heat is not a directly measured value, but is measured as a function of the expected sensitivity of the heaters, with respect to a resistive wire, as described in appendix C.2. The values for the generated heat presented in figure (2.15) should therefore be regarded as qualitative values, as the real values may not coincide with the calibrated values, and hence also the error bars of the plotted values is expected to be larger than the ones presented in the figure.

In order to determine the source of the entropy production, the possible contributors to entropy production must be investigated. There is no chemical reaction taking place in a supercapacotor, as the energy storing process is strictly physical; therefore this contribution is neglected. Another possible contributing factor, that has been neglected in this model, is the effect from polarization of the electrolyte. This effect has been described for water by Bresme et al. [39], but as the cycling reaches a stationary state the change in polarization, with respect to time, is expected to be equal to zero, and hence this term also cancels out. The two remaining possible contributions derive from the thermal

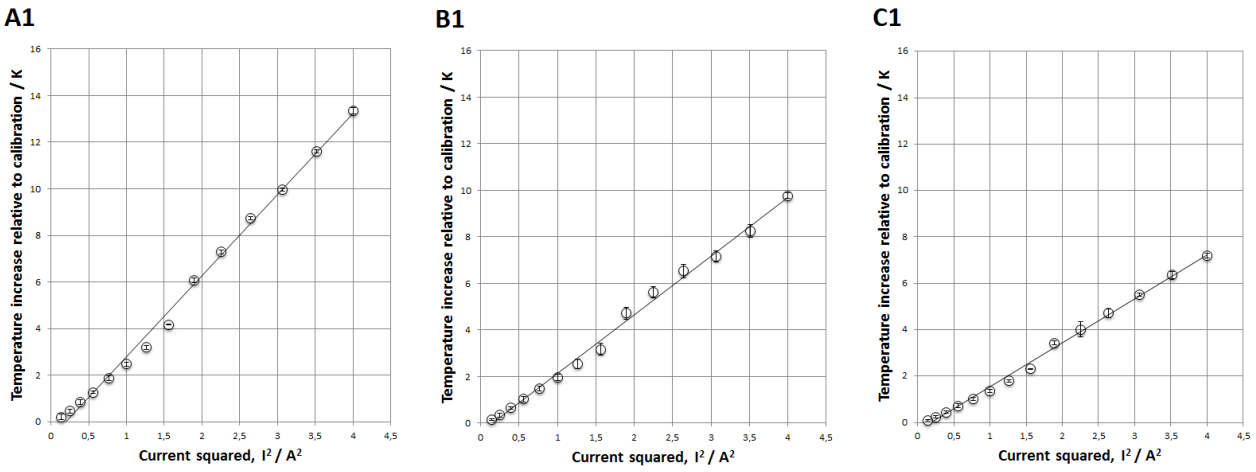

Figure 2.14: Maximum temperature profile of the first experiements of the A, B, and C series experiments, plotted as a function of the applied current squared, I^2.

and electric resistance of the device, described by equation (2.62). In order to determine which of the two terms that contribute the most to the entropy production, the electric contribution, equal to the first term of equation (2.62), will be compared to the total entropy production, calculated by equation (2.65). As the two terms of equation (2.62), in theory, should equal the total entropy production in equation (2.65), the difference between the total entropy production from equation (2.65), and the second term of equation (2.62), is therfore expected to equal the contribution from the thermal resistance (the second term of equation (2.62)).

In figure (2.16) the total entropy production, $\frac{dS_{irr}}{dt}$, calculated from equation (2.65), and the second term of equation (2.62) are plotted as a function of the the applied current squared, I^2. The generated heat showed a linear trend at cycling current above $1.375\ \mathrm{A}$, when plotted as a function of the applied current squared, I^2, therefore the same effect is observed for the total entropy production, as it derives directly from the measured heat. As seen from the figure the values for the electric contribution to the entropy production turned out to be much smaller than the corresponding values for the total entropy production, by four to six orders of magnitude. On the other hand, the heat flux, J_q, rises from the ohmic heat production in the first place, and therefore the most important factor for handelig the entropy production, is the thermal conductivity. Moreover, since the error of the heat measurement is expected to be maximally one order of magnitude off the real value, the contribution from electric resistance to the total entropy production can be neglected. Due to this error, deriving from the heat measurements, the values for the entropy production of the total entropy production, $\frac{dS_{irr}}{dt}$, should also only be regarded as qualitative values, as their precision is unknown.

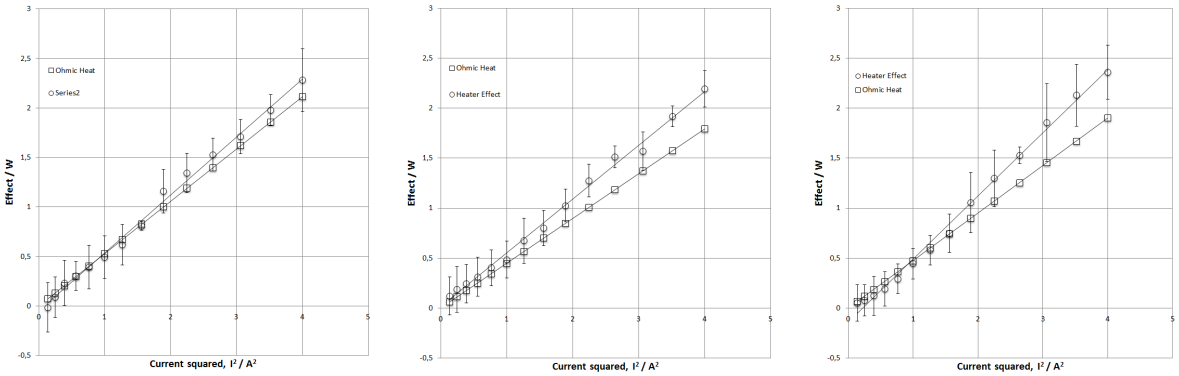

(a) Experiment A1 (b) Experiment B1 (c) Experiment C1

Figure 2.15: Heat production from the supercapacitors in in the first experiments of the A, B and C series experiments.

In order to minimize the energy loss, when storing electric energy in the supercapacitors, the first term of equation (2.62), related to the thermal resistance of the supercapacitor materials, is the main factor contributing to the loss of exergy. According to equation (2.62), maximizing the thermal conductivity of the supercapacitor materials, λ, corresponds to minimizing the the first term of the equation. As the second term of the equation has proved to give a negligible contribution to the total entropy production, the thermal conductivity, λ, can be regarded to be the most important factor to take into consideration when designing exergy efficient supercapacitors. In the following section the thermal conductivity of the supercapacitors is investigated in detail.

2.3.3 Thermal Conductivity

Several means were taken in order to study the thermal conductivity of the supercapacitors. From the experiments described in section (2.2.3) the thermal conductivity of all the materials of the Maxwell PC-10 series supercapacitors, λ_{i}, are determined. Two models for the total thermal conductivity of the supercapacitor stack were tested. The first model, model I, uses an approximative sum of least squares method, presented in section (2.1.2), to obtain the total thermal conductivity of the stack, λ using the the total ohmic resistance of the supercapacitor stack, $\mathrm{R}_{\mathrm{stack}}$, the geometry of the stack, and the axial temperature gradient across the stack, as parameters. The second model, model II, for which the theory is also described in section (2.1.2), uses the thermal conductivities of the materials from which the supercapacitors are made, λ_{i}, to determine the total thermal conductivity of the stack, λ_{stack}.

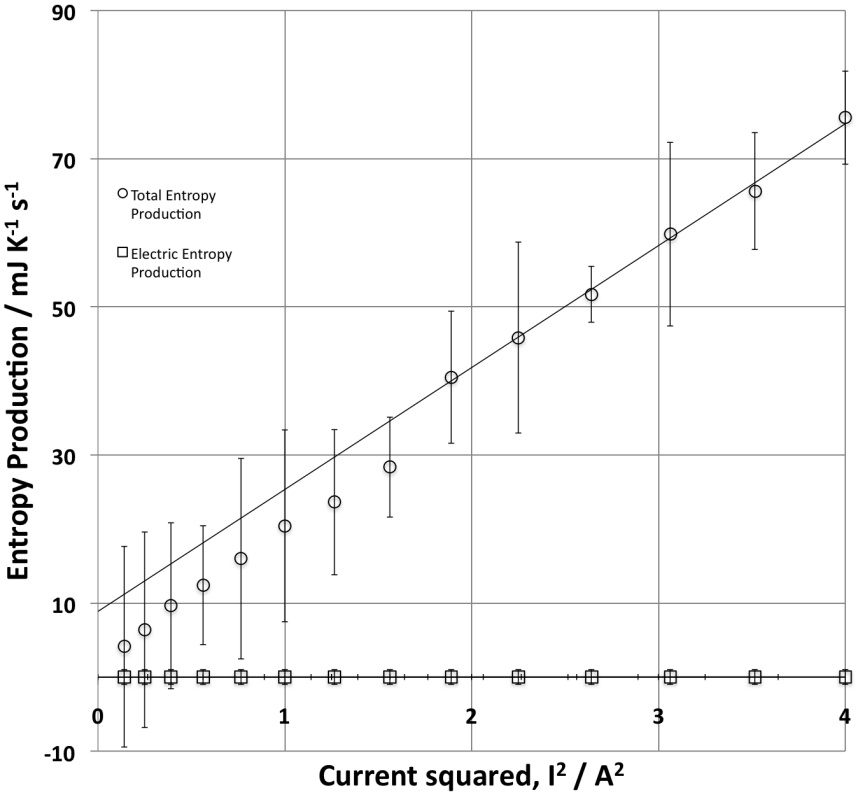

Figure 2.16: Plot of the total entropy production described in equation (2.65), $\frac{dS_{irr}}{dt}$, and the second term of equation (2.62) describing the electric contribution to the entropy production, for experiment B1.

Thermal Conductivity Model I: The Sum of Least Squares Method

In figure (2.17) the thermal conductivities of the supercapacitor stack, λ_{stack}, obtained by using the sum of least squares method described in the theory, are plotted as a function of the applied current, for experiment A1, B1 and C1. In table (2.2) all the thermal conductivities from the three experiemtal series are presented. As the increase in temperature is higher in the A series experiments compared to the B and C series experiments, the respective thermal conductivities, λ_{stack}, in these experiments are also higher, as the temperature increase is expected to arise from the thermal resistivity of the supercapacitor materials, which evidently is lower in the B and C series experiments than in the A series experiments.

The temperature profiles of the three experiments within each experimental series are approximately equal, as illustrated earlier, therefore their respective thermal conductivities are also fairly similar, as can be seen from table (2.2). The fact that the thermal conductivities reaches a steady value at $1.375\,\mathrm{A}$ indicates that the heat production can therefore be regarded as insignificant for the modelling of the thermodynamics of the supercapacitor stack prior to this state.

By rearranging equation (2.18), we see that the obtained thermal conductivity is proportional to the ohmic heat divided by the temperature difference. Thus, the thermal conductivity will reach a steady value, when the ohmic heat is so large that the temperature difference is related to the ohmic heat, and only that. For instance for low ohmic heat we record a too small temperature difference, and thus obtain to a high a value for the thermal conductivity. This can be due to the heat leakage of some kind. e.g. that the heat is lead at side of the supercapacitror housing or ambient air.

The discrepancy between the obtained thermal conductivities, of each experimental series, is directly linked to the difference in temperature increase, as the only other factor changing in the modelling is the ohmic resistance, R, that is a little higher for the A series supercapacitor stack. Hence, since the temperature difference between the A and the C series experiments is approximately given by a factor of 2, the difference in thermal conductivity is given by the same factor, in accordance with equation (2.18). As the compaction pressure is expected to be the reason for the discrepancy between the obatined values, the thermal contact between the supercapacitors is regarded to be an extremely important factor. Equation (2.18) can therefore be redefined to also take account for the compaction pressure, by multiplying the right hand side of the equation by a compaction factor, β, as illustrated in equation (2.66)

$$\Delta T = \frac{RI^2}{2\lambda w h \delta}\left(\frac{\delta^2}{4} - x^2\right)\beta \tag{2.66}$$

where β is a dimensionless unit.

Further, it is considered a strength of the model that it is able to approximate the thermal conductivity to a consistent and approximately constant value. In the background project [1], where the method for this kind of characterization was estabilieshed, less care was taken, and therefore the corresponding results for the thermal conductivity, reached no decisive value for the thermal conductivity. This illustrates the importance of placing the thermocouples at symmetrical positions, at the center of the supercapacitor interfaces.

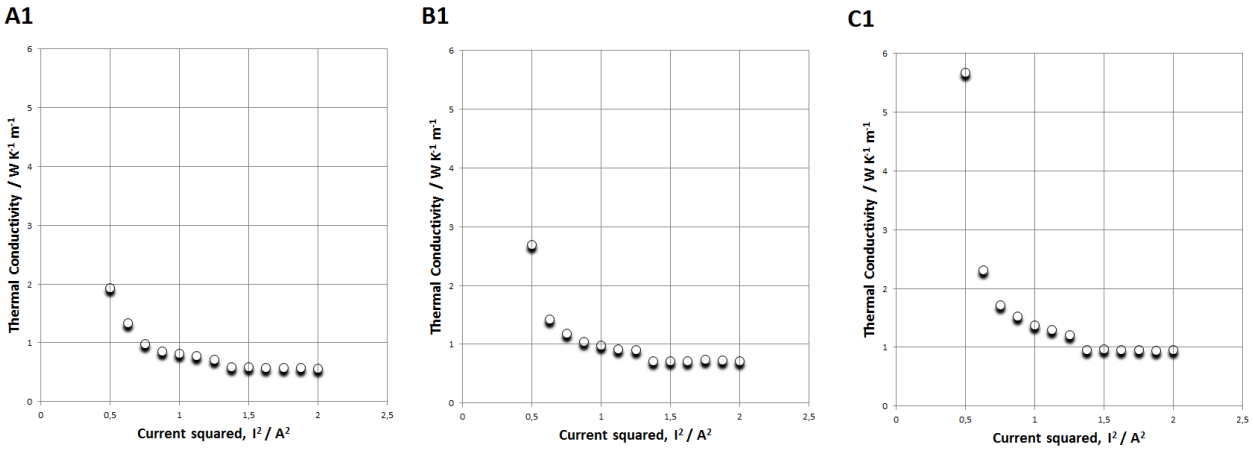

Figure 2.17: Thermal conductivity, λ_{stack}, obtained by using model I on the experimental results from experiment A1, B1, and C1.

Table 2.2: Thermal conductivities, λ, determined from experiemental data at cycling currents between 1.375 A and 2.000 A

Experimental series	Thermal conductivity, λ / $WK^{-1}m^{-1}$		
	Experiment 1	Experiment 2	Experiment 3
A	0.58 ± 0.02	0.57 ± 0.04	0.54 ± 0.04
B	0.72 ± 0.03	0.70 ± 0.01	0.69 ± 0.01
C	0.96 ± 0.02	0.95 ± 0.02	0.95 ± 0.02

Thermal Conductivity Model II: Obtaining the Thermal Conductivity from the Components

To obtain the total thermal conductivity of the supercapacitor stack using model II, the thermal conductivities of the materials, λ_{i}, constituting the supercapacitor structure had to be determined experimentally. The experimental method described in section (2.2.3) was used to obtain the thermal conductivitis of the aluminium current collectors, λ_{Al}, the carbon/aluminium electrodes, λ_{el}, the plastic coating, λ_{pl}, the separator between the electrodes, λ_{sep} and the steel housing, λ_{steel}, at different compaction pressures. From these results the thermal conductivity of the activated carbon layer of the electrodes can also be obtaind, as will be described more in detail later on in this section.

In table (2.3) the thermal conductivities of the supercapacitor materials, derived from the measurements of the thermal resistivities and sample thicknesses, presented in appendix B.1.1, are listed. The thermal conductivities were determined at compaction pressures of $4.6\,\mathrm{bar}$, $9.2\,\mathrm{bar}$, $13.8\,\mathrm{bar}$ and

$16.1\,\mathrm{bar}$ during compression, and at $4.6\,\mathrm{bar}$ during decompression. The compaction pressure within the supercapacitors is not known, and the apparatus did not allow lighter compression than $4.6\,\mathrm{bar}$ to be applied to the samples. Therefore the thermal conductivities measured during compression and decompression will be averaged when applied to the model for determining the total thermal conductivity of the supercapacitor stack, λ. As seen from table (2.3) the thermal conductivities of the components generally tend to increase as the compaction pressure is increased, except for the thermal conductivities of the steel housing which show a decreasing trend as the compaction pressure is increased. It should be noted that the thermal conductivity of the steel samples was determined with samples that were not entirely flat, due to the shape of the steel housing, and the high mechanical strengt of the material.

The cross sectional area of the supercapacitors is needed in order to determine the thermal conductivity through the stack, using model II. The cross sectional area chosen for this model is of the size corresponding to one quarter of the average electrode area, $A_{cs} = 2.5\,\mathrm{cm} \times 1.8\,\mathrm{cm} = 4.5\,\mathrm{cm}^2$. Analysing figure (2.10) this is assumed to be a reasonable approximation of the cross sectional area, as it encloses the area through which the heat flux has to travel through all the constituing layers. The area not included in the cross sectional area, $\mathrm{A_{cs}}$, consists mainly of the radial parts of the steel casing and the plastic coating, which do not contribute to the internal heat production, and since the shape of the steel housing and plastic coating causes these regions for the most part not to be in direct contact with the adjacent supercapacitors, their contribution to the axial heat transport is assumed to be negligible. The cross sectional area of $A_{cs} = 4.5\,\mathrm{cm}^2$, is therefore considered to be a reasonable parameter in the model, in which it is assumed to be constant.

In table (2.4) the averaged thermal conductivities of the components are presented, together with the total thermal resistivities of the respective materials, $\mathrm{r_i}$. The thermal resistivities of the material components, r_i, are calculated by rearranging equation (2.24), using the averaged thermal conductivities, λ_i, the cross sectional area of $A_{cs} = 4.5\,\mathrm{cm}^2$, and the total thicknesses of the material components, δ_i, presented in table (2.1), as parameters. Summing the component material resistivities, according to equation (2.25), the effective thermal resistivity of the supercapacitor stack is found to be $r_{stack} = 81.590 \pm 11.292\,\mathrm{K\,m^2\,W^{-1}}$. Dividing the total thickness of all the supercapacitor stack, $\delta = 1.3 \pm 0.1\,\mathrm{cm}$, obtained from summing all the component layers in the axial direction, on the effective resistivity, r_{stack}, multiplied with the cross sectional area, $\mathrm{A_{cs}}$, as described in equation (2.26), the effective thermal conductivity of the supercapacitor stack is found to be $\lambda_{stack} = 0.347 \pm 0.055\,\mathrm{WK^{-1}m^{-1}}$. This value is based on that the measurements of the steel casing are correct, but the samples used to determined the thermal conductivity of the steel were not perfectly flat, and it is very possible that the mechanical strength of the steel has caused air to occupy major parts of the intrinsic area between the steel samples, and hence given rise to a thermal resistance that is not representative for the material. By using a standard steel thermal conductivity of $15\,\mathrm{WK^{-1}m^{-1}}$ instead of the value given in table (2.4), and neglecting the standard deviation of this

parameter, an effective thermal conductivty of $\lambda_{stack} = 0.531 \pm 0.064\,\mathrm{WK^{-1}m^{-1}}$ is obtained.

Comparing the two models for the thermal conductivity, λ_{stack}, the values obtained from model II is smaller than all the effective thermal conductivities obtained using model I in the B and C experimental series, but for the A experimetal series the fit between the two models is good. Having carried out numerous dissecations of the supercapacitors, it is regarded unlikely that the compaction pressure inside the supercapacitors has exceeded the compaction pressures applied in the determination of the component material thermal conductivities, λ_{i}, in model II. This implies that the compaction pressure can not be regarded the reason for the misfit between the two models, as the thermal conductivity generally is expected to increase with increasing compaction pressure. On the other hand, the discrepancy of the thermal conductivities from model I is assumed to be the compaction pressure of the supercapacitors within the calorimeter. The two models do therefore show common effective thermal conductivities when the compaction pressure in the calorimeter is high enough.

There are three other possible reasons for the discrepancy between the two models; namely that the encapsuling of the supercapacitors may give the major contribution to the thermal conductivity of the supercapacitor stack estimated in model I, that the effective thermal conductivity may vary from the center to the edge, or that the thermal paste between the supercapacitors in the calorimetric experiments has given the rise to a higher thermal conductivity than what has been taken account for in model II. A high conductance of the thermal paste, that is neglected in model II, would give a positive contribution to the thermal conductivity in model I, that has not been taken account for in model II. This may also be to to the plastic, and contact resistance between the plastic and the steel housing. Hence, there is good reason to assume that the real value of the effective supercapacitor stack thermal conductivity, λ_{stack}, can be expected to be somewhere in between the values obtained from model I and II.

Studying the thermal resistivities displayed in table (2.3), and assuming that the thermal conductivity of the steel casing is closer to $15\,\mathrm{WK^{-1}m^{-1}}$ than the questionable values obtained from the experiments, it is evident that it is the activated carbon/aluminium electrodes reside the highest thermal resistivity of the constituent material layers. Assuming that the aluminium of the electrodes are made from the same material as the current collectors, the main contribution to the thermal resistivity of the electrodes is the activated carbon layer. Connecting this observation to the the analysis of the entropy production, described by equation (2.62), being inversely proportional to the thermal conductivity of the supercapacitor materials, it can be concluded that the activated carbon layer of the electrodes give the major contribution to the entropy production, and hence the loss of exergy in the energy storing process.

Using equation (2.26) reversibly for the activated carbon/aluminium electrodes, with the area of the circular samples as the area parameter, $\mathrm{A_{sample}} = \pi \left(\frac{21.0 \pm 0.1\,\mathrm{mm}}{2}\right)^2$, and assuming that the aluminium

layer of the electrodes are made from the same material as the aluminium current collectors, the thermal conductivty of the activated carbon is found to be $\lambda_C = 0.19 \pm 0.10\,\mathrm{WK^{-1}m^{-1}}$. The large uncertainty is related to the uncertainty in the thickness of the two layers, as the thickness was determined as the difference in thickness before and after removing the layer mechanically, with a scalpel. The average value is places itself close to the value of dry the dry activated carbon supercapacitor electrode material reported by Burheim et al. [36], of $0.13 \pm 0.01\,\mathrm{WK^{-1}m^{-1}}$. The corresponding value for the activated carbon soaked in 1 M $\mathrm{TEA-BF_4}$ was reported to be $0.47 \pm 0.04\,\mathrm{WK^{-1}m^{-1}}$. 1 M $\mathrm{TEA-BF_4}$ was also used in the experimental procedure of the model II experiments, when determining the thermal conductivity of both the electrodes and the separator, in order to recreate the conditions within the supercapacitors in the best way possible. The reason for the discrepancy between the two models could be due to different preparation of the activated carbon materials tested, or less soaked electrodes in this experiement, than in the corresponding experiment carried out by Burheim et al.,as acetonitrile evaporates very quickly.

2.3.4 Further Work

The investigation of the supercapacitors is very thorough, but there are some aspects that could be investigated more in detail, and with higher precision. This concerns the measurement of the heat leaving the supercapacitors during cycling, and hence an accurate measurement of the total entropy production. Another interesting aspect that should be investigated, is the ratio between the capacitance of supercapacitor electrodes, with respect to their thermal conductivity, as this can be considered to be a good indication of the capacity of the device with respect to its thermal efficiency, based on the findings of the experimental work presented in this chapter. The uncertainty in the calculation of the activated carbon electrode material should also be determined with high precision.

When designing supercapacitor banks, consisting of several supercapacitors connected in series, parallel, or a combination of the two, the compaction could prove to be an important factor, hence the compaction factor, β, defined in equation (2.66), might be an interesting factor to investigate more in detail.

Table 2.3: Thermal conductivities, λ, of the material components of the supercapacitors, at compression pressures of $4.6\,\mathrm{bar}$, $9.2\,\mathrm{bar}$, $13.8\,\mathrm{bar}$ and $16.1\,\mathrm{bar}$ during compression, and $4.6\,\mathrm{bar}$, during decompression, listed in the respective order.

Material	Compaction pressure [bar]	Thermal conductivity, λ_i $[WK^{-1}m^{-1}]$
Aluminium Current Collectors	4.6	0.633 ± 0.310
	9.2	0.970 ± 0.490
	13.8	1.271 ± 0.672
	16.1	1.435 ± 0.777
	4.6	1.223 ± 0.739
Carbon/Aluminium Electrodes	4.6	0.641 ± 0.021
	9.2	0.618 ± 0.031
	13.8	0.650 ± 0.008
	16.1	0.671 ± 0.019
	4.6	0.663 ± 0.032
Plastic Coating	4.6	0.104 ± 0.020
	9.2	0.130 ± 0.027
	13.8	0.122 ± 0.012
	16.1	0.125 ± 0.012
	4.6	0.123 ± 0.013
Separator	4.6	0.201 ± 0.011
	9.2	0.215 ± 0.034
	13.8	0.220 ± 0.036
	16.1	0.227 ± 0.051
	4.6	0.245 ± 0.085
Steel Housing	4.6	0.224 ± 0.102
	9.2	0.195 ± 0.057
	13.8	0.185 ± 0.032
	16.1	0.188 ± 0.023
	4.6	0.236 ± 0.028

Table 2.4: Average thermal conductivity of the supercapacitor component materials, λ_{i}, and their respective thermal resistivities relative to the total material thicknesses through the axial direction in the supercapacitor stack, $\mathrm{r_i}$.

Material	Thermal Conductivity, λ_i $[WK^{-1}m^{-1}]$	Thermal Resistivity, r_i $[K\,m^2\,W^{-1}]$
Aluminium Current Collectors	1.106 ± 0.278	2.159 ± 0.694
Activated Carbon/Aluminium Electrodes	0.649 ± 0.011	24.394 ± 0.970
Plastic Coating	0.121 ± 0.008	15.861 ± 3.922
Separator	0.222 ± 0.022	10.554 ± 2.570
Steel Housing	0.206 ± 0.025	28.621 ± 10.203

2.4 Conclusion

Embedding thermocouples between a stack of commercial supercapacitors, analyzed in the ligth of the first law of thermodynamics, a thermal conductivity, λ_{stack}, between $0.5\,\mathrm{WK^{-1}m^{-1}}$ and $1.0\,\mathrm{WK^{-1}m^{-1}}$, is obtained.

Measuring the thermal conductivity of each component independently, an effective thermal conductivity of $\lambda_{stack} = 0.531 \pm 0.064\,\mathrm{WK^{-1}m^{-1}}$, is obtained.

When evaluating stacks of supercapacitors, the contact between the single supercapacitors appears the most important factor for the overall heat management. When evaluating the effective thermal conductivity of each single supercapacitor, the thermal conductivity of the active electrode is the most important factor.

According to our second law analysis, thermal conductivity appears to be the most important factor for the entropy production.

Chapter 3

Thermoelectric Generators

3.1 Theory

This section is dedicated to provide the necessary theory for evaluating the thermoelectric efficiency of the thermoelectric module tested in the experimental work described in section (3.2). Section (3.1.1) introduces a short summary of the history of the discovery of thermoelectricity, followed by examples of their practical use and the material factors deciding their efficiency. Section (3.1.2) describes how the thermoelectric modules are designed, and in section (3.1.3) the irreversible thermodynamics used to calculate the entropy production and efficiencies of the module is derived.

3.1.1 Thermoelectricity

The thermoelectric effect was discovered in the 19^{th} century through three important discoveries by the Baltic German scientist Thomas Johan Seebeck (1770–1831), the French scientist and watchmaker Jean Charles Athanase Peltier (1785–1845) and the British physisist William Thomson, later named Lord Kelvin (1824–1907). In 1821 Seebeck accidentally discovered that a junction of two dissimilar metals produce an electric current when exposed to a temperature gradient, which is now called the Seebeck effect. The discovery was done as he made a circuit from two dissimilar metals (copper and bismuth), with junctions at different temperatures, and discovered that the circuit deflected compas needles. He first thought this was due to magnetism, but it was later found that it was actually due to an induced current running through the circuit. 13 years later, in 1834, Peltier found the reverse effect; a heat difference generated from an electric voltage, when a current passed through a circuit of two

dissimilar conductors, called the Peltier effect. In 1851 Thomson dicovered that a spatial gradient in temperature resulted in a gradient in the Seebeck coefficient, and that when a current is driven through this gradient a continous version of the Peltier effect occured, called the Thomson effect. Thereby the heating or cooling of a current-carrying conductor, with a temperature gradient, was determind, also known as the thermoelectric effect. The discovery established the theory of the interedependency of the Seebeck and Peltier effect, known as the Kelvin relations [22, 40, 41].

As the doping of semiconductors was discovered, thermoelectrics experienced a technical revolution. In the beginning the technology was used in both Peltier refridgerators in the household [42], and even in the Pioneer space programs to generate power from the temperature gradient between the radioactive decay of radioactive material (usually Pu-238, Sr-90, or Cm-244) and the outside temperature in space. The use of various kinds of radioisotope thermolectric generators has since also been used in most space programs, including the Voyager program, lately in the robotic rover Curiosity on Mars, and also in unmanned facilities, such as in Russian lighthouses in remote locations, far from human settlements [43]. The technology is also used for other means such as in thermocouples used for temperature measurements and control, which have been used in almost all experimental work of this master thesis. Typically K-type thermocouples, consisting of thin chromel and alumel wires, are used to determine the temperature from a voltage drop of $40.6\,\mu\mathrm{V\,K^{-1}}$ [41].

The low efficiency, usually of about $5\,\%$, does however limit the use of thermoelectric generators to use where cost is not a main consideration. This applies to green technology where the supply of heat is cheap, or even free, as in the case of waste heat, e.g. from the casting process in an aluminum plant, where the efficiency of the conversion system is not an overriding consideration [44].

For a given temperature regime of operation the conversion efficiency, that is the electric power out to the heat input, of a thermoelectric generator is dependent only on the performance of the thermocouple material, expressed through the figure of merit, Z, displayed in equation (3.1).

$$Z = \frac{\kappa\,\eta_s^2}{\lambda} \tag{3.1}$$

where κ is the combined electric conductivity, η_s is the Seebeck coefficient, and λ is the thermal conductivity. Established thermoelectric materials have relatively well defined temperature regions of operation. The maximum figures of merit, $\mathrm{Z_{max}}$, decreases as the operating temperature increases, and consequently a more meaningful material performance indicator is the dimensionless figure of merit, ZT, where T is the absolute temperature, and the best materials have a value of a round unit.

3.1.2 The Design of Themoelectric Generators

The thermoelectric modules can operate in two different modes, namely in the Peltier mode, operating as a heat pump, or in the Seebeck mode, operating as a heat engine. In the Peltier mode heat is transported from the cold to the hot side of the module, at temperatures $\mathrm{T_c}$ and $\mathrm{T_h}$, respectivly, as a current is passing through the circuit of the device. When operated in the Seebeck mode, heat transported from a heat source, at a temperature $\mathrm{T_h}$, to a heat sink, at a temperature $\mathrm{T_c}$, induces a current through the module. The technology behind the thermoelectric modules is based on so-called thermocouples, which consist of a pair of n- and p-type semiconductors that can be regarded as the 'monomer' of the device. In a thermoelectric module several thermocouples are connected with electric conductors, usually in series. The thermocouples are sandwiched between two electrically insulating, but thermally conducting, ceramic plates that also serve as a constructional support. When operated in the Seebeck mode the power output from a single thermocouple is small, therefore many thermocouples in series are needed in order to create a power output that can be used for practical means, as the potential created is proportional to the number of thermocouples in the module [42,45]. In figure (3.1) a sketch of the basic structure of a thermoelectric module is displayed.

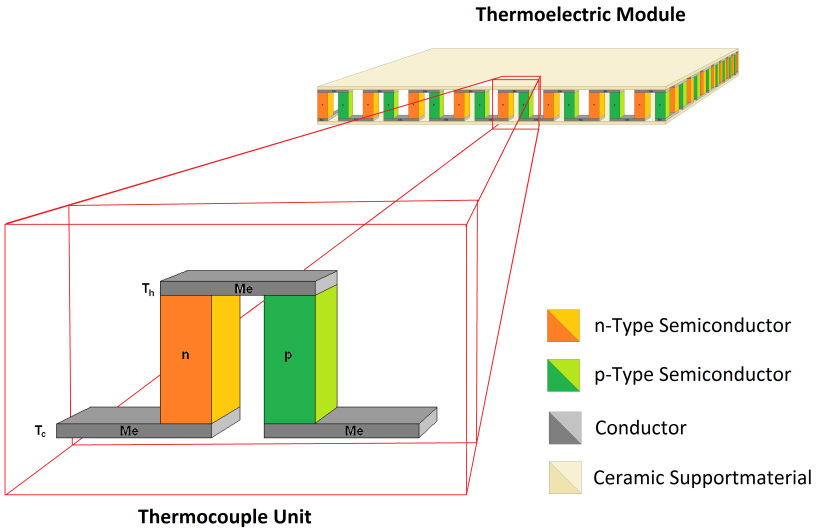

Figure 3.1: Structure of a thermoelectric module

3.1.3 Derivation of the Thermodynamics behind Thermoelectric generators

The following theory is based on theory presented by Kjelstrup et. al. [4, 22]. The fact that there is no chemical reaction taking place in the thermoelectric modules while operated in the Peltier and Seebeck mode, makes the entropy production of the module only dependent on the heat and current fluxes. This means that the same general expression for the entropy production in a homogeneous phase used for the supercapacitors, previously expressed in equation (2.45), can be used also for the thermoelectric generators. The frame of reference in the theoretical approach is a single semiconductor thermocouple unit, as illustrated in figure (3.1). In the following a few of the basic equations, already derived for the supercapacitors in the previous chapter, will be reproduced in order to make the derivations for a thermoelectric module as clear as possible.

The Entropy Production

The entropy production, σ, is described by the conjugate forces and fluxes of the heat and the electric current, as displayed in equation (3.2),

$$\sigma = J'_q \frac{\partial}{\partial x}\left(\frac{1}{T}\right) + j\left(-\frac{1}{T}\frac{\partial \phi}{\partial x}\right) = J'_q\left(-\frac{1}{T^2}\frac{\partial T}{\partial x}\right) + j\left(-\frac{1}{T}\frac{\partial \phi}{\partial x}\right) \tag{3.2}$$

where J'_q is the measurable heat flux, j is the current density, and $\frac{d}{dx}\frac{1}{T}$ and $-\frac{1}{T}\frac{d\phi}{dx}$ are their respective conjugate forces. Using the Onsager reciprocal relations, the flux equations for the measurable heat flux, $\mathrm{J'_q}$, and the current density, j, can be expressed as equation (3.3) and (3.4), respectively.

$$J'_q = L_{qq}\left[\frac{\partial}{\partial x}\frac{1}{T}\right] + L_{q\phi}\left[-\frac{1}{T}\frac{\partial \phi}{\partial x}\right] = -L_{qq}\frac{1}{T^2}\frac{\partial T}{\partial x} - L_{q\phi}\frac{1}{T}\frac{\partial \phi}{\partial x} \tag{3.3}$$

$$j = L_{\phi q}\left[\frac{\partial}{\partial x}\frac{1}{T}\right] + L_{\phi\phi}\left[-\frac{1}{T}\frac{\partial \phi}{\partial x}\right] = -L_{\phi q}\frac{1}{T^2}\frac{\partial T}{\partial x} - L_{\phi\phi}\frac{1}{T}\frac{\partial \phi}{\partial x} \tag{3.4}$$

As previously described equation (3.3) can be transformed into an expression for the thermal conductivity, λ by equating the current density to zero, and equation (3.4) can be transformed into an expression for the electric conductivity, κ, when the temperature difference is zero. The resulting equations for the thermal and electric conductivity are displayed in equation (3.5) and (3.6), respectively.

$$\lambda \equiv -\left[\frac{J_q^{'}}{\frac{\partial T}{\partial x}}\right]_{j=0} = \frac{1}{T^2}\left[L_{qq} - \frac{L_{\phi q}L_{q\phi}}{L_{\phi\phi}}\right] \tag{3.5}$$

$$\kappa = -\left[\frac{j}{\frac{d\phi}{dx}}\right]_{dT=0} = \frac{L_{\phi\phi}}{T} \tag{3.6}$$

The Peltier coefficient, π, is related to the Seebeck coefficient through the Onsager reciprocal relations. It is defined as the heat being transfered reversibly per unit charge, with the electric current at constant temperature, as defined in equation (3.7):

$$\pi \equiv F\left[\frac{J_q^{'}}{j}\right]_{dT=0} = F\frac{L_{q\phi}}{L_{\phi\phi}} \tag{3.7}$$

As the current travels through the circuit, the electrons experience an inabsolute kinetic change in entropy, when traveling from one material phase to another, relative to a reference compound. In this regard the Peltier coefficient can be expressed as equation (3.8)

$$\pi \equiv T\,S^* \tag{3.8}$$

Using the Onsager reciprocal relations revealed in equation (3.3) through (3.7), the measureable heat flux, $J_q^{'}$, and the current density, j, can be redefined as equation (3.9) and (3.10), respectively.

$$J_q^{'} = -\lambda\frac{\partial T}{\partial x} + \frac{\pi}{F}j \tag{3.9}$$

$$j = -\frac{\kappa\pi}{FT}\frac{\partial T}{\partial x} - \kappa\frac{\partial\phi}{\partial x} \tag{3.10}$$

By introducing equation (3.9) and (3.10) into the expression for the entropy production, in equation (3.2), the entropy production can be re-expressed as equation (3.11).

$$\sigma \;=\; \frac{\lambda}{T^2}\left(\frac{dT}{dx}\right)^2 + \frac{j^2}{T\,\kappa} \;=\; \frac{\lambda}{T^2}\left(\frac{dT}{dx}\right)^2 + \frac{r\,j^2}{T} \tag{3.11}$$

To derivate the total entropy production in the thermocouple, the local entropy production, σ will have to be integrated over the volume of the respective thermocople according to equation (3.12).

$$\frac{S_{irr}}{dt} = \int \sigma \, dV \tag{3.12}$$

Introducing equation (3.11) into equation (3.12) a final expession for the toal entropy production through the thermocouple is obtained in equation (3.13).

$$\frac{S_{irr}}{dt} = \Omega \int_0^l \left(\frac{\lambda}{T^2} \left(\frac{dT}{dx} \right)^2 + \frac{r\, j^2}{T} \right) dx \tag{3.13}$$

The Electric Potential

The important process taking place in the thermoelectric modules is the the process of creating an electric potential that can be used to restore thermal energy, that would otherwise be lost to the environment. Rearranging equation (3.10), and introducing equation (3.8) into it, the gradient in electric potential can be defined as equation (3.14)

$$\frac{\partial \phi}{\partial x} = -\frac{S^*}{F} \frac{dT}{dx} - r\, j \tag{3.14}$$

By integrating equation (3.14) from terminal to terminal in the semicunductor thermocouple, and neglecting the contact resistances between the thermocouple compounds, an expression for the electric potential difference, $\Delta\phi$, is obtained, as shown in equation (3.15).

$$\Delta\phi = \int_0^l \left(-\frac{S_n^*}{F} \frac{dT}{dx} - r_n\, j \right) dx \; + \; \int_0^l \left(-\frac{S_p^*}{F} \frac{dT}{dx} - r_p\, j \right) dx \tag{3.15}$$

where l is the the length of the semiconductor bulk pieces illustated in figure (3.1), $\mathrm{S_n^*}$ and $\mathrm{S_p^*}$ are the transported entropies of the p- and n-type semiconductors, and $\mathrm{r_n}$ and $\mathrm{r_p}$ are their respective ohmic resistances. The contributions from the electric conductors connecting the semiconductors are not included in equation (3.15), as they cancel each other out.

When combining the integrals in equation (3.15) and introducing the Seebeck coefficient, equation (3.16) is obtained.

$$\Delta\phi = \int_0^l \left(\frac{S_p^* - S_n^*}{F} \frac{dT}{dx} - (r_n + r_p)\, j \right) = \int_0^l \left(\frac{\Delta S^*}{F} \frac{dT}{dx} - r_{total} j \right) \tag{3.16}$$

where $\Delta\mathrm{S}^*$ is the change in change in transported entropy, when electrons are transfered between the n- and p-type semiconductors of the thermocouple, and $\mathrm{r_{total}}$ is the sum of the ohmic resistivities in the semiconductors. The electric potential difference is in other words genrated between the two terminals because there is a difference in the transported entropy of the charge carriers in the semiconductors. By identifying the Seebeck coefficient as $\eta_\mathrm{s} = \frac{\Delta \mathrm{S}^*}{\mathrm{F}}$, the change in electric potential can be redefined as equation (3.17).

$$\Delta\phi = \int_0^l \left(\eta_s \frac{dT}{dx} - r_{total} j \right) \tag{3.17}$$

By assuming that the transported entropies are independent of temperature and integrating over the length of the semiconductor pieces the electric potential is defined by equation (3.18).

$$\Delta\phi = \eta_s \left(T_h - T_c\right) - l\, r_{total}\, j \;=\; \eta_s\, \Delta T - l\, r_{total}\, j \tag{3.18}$$

When analysing equation (3.18) it becomes evident that the maximum electric potential is obtained when the current density is equal to zero, $\mathrm{j} = 0$, equal to the reversible potential, also known as the electromotive force/emf, E. The other contribution comes from the internal resistance of the thermocouple. According to equation (3.18) the emf, E, is defined as equation (3.19).

$$E = \Delta\phi_{j=0} = \eta_s \Delta T \tag{3.19}$$

Rearranging equation (3.19), the Seebeck coefficient, η_s, can be defined as the ratio of the emf divided by the temperature difference between the hot and the cold side of the thermocouple, as presented in equation (3.20).

$$\eta_s = \left(\frac{\Delta\phi}{\Delta T} \right)_{j=0} = \frac{\Delta S^*}{F} \tag{3.20}$$

The Seebeck coefficient is related to the Peltier coefficient through the second Thomson relation given in equation (3.21)

$$\eta_s = -\frac{\pi}{F\,T} \tag{3.21}$$

The thermoelectric power is defined as the current density times the electric potential, and consequently the thermoelectric power of the thermocouple, P can be defined as equation (3.22).

$$P \equiv j\,\Delta\phi = \eta_s\,\Delta T\,j\; - r_{total}\,j^2 \tag{3.22}$$

When the thermocouple is connected to an external load, the terminal voltage is given as equation (3.23).

$$\Delta\phi_{load} = j\,r_{load}\; =\; \Delta\phi_{j=0}\; -\; j\,r_{total} = \eta_s\,\Delta T\; -\; j\,r_{total} \tag{3.23}$$

Reorganising equation (3.23) the current density, j, can be defined as equation (3.24).

$$j = \frac{\eta_s\,\Delta T}{r_{load}\; +\; r_{total}} \tag{3.24}$$

By inserting the expression for the current density in equation (3.24) into equation (3.22), then differentiating it with respect to the load resitance and assuming that the maximum power output from the thermocoule is obtained when the load resistance is equal to the inerternal resiatance of the thermocouple, $\mathrm{r_{load}} = \mathrm{r_{total}}$, the maximum power output can be expressed as equation (3.25).

$$P_{max,tc} = \frac{\left(\eta_s\,\Delta T\right)^2}{4\,r_{total}} \tag{3.25}$$

As previously noted, the thermoelectric module consists of several thermocouples connected in series. The potential from a thermoelectric module, $\Delta\phi_{\mathrm{module}}$, can therfore be defined as the number of thermocouples, N, in the module times the potental generated by a single thermocouple, as shown in equation (3.26).

$$\Delta\phi_{module} = N\Delta\phi \tag{3.26}$$

The internal resistance, R, of the intire module, consisting of N thermocouples, can similarly be defined as equation (3.27).

$$R = \frac{N\, l\, r_{total}}{\Omega} \tag{3.27}$$

where Ω is the cross section area of the bulk semiconductors in a thermocouple. When inserting equation (3.26) and (3.27) into equation (3.18), an expression for the electric potential of a module, $\Delta\phi_{\mathrm{module}}$, consisting of N thermocouples connected in series is defined as equation (3.28).

$$\Delta\phi_{module} = N\, \eta_s\, \Delta T \; - \; RI \tag{3.28}$$

The maximum power of the module can, in accordance with equation (3.25), be expressed as equation (3.29).

$$P_{max,module} = \frac{\left(N\, \eta_s\, \Delta T\right)^2}{4\, R} \tag{3.29}$$

The Efficiency of a Thermoelectric Generator

In order to determine how effective a thermoelectric generator is, the first and second law efficiencies,η_{I} and η_{II}, will have to be investigated together with the figure of merit, Z, of the module.

The First Law Efficiency The first law efficiency of a process, η_{I}, is defined as the work produced by the process, w, devided by the heat added to the process, q, as shown in equation (3.30).

$$\eta_I = \frac{w}{q} \tag{3.30}$$

In the case of the thermoelectric generator the first law efficiency can be defined as the ratio of the effect generated by the thermoelectric generator with respect to the heat added at the hot side of the generator, as displayed in equation (3.31).

$$\eta_I = \frac{P}{Q_h} \tag{3.31}$$

Using theory by Zebarjadi et al. [46], the maximum first law efficiency of the device can be related to the Carnot efficiency, $\eta_{\mathrm{C}} = \frac{\mathrm{T_h} - \mathrm{T_c}}{\mathrm{T_h}}$, together with a γ term capturing the features of the device, through equation (3.32).

$$\eta_{I,max} = \eta_C \, \gamma \; = \; \frac{T_c \, - \, T_c}{T_h} \, \frac{\sqrt{1 \, + \, Z \, \overline{T}} \, - \, 1}{\sqrt{1 \, + \, Z \, \overline{T}} \, + \, \frac{T_c}{T_h}} \tag{3.32}$$

where the $\overline{\mathrm{T}} = \frac{\mathrm{T_h} + \mathrm{T_c}}{2}$, is the average temperature at the two faces of the device, and Z is the figure of merit given in equation (3.1).

The Second Law Efficiency The second law efficiency, η_{II}, is defined as the efficiency of the process compared to the ideal process, which can be expressed in terms of the work of the process, w, compared to the work of the process carried out under ideal conditions, $\mathrm{w_{ideal}}$. This relation is directly linked to the lost work of the process, $\mathrm{w_{lost}}$, as presented in equation (3.33) for a work producing process.

$$\eta_{II} \; \equiv \; \frac{|w|}{|w_{ideal}|} \; = \; 1 \; - \; \frac{w_{lost}}{|w_{ideal}|} \tag{3.33}$$

When carrying out a process $\mathrm{T_0} \left(\frac{\mathrm{dS_{irr}}}{\mathrm{dt}}\right) \Delta \mathrm{t}$ is the additional amount of work that is needed to carry out a real process compared to the corresponding ideal process, where $\mathrm{T_0}$ is the temperature of the environment, $\Delta \mathrm{t}$ is the time interval of the process and $\left(\frac{\mathrm{dS_{irr}}}{\mathrm{dt}}\right)$ is the total entropy production. The Gouy-Stodola theorem [47] states that the lost work hence can be expressed as equation (3.34).

$$w_{lost} \; = \; w - w_{ideal} \; = \; T_0 \left(\frac{dS_{irr}}{dt} \right) \, \Delta t \tag{3.34}$$

Inserting the expression for the lost work in equation (3.34) the second law efficiency can be defined as equation (3.35).

$$\eta_{II} = 1 \; - \; \frac{T_0 \, \left(\frac{dS_{irr}}{dt}\right) \, \Delta t}{w_{ideal}} \tag{3.35}$$

When operated in the Seebeck mode as a heat engine the maximum work from the process is given by the Carnot efficiency multiplied by the heat passing through the module and the time interval, $\mathrm{w_{ideal}} \; = \; \eta_{\mathrm{C}} \, \mathrm{Q_{in}} \, \Delta \mathrm{t}$. From this the second law efficiency can be defined as equation (3.36).

$$\eta_{II} \; = \; \frac{P}{\eta_C \, Q_{in} \, \Delta t} \tag{3.36}$$

3.2 Experimental

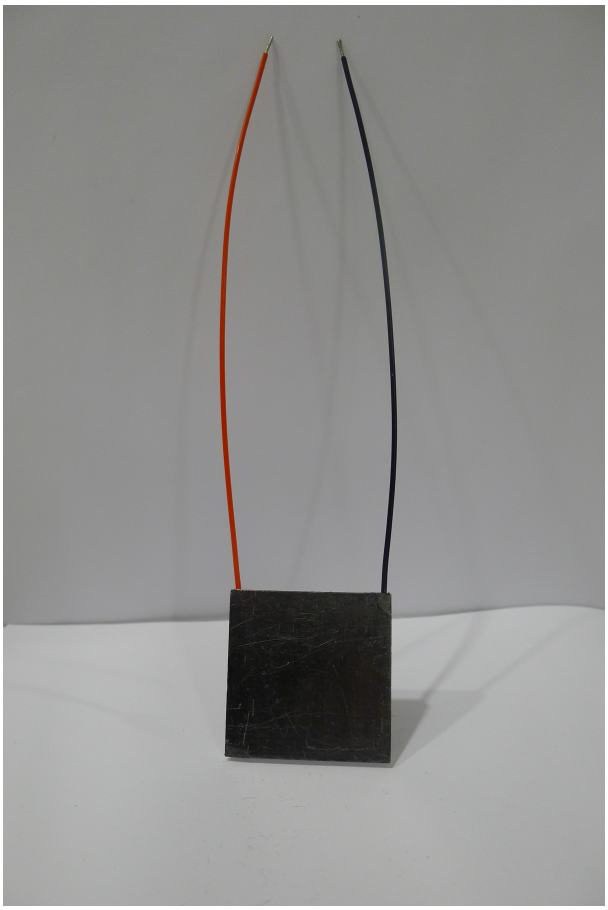

Figure 3.2: Photo of the TEP-1264-1.5 thermoelectric module, supplied by Thermo-Gen AB.

The thermoelectric module, TEP-1264-1.5, supplied by Thermo-Gen AB, illustrated in figure (3.2), consists of 126 bismuth-telluride semiconductor thermocouples connected electrically in series. The thermocouples are stacked into a $40\,\mathrm{mm} \times 40\,\mathrm{mm}$ square-shaped device, sandwiched between ceramic aluminium oxide support plates. The maximum hot side continously applied temperature of the device, is set to be $260\,^{\circ}\mathrm{C}$ by the maufactorer, and the corresponding maximum temperature at the cold side is $160\,^{\circ}\mathrm{C}$ [2].

For the thermolelectric module four different types of experiments were conducted in order to test both the Seebeck, and the Peltier mode of the thermoelectric device, and additionally determine the

module isothermal internal ohmic resitance. The experiments were carried out in such a way that they could be compared to the experiemtal results obtained by Takla [2]. The original aim of the studies of the Seebeck mode was to test the potential produced by the device, under increased externally applied loads. This goal was not obtainable using the the calorimeter as heat source and heat sink, as the temperature difference across the device was not big enough for producing an emf big enough to be altered by an external load. The typical temperature difference obtainable within the calorimeter, while still having sensitivity of the heat entering and leaving the calorimeter is typically in the range of about $\Delta T = 10\,^{\circ}\mathrm{C}$. The corresponding Seebeck mode experiment carried by Takla, with a more suited equipment, the temperature difference obtained was one order of magnitude higher, and hence the emf obatied was also higher. For the Peltier mode experiments and the experiment testing the ohmic resistance, the experimental equipment, namely the calorimeter designed by Burheim [3], is consistent with the experiemental equipment used by Takla [2].

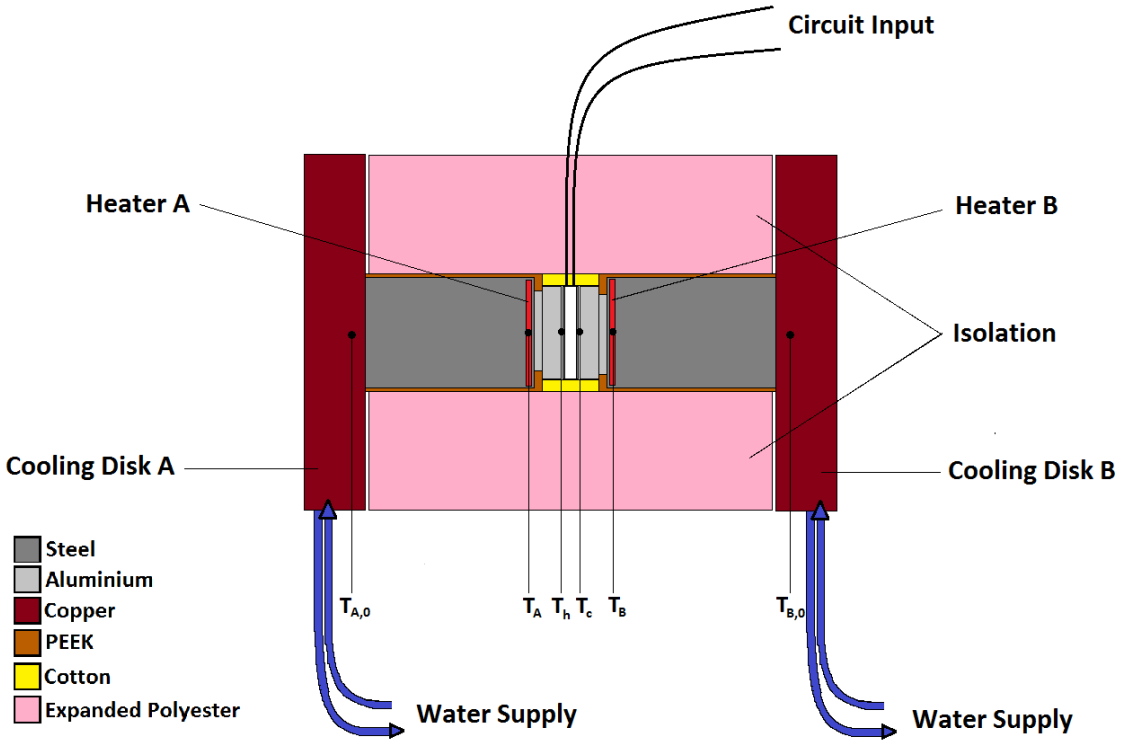

Figure 3.3: Experimental setup of the TEP -1265-1.5 thermoelectric module, sandwiched between two aluminium plates in the calorimeter. Two resistive heating wires positioned at either side of the aluminium plates, generating an axial heat flux towards the external copper cooling disks.

The experimental setup for all the experiments is illustrated in figure (3.3). Temperatures are measured with K-type thermocouples at the positions indicated with $\mathrm{T_i}$, where the subscript, i, refers to the position within the apparatus. The heaters within the effect to the heaters consists of $10\,\Omega$ resistive heating wires, controlled by two Eurotherm PID-controllers, operating in a thermostatic mode. The thermoelectric module is positioned in such a way that the left hand side of the calorimeter, pictured in figure (3.3), controlled the hot side of the device (defined by the manufactorer). The cooling necessary to maintain a constant heat flux in the axial direction through the steel rods was obtained by circulating water mixed with glycolic antifreeze, supplied by a Braun Thermomix 1441 waterbath, through two copper cooling plates posistioned at either side of the calorimeter. A more thorough description of the apparatus, supplied with the reasons for the choises of materials used in the apparatus, is given in the previous chaper. The experimental data from temperature measurements, and the effect applid to the heaters was logged by a LabView setup. In figure (3.4) the apparatus described in this section, is divided into five experimental units, as this is representative for how the apparatus is placed in the lab. In section (3.2.1) through (3.2.4), the experimental descriptions are presented.

3.2.1 Seebeck Mode Experiment

In this experiment the Seebeck mode of the device was investigated, by deterining the Seebeck coefficient of the thermoelectric module, $\eta_{S,module}$. As described in the theory, the Seebeck coefficient is defined as the emf of the module, divided by the temperature difference across the respective module. In the experimental procedure all temperatures indicated in figure (3.3) were measured, with thermocouples, and the emf of the module was measured by the Agilent 6060B System DC Electronic Load box, as the temperature difference across the device was increased by lowering T_c, relative to T_h, which was kept constant at approximately $50\,^{\circ}\mathrm{C}$ throughout the the experiment. Five measurements were carried out, with an increasing temperature difference of $2\,^{\circ}\mathrm{C}$ to approximately $8\,^{\circ}\mathrm{C}$. The Seebeck coefficient is expected to follow a linear trend when plotting the emf, as a function of the temperature difference across the module. In theory three measurements should be enough to determine a linear trend. Hence, when measuring five data points, the presence of the linear relation should be evident. Each experiement was conducted at a constant temperature difference, for at least one hour, in order to avoid temperature fluctuations, which would alter the precision of detemined the Seebeck coefficient. All data was logged by the LabView setup every second.

3.2.2 Experiment on Isothermal Internal Ohmic Resistance

In this experiment the isothermal internal ohmic resistance the of the thermoelectric generator, as a function of the average temperature of the device, $\overline{T} = \frac{1}{2}(T_h + T_c)$, was investigated. Obtaining

an equal temperature at either side of thermoelectric device was a high priority in this experiment, as isothermal conditions was a requirement. This is one of the main reasons why the thermocouples were placed at the interface, between the calorimeter and the device, and not inside the aluminium plate of the calorimeter, as practiced by Takla [2]. The temperature at the hot and cold side of the device is controlled by the Eurotherm PID-controller, which were adjusted in order to obtain an approximately equal temperatures measured at T_h and T_c, in the figure (3.3). The adjustment of the temperature could be done with a precision of approximately $\pm 0.1\,^{\circ}\mathrm{C}$. The internal ohmic resistance, R, was measured using a Agilent 4338B High Frequency Ohmmeter. The temperature was increased stepwise in the temperature range $20\,^{\circ}\mathrm{C}$ to $60\,^{\circ}\mathrm{C}$, with steps of $2.0 \pm 0.1\,^{\circ}\mathrm{C}$. The measurements were carried out for at least one hour per temperature interval, in order to be sure to have stable isothermal conditions in the system. The ohmic resistance, and the temperatures indicated in figure (3.3) were logged by the LabView setup every second during the measurements.

3.2.3 Peltier Experiment I: Applying voltage

In the first experiment testing the Peltier mode of the thermoelectric module, henceforth refered to as Peltter experiment I, the heat produced by the thermoelectric device was to be determined as a function of the voltage applied to the device. The temperature at the hot and the cold side of the device were set to an approximately equal temperature altering the effect added to the heaters, testing the effect of the experiment at both $35 \pm 0.1\,^{\circ}\mathrm{C}$, and at $50 \pm 0.1\,^{\circ}\mathrm{C}$, which is the temperature at which Takla [2] carried out the experiment. Testing the experiment also at $35 \pm 0.1\,^{\circ}\mathrm{C}$, was a measure carried out in order to try to obtain higher heat resolution.

After obtaining isothermal conditions across the device a potential was applied to the device using an Agilent E3633A Power Supply, increasing the voltage stepwise from $0.0\,\mathrm{V}$ to $2.0\,\mathrm{V}$, with steps of $0.2\,\mathrm{V}$, every hour. The effect from the heaters, the added voltages and currents, and the temperatures, indicated in figure (3.3), were logged with the LabView setup every second. The cycling was also attemped using the a Princeton Applied Reasearch 263A Potentiostat/Galvanostat, in order to test whether the observed heat insensitivty was caused by the external power supply. This turned out to be a false assumption, as the same effect was observed also with this potentiostat.

3.2.4 Peltier Experiment II: Heat Generated From Temperature Difference

In the second Peltier mode experiement, henceforth refered to as Peltier experiment II, the heat delivered to the calorimeter, as the temperature difference across the thermoelectric generator was in

increased, while applying a constant current to the module, was to be determined. The initial temperature was kept equal at both sides of the device during the initial calibration, at a temperature of $50 \pm 0.1\,^{\circ}\mathrm{C}$. Constant currents of both $0.50 \pm 0.01\,A$ and $1.00 \pm 0.01\,A$ were tested. The currents were applied from the Agilent E3633A Power Supply, as the temperature at the cold side was lowered stepwise every hour, by $1 \pm 0.1\,^{\circ}\mathrm{C}$ at a time. The temperature was lowered by adjusting the thermostat of the Eurotherm PID-controller. Also for this experiment a similar heat insensitivity was observed, and hence the Princeton Applied Reasearch 263A Potentiostat/Galvanostat was tested also for this experiment. Also with this potentiostat the heat sensitivity was evident. The insensitivity of the heat was eventually suscribed to calorimeter not having high enough resolution and the heat calibration carried out in appendix C.2 not being applicable, when heat polarization is present.

As the current of $1.00 \pm 0.01\,A$ was considered to be too high, a current of $0.50 \pm 0.01\,A$ was also tested. This did not help increasing the credibilty of the results, but it helped the device to remain within the reach of the heater sensitivty longer, as the generted ohmic heat was lower.

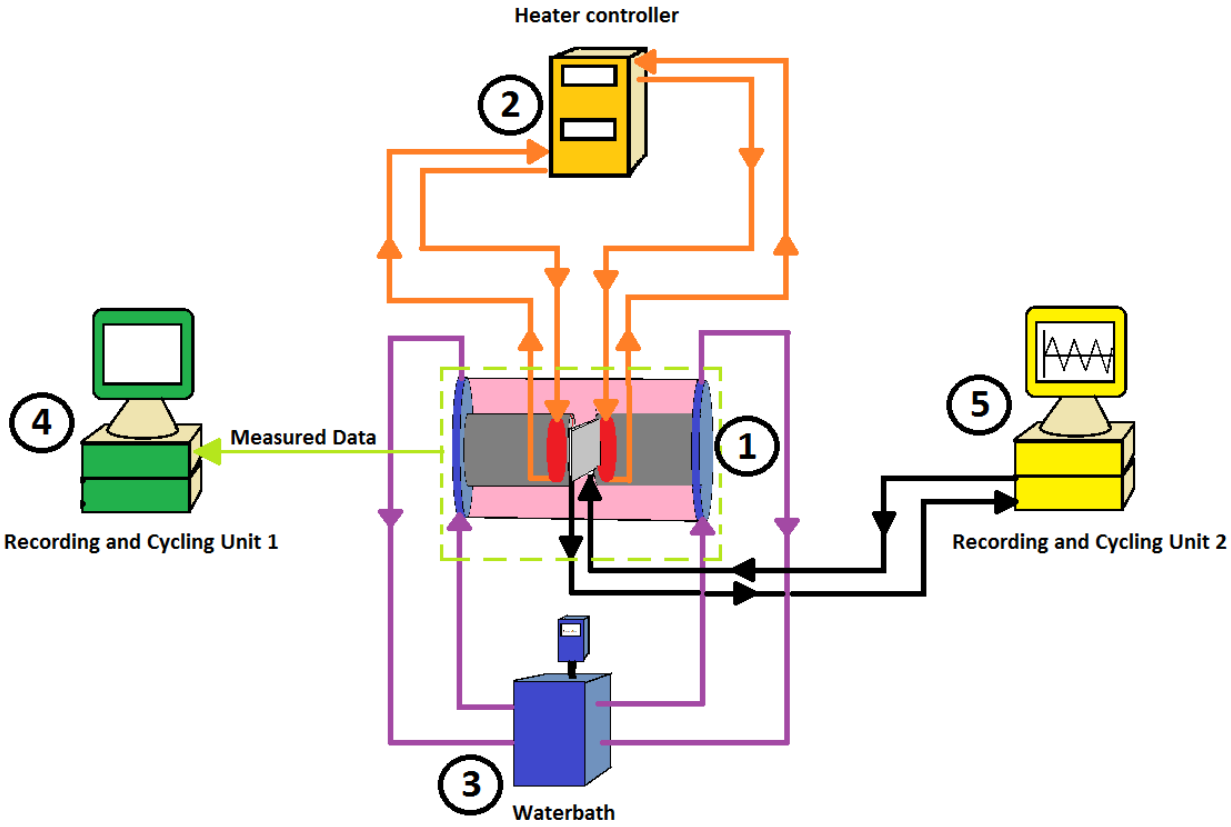

Figure 3.4: Experimental set-up of the caliorimetric studies of thermoelectric generators. In the figure the five experimental units used during the experiments are presented. (1) The calorimeter unit: Consisting of a TEP-1264-1.5 thermoelectric module, by Thermo-Gen AB, sandwiched between the two symmetrical parts of a calorimeter designed by Burheim [3]. The heat flux through the horizontal directions is ensured by two heaters located at each end plate facing the center, and two cooling copper plates at the two external faces of the calorimeter. (2) Heater controller: A double Eurotherm PID-controller controlling the effect delivered to the two heaters inside the calorimeter by keeping the temperature constant during measurements. The circuits of the resistancy threads inside of the two heaters are indicated with orange lines. (3) Waterbath: A Braun Thermomix 1441 waterbath, mixed with glycolic antifreeze, delivering a flux of cold liquid to the external copper cooling plates of the calorimeter. The two water fluxes are indicated by purple lines. (4) Recording and Cycling Unit 1: Consists of a Agilent 4338B Milliohmmeter, an Agilent E3633A Power Supply, an Agilient 6060B System DC Electronic Load, and computer with a LabView software recording experimental data from the calorimeter unit. The overall acquistation of data from the experiment is indicated with green lines. (5) Recording and Cycling Unit 2: Consisting of a Princeton Applied Research 263A Potentiostat/Galvanostat connected with a computer with a CorrWare software for control and recording of the applied voltages and currents. The circuit of the cycling from the Potentiostat/Gavvanostat is indicated with black lines.

.

3.3 Results and Discussion

In the following the results from the experiments described in the experimental section (3.2) are presented and discussed. The results are presented as average values with a double standard deviation, corresponding to a 95 % confidence interval, in accordance with the theory on error estimates presented in appendix A. In the experimental procedures one experiment testting the thermoelectric module's Seebeck mode, two experiements testing the Peltier mode, and additionally one experiment to test the isothermal internal ohmic resistance of the module when increasing the resective external interface isothermal temperatures.

The Seebeck Mode Experiment

The Seebeck experiment is carried out in accordance with the experimental description given in section (3.2.1). As mentioned previously, the emf, $\phi_{\mathrm{j}=0}$, obtained from the module at the maximum obtainable temperature difference between the two external interfaces of the device, $\Delta\mathrm{T}$, turned out to not be too small to be tested with external loads, therefore the experimental procedure had to be altered in order to obtain the Seebeck coefficient of the device, which is closely connected to the efficiency of the device, through the figure of merit, Z, displayed in equation (3.1).

In figure (3.5) the emf of the thermoelectric generator, measured as the temperature difference across the device, $\Delta\mathrm{T}$, is increased from approximately $2\,^{\circ}\mathrm{C}$ to $8\,^{\circ}\mathrm{C}$, is plotted as a function of the temperature difference across the device. The corresponding Seebeck coefficients are presented in table (3.1). The average Seebeck coefficient from these experiments is $\eta_{S,module} = 40 \pm 3\,\mathrm{mV/K}$, meaning that the average Seebeck coefficient of each single theromocouple, of the totally 126 thermocouples within the module, is $\eta_{S,tc} = 319 \pm 20\,\mu\mathrm{V/K}$. Using the slope, presented in figure (3.5), to determine the Seebeck coefficient a vlaue of $\eta_{S,module} = 38 \pm 7\,\mathrm{mV/K}$ is obtained, corresponding to a Seebeck coefficient of $\eta_{S,tc} = 300 \pm 60\,\mu\mathrm{V/K}$ for the single thermocouples. The Seebeck coefficient determined by the slope of the trend line in figure (3.5) is based on the assumption that the Seebeck coefficient is constant and independent of the temperature difference applied across the device. When comparing the values obtained in these experiements, at relatively low temperatures and low temperature differences, to the corresponding Seebeck coefficient obtained by Takla [2], using a temperature differences that are one order of magnitude larger, an intersting effect is observed. Takla [2] obtained a Seebeck coefficient of $\eta_{\mathrm{S}} = 30 \pm 1\,\mathrm{mV/K}$ using the slope of the trendline of the emf plotted as a function of as the temperature difference across the device. The Seebeck coefficient obtained with a smaller temperature difference is approximately $27\,\%$ larger than the Seebeck coefficient obtained at temperature differences of higher magnitude, indicating that the efficiency of the module decreases drastically as the temperature gradient across the device is increased. The assumption that the See-

Table 3.1: Overview of the Seebeck coefficients, η_S, calculated from the emf produced by the thermoelectric module, $\phi_{\mathrm{j}=0}$, divided by the temperature difference, $\Delta\mathrm{T}$, graphically displayed in figure (3.5), with 95 % confidence interval values.

$\Delta\mathrm{T}$ $[K]$	$\phi_{\mathrm{j}=0}$ [mV]	η_{S} $[mVK^{-1}]$
$2,2 \pm 0,1$	97,0	43 ± 9
$3,5 \pm 0,1$	146,0	42 ± 6
$4,7 \pm 0,2$	180,0	38 ± 6
$6,3 \pm 0,1$	228,9	36 ± 3
$8,0 \pm 0,1$	329,0	$40,9 \pm 1,9$

beck coefficient is constant, is therfore only valid for specified temperature intervals, though it should be kept in mind that the uncertainty in the experiement of this thesis is about one order of magnitude larger than the corresponding value obtained by Takla [2].

When determining the Seebeck coefficent, the temperature is measured at the interface between the ceramic heat conducting support layer, sandwiching the semicunductor thermocouples, and the calorimeter. The Seebeck effect arises from a temperature gradient afflicted uppon the semiconductor structure, forcing a transport of entropy across the different phases of the thermocouple bulk materials. The support material is not a part of the semiconductor structure in itself, therefore when determining the Seebeck coefficient of the thermoelectric module, $\eta_{S,module}$, the thermal conductivity of the support material is assumed to be so large, that the temperature gradient across the ceramic support material is negligible.

As seen from table (3.1), the double standard deviations of the emf measurements are of a negligible magnitude, indicating that the emf, $\phi_{\mathrm{j}=0}$, generated by the thermoelectric module, is more dependent on the average temperature difference across the device, than on the fluctuations of respectve temperatures.

No credible value was obtained for the heat flow through the device in these measurements, and hence the thermal conductivity, λ, used to determine the figure of merit, Z, defined in equation (3.1), was not obtained. The first and second law efficiencies, η_{I} and η_{II}, defined in equation (3.31) and (3.36), also require the heat flow through the device, and hence also their values are not obtianed. The reason for this is that the calorimeter has a high uncertainty in the heat registered by the heaters. Alternatively the thermal conductivity of the device could have been calculated using the heat flux, obtained from the temperature gradient across the steel rods of the calorimeter (using the same theory described in the previous chapter, for determining the thermal conductivity of the supercapacitor materials). This method requires an accurate value of the thermal conductivity of the steel rods, λ_{steel}, but the type of

steel used in the calorimeter is not known, and therefore also this method is considered invalid for determining the figure of merit, Z, of the device.

3.3.1 The Experiment on Isothermal Internal Ohmic Resistance

The ohmic resistance of the thermoelectric module was measured as the isothermal temperature at either side of the device was increased with temperature intervals of $2 \pm 0.1\,^{\circ}\mathrm{C}$ from $20.0 \pm 0.1\,^{\circ}\mathrm{C}$ to $60.0 \pm 0.1\,^{\circ}\mathrm{C}$. In figure (3.37) the measured total ohmic resistance, R, is plotted as a function of the average temperature at the interfaces of the device, $\overline{\mathrm{T}} = \frac{\mathrm{T_h} + \mathrm{T_c}}{2}$, is presented. As seen from the figure, the total ohmic resistance, R, increases with increasing average temperature, $\overline{\mathrm{T}}$, and the linear trend line prove an almost perfect fit to the linear relation presented in equation (3.37), describing the total ohmic resistance of the device.

$$R = 1.394 + 0.007\,\overline{T} \tag{3.37}$$

where the unit of total ohmic resistance, R, is $[\Omega]$ and the unit of average temperature, $\overline{\mathrm{T}}$, is $[^{\circ}\mathrm{C}]$. When comparing the plot of the experimental results, obtained in this experiment, to the corresponding experimental results of Takla [2], it is evident that the accuracy of the measurements is increased. Takla reports a standard deviation in the measurments of the ohmic resistance of $\pm 0.01\,\Omega$, which is the approximate value of the corresponding double standard deviation of the experiements presented in figure (3.37). Additionally the results show a better fit to the linear trend, which is assumed to be due to the much more accurate temperature measurements, obtained by measuring the temperature at the interface between the aluminium plate of the calorimeter, and the thermoelectric module, instead of from the inside of the aluminium plate, which was the case in the experiments descibed by Takla [2]. Takla reports an inaccuracy of the average temperature of about $1\,\mathrm{K}$, but the corresponding double standard deviation is two orders of magnitude smaller for the values presented in figure (3.6), and their error bars are therefore barely visible in the figure.

The ohmic resistance obtained by Takla [2] is described as $R = \left(1.403 + 0.00758\,\overline{T}\right)\,\Omega$. When comparing equation (3.37) to the corresponding relationship described by Takla, a negative misfit of $9\,\mathrm{m}\Omega$ in the intercept of the secondary axis of ohmic resistance, when the average temperature is $\overline{T} = 0\,^{\circ}\mathrm{C}$, and regarding the slope of the regression line a negative misfit of $0.00058\,\Omega\mathrm{K}^{-1}$ is observed. This difference is considered to be negligible, although equation (3.37) is considered to posses the highest accuracy.

3.3.2 The Peltier Mode Experiments

The experimental results of the Peltier mode of the thermoelectric device turned out to not be fit for a qualitative analysis of the device. The reason for this is that the values for the measured heat, obtained from the experiments, proved to be off the expected range, with at least one order of magnitude, even when not using the senistivity factors obtained from appendix C.2. The reason for the low heat resolution of the calorimeter is expected to be caused by the heat polarization not being applicable for the calibration done for isothermal conditions, even when calibrating each side of the calorimeter independently. In order to obtain credible results for heat passing through the device, the heat sensitivity of the calorimeter must therefore be increased. As the time at hand was limited, these possible measures, listed later in this section, was not obtainable, within the given time frame of this thesis.

Practically, the reason for the insensitivity of the calorimeter can be credited to the measureable heat, at the hot side of the thermoelectric device reaching the minimum effect already at appied currents of $0.6\,\mathrm{A}$ in Peltier experiment I, which in the corresponding experiement carried out by Takla [2], is considered to be outside the valid measuring range of the calorimeter. Since the thermoelectric device tested is the same, this indicates that the calorimeter was able to accept more heat during Takla's experiments, and that this feature has been degraded over the approximately three years between the experiments. The same effect was observed in Peltier experiment II. When applying a current of $1.000\,\mathrm{A}$, the heat sensitivity at the hot side of the device was lost, and even when lowering the applied current to $0.5\,\mathrm{A}$, the same heat insensitivity described for Peltier experiment I was observed.

One feature of the Peltier mode, independent of the heat sensitivity of the calorimeter was obtained in Peltier experiment I. As the added current and voltage was measured, together with the temperatures across the thermoelectric module, the effect added to the device is given as, $P = UI$, where U is the voltage, in [V], and I is the current in [A]. According to Ohm's law, this effect is expected to be directly proportional to the ohmic heat, given as RI^2, where R is the ohmic resistance, in [Ω], calculated by from the linear relation for the isothermal resistivity, obtained from figure (3.6). As seen from the plot in figure (3.7), the ohmic heat proved to be lower than the corresponding values for the added potential. As the two curves are expected to overlap, this indicates that when operating with a temperature gradient, and with applied currents, the ohmic resistance is higher than under isothermal emf conditions.

3.3.3 Further Work

Consistently from all the work thoughout all this thesis, an important challenge was related to determining a precise heat measured from a PID-controlled resistance. This means that further work in

relation to this thesis is to improve the means to measure heat. There is in principle at least two ways in which the sensitivity of the measured heat can be increased. One is to insert thermocouples in the steel cyclinders, between the copper heaters and the copper coolers, see figure (3.3). This, of course, requires precise knowledge of the thermal conductvity of the steel in the calorimeter. The other approach would be to use Peltier modules at zero current. This can be done because the corresponding potential will be directly proportianal to the heat flux through the Peltier element. Another challenge with this is that it requires a calibration, and also a linearity in the sence that one applies a Peltier module to characterise the same Peltier module, and this lowers the credibility of the method.

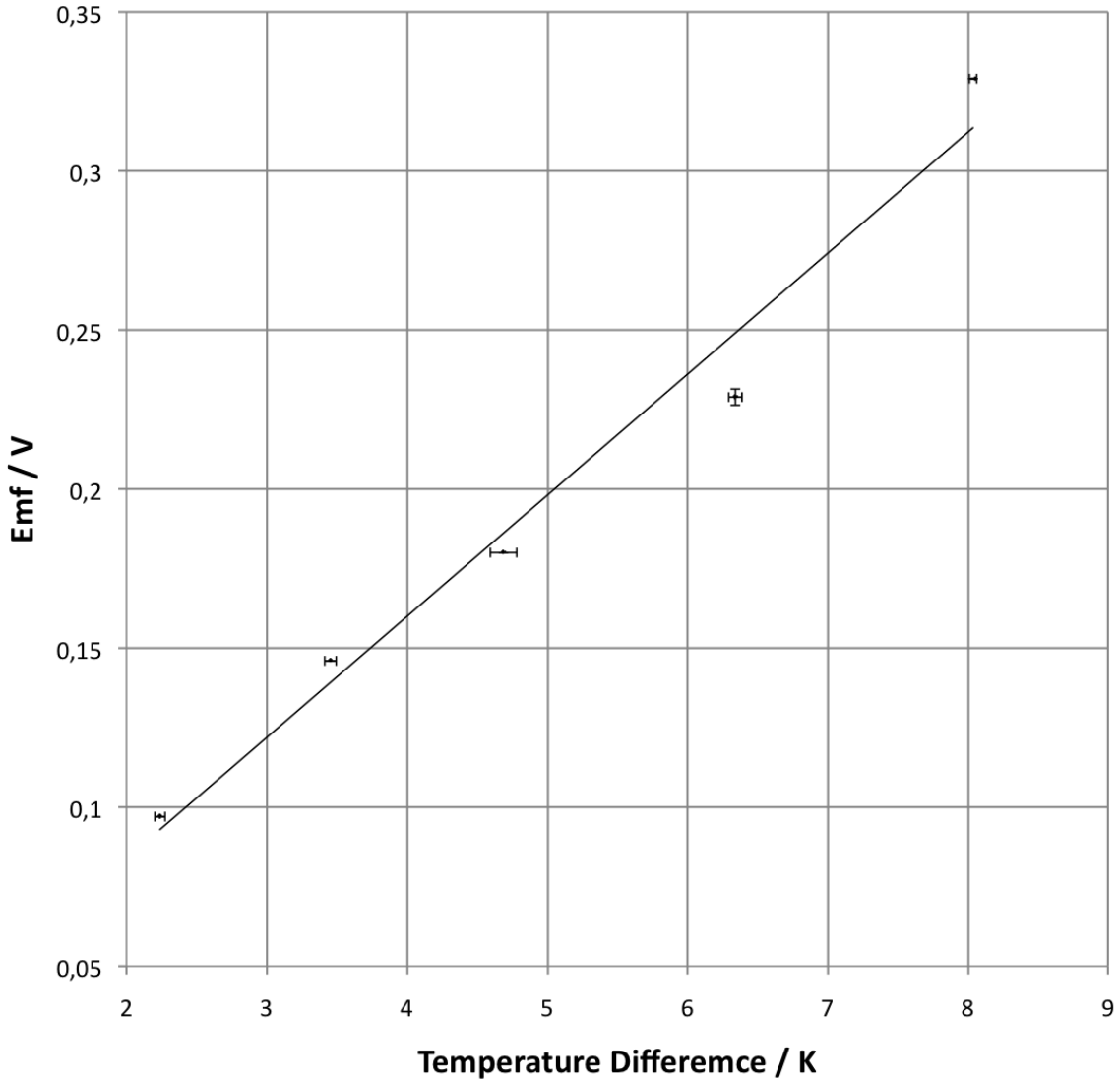

Figure 3.5: The measured emf of the thermoelectric module, plotted as a function of the temperature difference across the thermoelectric module, $\Delta \mathrm{T} = \mathrm{T_h} - \mathrm{T_c}$, with 95 % confidence error bars.

.

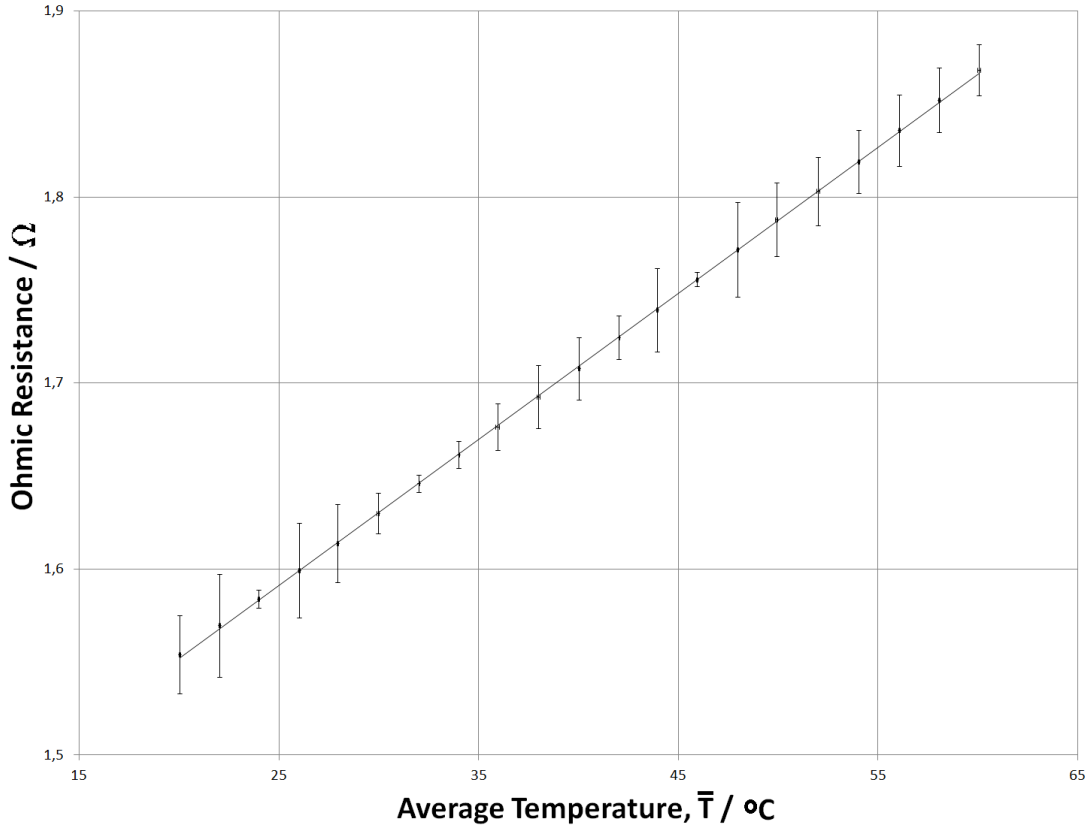

Figure 3.6: The measured ohmic resistance, R, plotted as a function of average temperature across the thermoelectric module, $\overline{\mathrm{T}} = \frac{\mathrm{T_h} + \mathrm{T_c}}{2}$, with 95 % confidence error bars.

.

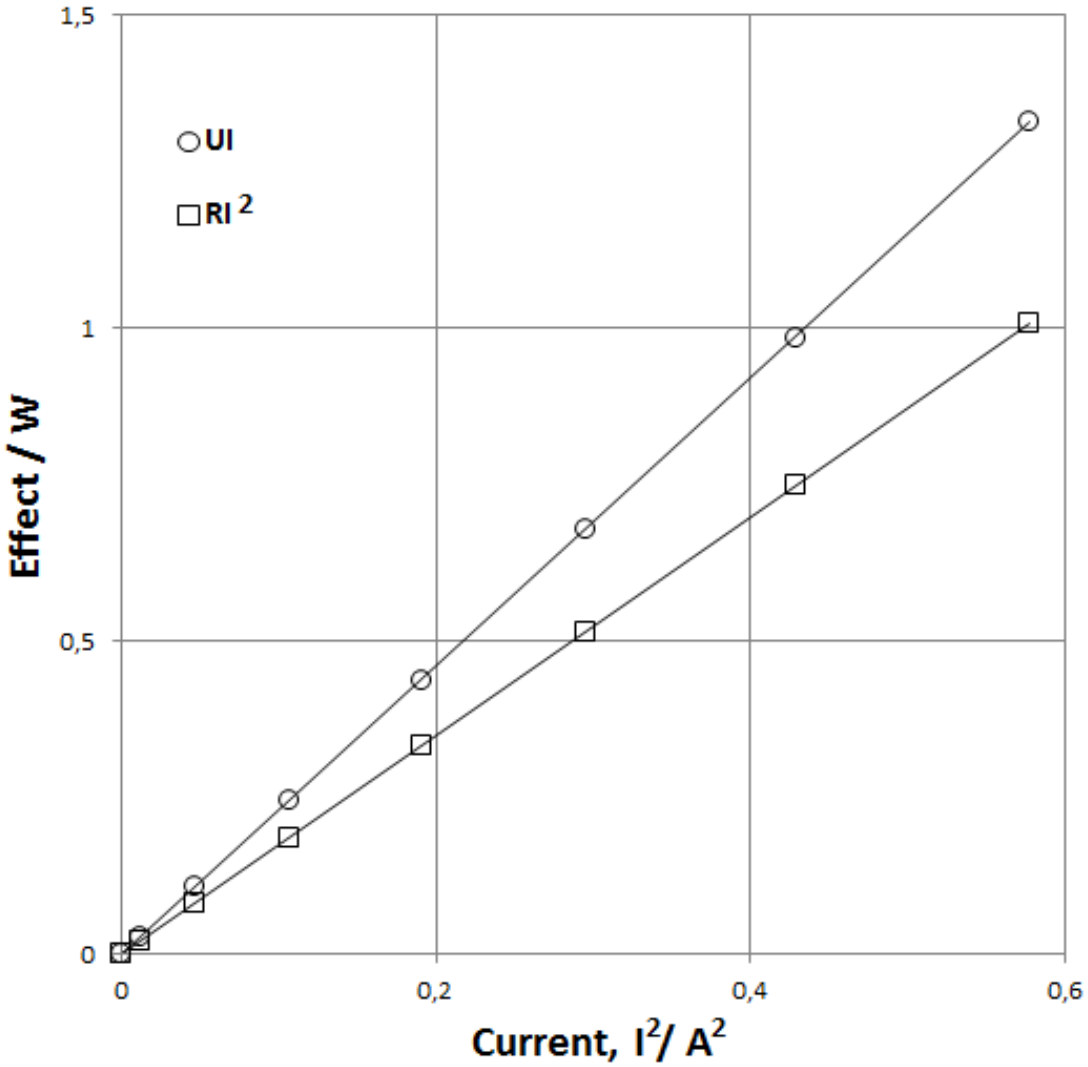

Figure 3.7: The measured ohmic resistance, R, plotted as a function of average temperature across the thermoelectric module, $\overline{\mathrm{T}} = \frac{\mathrm{T_h} + \mathrm{T_c}}{2}$, with 95 % confidence error bars.

.

3.4 Conclusion

Using a calorimeter the Seebeck coefficient of the module was determined to be $\eta_{S,module} = 37 \pm 7\,\mathrm{mVK}^{-1}$. This is in accordance with the prevoiusly reported values by Takla [2].

The isothermal ohmic resistance was determined to follow a linear temperature dependency descibed by $R = 1.394 + 0.007\,\overline{T}$. This is also in agreement with previously reported values by Takla [2].

The biggest challenge with the given apparatus, was to precisely determine the heat fluxes into and out of the Peltier element, which limited the accuracy of measuring the entropy production, and heat polarization of the Peltier element.

Chapter 4

Answer to the problem formulation

4.1 Problem Formulation

The overall goal of the project is to measure the heat and work produced by two thermoelectric devices. The project starts with a review of calorimetric studies of thermoelectric and other devices relevant for renewable energy conversion and storage. Calorimetric measurements shall be done for a stack of supercapacitors and a thermoelectric generator from semiconductors. As thermoelectric generator the Bi-Te module from Thermo-Gen AB will be investigated. Regarding the supercapacitors, commercial ones (PC10-series) supplied from Maxwell, Germany, will be used.

The aim is to study the efficiency of the conversion of thermal energy into electric energy, expressed in terms of the entropy production. The efficiency shall also be calculated from the figure of merit of the converter. The experimental program shall examine the module under various external loads and temperature conditions (temperature difference across the module, and absolute temperatures at the boundaries). The calorimeter designed by Burheim [3] for studies of fuel cells, shall be used. The positioning of the module in the calorimeter may have to be optimized. The work shall aim to obtain results as described by Marit Takla in her master thesis [2], but with higher precision, and with error estimates. The experimental results shall be described using irreversible thermodynamics theory, as presented in the book by Kjelstrup et al. [4].

For the super capacitors, the effective thermal conductivity is to be obtained in a reproducible manner, along with the measured and calculated entropy production. This project is a continuation of a small student project initiated by Hauge the student et al. [1]. It is also an expansion of an introductionary study of thermal conductivities of super capacitor electrodes – a field of high novelty with commercial

interests [36]. It is a goal that the student should first reproduce results of his first project for a stack of super capacitor commercial devices, and that these results come to a level where it is acceptable for journal publication.

4.2 Response

Throughout this thesis all problems have been answered, with the exception of determining the figure of merit, Z, and recording the internal heat polarization of the Peltier element in Seebeck mode. We also had problems determing the measured heat for the Peltier mode. All these problems stem from the low resolution of measuring the heat. Suggestions for improving this in a future study is given in section (3.3.3).

Bibliography

[1] Hans Henrik Hauge. *TKJ4510 Project: Isothermal Calorimetry of Supercapacitors*. NTNU, 2013.

[2] Marit Takla. Recovering industrial waste heat by the means of thermoelectricity. *Master Thesis at NTNU*, 2010.

[3] Odne Stokke Burheim. *Thermal Signature and Thermal Conductivities of PEM Fuel Cells*. Doctoral Thesis at NTNU, 2009.

[4] Johannessen E. Kjelstrup S., Bedeaux D. and Gross J. *Non-Equilibrium Thermodynamics for Engineers*. World Scientific Publishing Co. Pte. Ltd., 2010.

[5] Sankara Papavinasam. Chapter 1 - the oil and gas industry. In Sankara Papavinasam, editor, *Corrosion Control in the Oil and Gas Industry*, pages 1 – 39. Gulf Professional Publishing, Boston, 2014.

[6] Thomas Christen and Martin W. Carlen. Theory of the ragone plots. *Journal of Power Sources*, 91:210 – 216, 2000.

[7] Working Group I of the IPCC. Working group i contribution to the ipcc fifth assessment report climate change 2013: The physical basis. *http://www.ipcc.ch*, 2013.

[8] Taagepera Rein. A world population growth model: Interaction with earth's carrying capacity and technology in limited space. page http://www.mpoweruk.com/performance.htm, 2013.

[9] Tom Knapp and Rajen Mookerjee. Population growth and global {CO2} emissions: A secular perspective. *Energy Policy*, 24(1):31 – 37, 1996.

[10] Tucker M. Carbon dioxide emissions and global gdp. *Ecological Economics*, 15:215–223, 1995.

[11] DeJoseph B.M. Branch T.A. and Ray L.J. Impacts of ocean acidification on marine seafood. *Trends in Ecology and Evolution*, 28:178–186, 2013.

[12] Ferenc L. Toth and Hans-Holger Rogner. Oil and nuclear power: Past, present, and future. *Energy Economics*, 28(1):1 – 25, 2006.

[13] Scott Hardman, Robert Steinberger-Wilckens, and Dan van der Horst. Disruptive innovations: The case for hydrogen fuel cells and battery electric vehicles. *International Journal of Hydrogen Energy*, 38(35):15438 – 15451, 2013.

[14] G. Pasaoglu, D. Fiorello, A. Martino, L. Zani, A. Zubaryeva, and C. Thiel. Travel patterns and the potential use of electric cars results from a direct survey in six european countries. *Technological Forecasting and Social Change*, (0):–, 2013.

[15] Marius Lorentzen. Her er de mest solgte bilene i 2013: Tesla ble førjulsfavoritten. *http://www.e24.no*, (Retrieved January 13th 2014).

[16] http://www.maxwell.com/products/ultracapacitors/industries/regenerative power. Maxwell ultracapacitor regenerative power solutions. (Retrieved January 8th 2014).

[17] Slideshare.net. Super capacitor buses in shanghai. 2010 (Retrieved January 6th 2014).

[18] Tyler Hamilton. Next stop: Ultracapacitor buses. *Technology Review, MIT*, 2009 (Retrieved January 6th 2014).

[19] W.G. Pell and B.E. Conway. Quantitative modeling of factors determining ragone plots for batteries and electrochemical capacitors. *Journal of Power Sources*, 63(2):255 – 266, 1996.

[20] http://www.maxwell.com/ultracapacitors/. Maxwell ultracapacitors: Enabling energy's future. (Retrieved January 8th 2014).

[21] http://spectrum.ieee.org/green-tech/advanced-cars/the-charge-of-the-ultra capacitors. The charge of the ultra - capacitors: Nanotechnology takes energy storage beyond batteries. 2007 (Retrieved January 8th 2014).

[22] Signe Kjelstrup and Dick Bedeaux. *Non-Equilibrium Thermodynamics of Heterogeneous Systems*. World Scientific Publishing Co. Pte. Ltd., 2008.

[23] http://www.hydro.com. Aluminium, environment and society. (Retrieved January 11th 2014).

[24] Alton T. Tabereaux and Ray D. Peterson. Chapter 2.5 - aluminum production. In Seshadri Seetharaman, editor, *Treatise on Process Metallurgy*, pages 839 – 917. Elsevier, Boston, 2014.

[25] Cheng-Ting Hsu, Gia-Yeh Huang, Hsu-Shen Chu, Ben Yu, and Da-Jeng Yao. Experiments and simulations on low-temperature waste heat harvesting system by thermoelectric power generators. *Applied Energy*, 88(4):1291 – 1297, 2011.

[26] M.A. Karri, E.F. Thacher, and B.T. Helenbrook. Exhaust energy conversion by thermoelectric generator: Two case studies. *Energy Conversion and Management*, 52(3):1596 – 1611, 2011.

[27] Y.Y. Hsiao, W.C. Chang, and S.L. Chen. A mathematic model of thermoelectric module with applications on waste heat recovery from automobile engine. *Energy*, 35(3):1447 – 1454, 2010.

[28] K. Matsubara. Development of a high efficient thermoelectric stack for a waste exhaust heat recovery. *Proceedings of ICTÕ02, 21st International Conference on thermoelectrics*, pages 418–423, 2002.

[29] D. Astrain, J.G. ViÃ¡n, and J. Albizua. Computational model for refrigerators based on peltier effect application. *Applied Thermal Engineering*, 25(17â18):3149 – 3162, 2005.

[30] Inagaki M. Konno H. and Tanaike O. Carbon materials for electrochemical capacitors. *Journal of Power Sources*, 195:7880 7903, 2010.

[31] P.A. Tipler and G. Mosca. *Physics for Scientists and Engineers*. W.H. Freeman and Company, 6th edition, 2008.

[32] H.O. Ohanian. *Principles of Physics*. W.W. Norton and Company Inc., 6th edition, 1994.

[33] W.E. Stewart Bird R.B. and E.N. Lightfoot. *Transport Phenomena*. John Wiley and Sons, 2nd edition, 2007.

[34] O.S. Burheim, G. Ellila, J.D. Fairweather, A. Labouriau, S. Kjelstrup, and J.G. Pharoah. Ageing and thermal conductivity of porous transport layers used for {PEM} fuel cells. *Journal of Power Sources*, 221(0):356 – 365, 2013.

[35] Odne S. Burheim, Huaneng Su, Sivakumar Pasupathi, Jon G. Pharoah, and Bruno G. Pollet. Thermal conductivity and temperature profiles of the micro porous layers used for the polymer electrolyte membrane fuel cell. *International Journal of Hydrogen Energy*, 38(20):8437 – 8447, 2013.

[36] Odne S. Burheim, Mesut Aslan, Jennifer S. Atchison, and Volker Presser. Thermal conductivity and temperature profiles in carbon electrodes for supercapacitors. *Journal of Power Sources*, 246(0):160 – 166, 2014.

[37] Maxwell Technologies. Datasheet: Pc-series ultracapacitors. *"http://www.maxwell.com/"*, 2013.

[38] O. Burheim, P.J.S. Vie, J.G. Pharoah, and S. Kjelstrup. Ex situ measurements of through-plane thermal conductivities in a polymer electrolyte fuel cell. *Journal of Power Sources*, 195(1):249 – 256, 2010.

[39] Dick Bedeaux Fernando Bresme, Anders Lervik and Signe Kjelstrup. Water polarization under thermal gradients. *Physical Review Letters*, 101, 208.

[40] California Institute of Technology. Brief history of thermoelectrics. *http://www.thermoelectrics.caltech.edu/thermoelectrics/history.html*, (Retrieved January 20th 2014).

[41] Jim Williams. 30 - thermocouple measurement. In Bob Dobkin and Jim Williams, editors, *Analog Circuit Design*, pages 596 – 613. Newnes, Oxford, 2011.

[42] S.B Riffat and Xiaoli Ma. Thermoelectrics: a review of present and potential applications. *Applied Thermal Engineering*, 23(8):913 – 935, 2003.

[43] Mason Jiang. An overview of radioisotope thermoelectric generators. *http://www.large.stanford.edu*, 2013.

[44] D.M. Rowe. Thermoelectrics, an environmentally-friendly source of electrical power. *Renewable Energy*, 16(1â4):1251 – 1256, 1999. Renewable Energy Energy Efficiency, Policy and the Environment.

[45] Gao Min and D.M. Rowe. Cooling performance of integrated thermoelectric microcooler. *Solid-State Electronics*, 43(5):923 – 929, 1999.

[46] M.S. Dresselhaus-Z.F. Ren M. Zebarjadi, K. Esfarjani and G. Chen. Perspectives on thermoelectrics: from fundamentals to device applications. *Energy and Environmetal Sciece*, 5(1â4):5147 – 5162, 2012.

[47] A. Bejan. Entropy generation minimization. the method of thermodynamic optimization of finite-soze systems and finite-time processes. *CRC Press*, 1996.

[48] Kjelstrup S. and Ramstad A.L. *Prosjekter i fysikalsk kjemi grunnkurs*. Tapir Akademiske Forlag, 5th edition, 2007.

[49] O.S. Burheim. Error analysis for measured values.

Appendix A

Calculation of Experimental Uncertainty

The error propagation is based on standard statistical methods described by Kjelstrup and Ramstad [48], and Burheim [49]. For a variable, denoted by y, the mean value of a series of measurements, $\overline{y}$, is given by equation (A.1)

$$\overline{y} = \frac{1}{n}\sum_{i=1}^{n} y_i \tag{A.1}$$

where the subscript i indicate the number of measurments of the parameter y. The unbiased variance, s^2, is given by equation (A.2):

$$s^2(y) = \frac{\sum_{i=1}^{n}(y_i - \overline{y})^2}{n-1} \tag{A.2}$$

The the standard deviation of the of the parameter is obtained by taking the square root of the variance achieved in equation (A.2), giving the expresion in equation (A.3):

$$s(y) = \sqrt{s^2(y)} \tag{A.3}$$

For measurments of e.g. ditances, the measuring devices are often provided with a measurement error, u. In these cases the combined standard deviation is given by equation (A.4):

$$s_c = \sqrt{s^2(y) + u^2(y)} \tag{A.4}$$

where $u(y)$ indicate the error related to the reading of the value. Provided that the data measured has normal distribution, it is standard procedure to present the experimental values with a 95% confidence interval, corresponding to the double standard deviation of the mean value described in equation (A.5)

$$y = \overline{y} \pm 2s(y) \tag{A.5}$$

For a parameter, y that is derived from other parameters an error propagation calculation has to be performed. The parameter y can be expressed as a function of the parameters $x_1, x_2, ..., x_m$ that defines it, $y = f(x_1, x_2, ..., x_m)$, for which the standard deviation is known. The standard deviation of the variable y, can in this case be expressed by equation (A.6):

$$s(y) = \sqrt{s^2(y)} \approx \sqrt{\sum_{i=1}^{m} \left(\frac{\partial f}{\partial x_i}\right)^2 s^2(x_i)} \tag{A.6}$$

where $\frac{\partial f}{\partial x_i}$ and $s^2(x_i)$ indicate the derivative of the function describing the parameter y with respect to the parameter x_i and the unbiased variance of the variable x_i, respectively.

Appendix B

Experimental Basis Data

B.1 Supercapacitor Experiments

B.1.1 Thermal Conductivity of the Supercapacitor Components

In the following figures (B.1) through (B.25) the thermal resistance, $\mathrm{r_i}$, and the corresponding thicknesses, δ_i of the supercapacitor materials with axial and vertical $95\,\%$ confidence error bars, measured in the experiments described in the section (2.2.3). The data are presented for four material thicknesses for the aluminium current collectors, the electrodes, the plastic coating, the separator, and for three material thicknesses for the steel housing (due to lack of material samples), at compaction pressures of $4.6\,\mathrm{bar}$, $9.2\,\mathrm{bar}$, $13.8\,\mathrm{bar}$ and $16.1\,\mathrm{bar}$ during compression, and $4.6\,\mathrm{bar}$ during decompression. The results presented in this section is the basis for the resulting thermal conductivities, λ, presented in section (**??**, described theoretically in section (**??**.

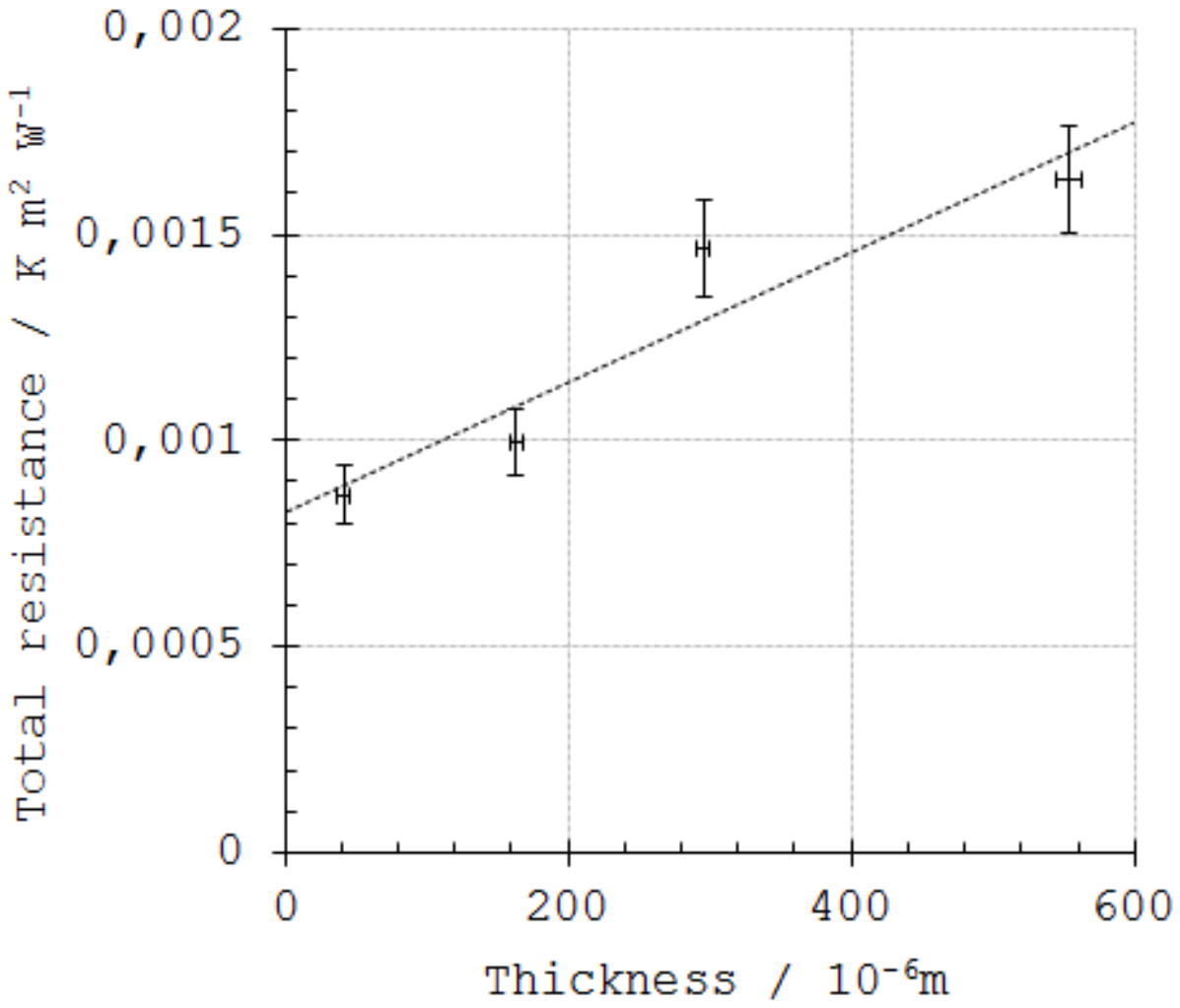

Figure B.1: Plot of the total thermal resistance of four material thicknesses of the aluminium current collectors of the Maxwell PC-10 series supercapacitors, $\mathrm{r_{Al}}$, as a function of the sample thickness, δ_{Al}, at $4.6\,\mathrm{bar}$ compression pressure, with axial and vertical 95% confidence error bars, and linear trendline.

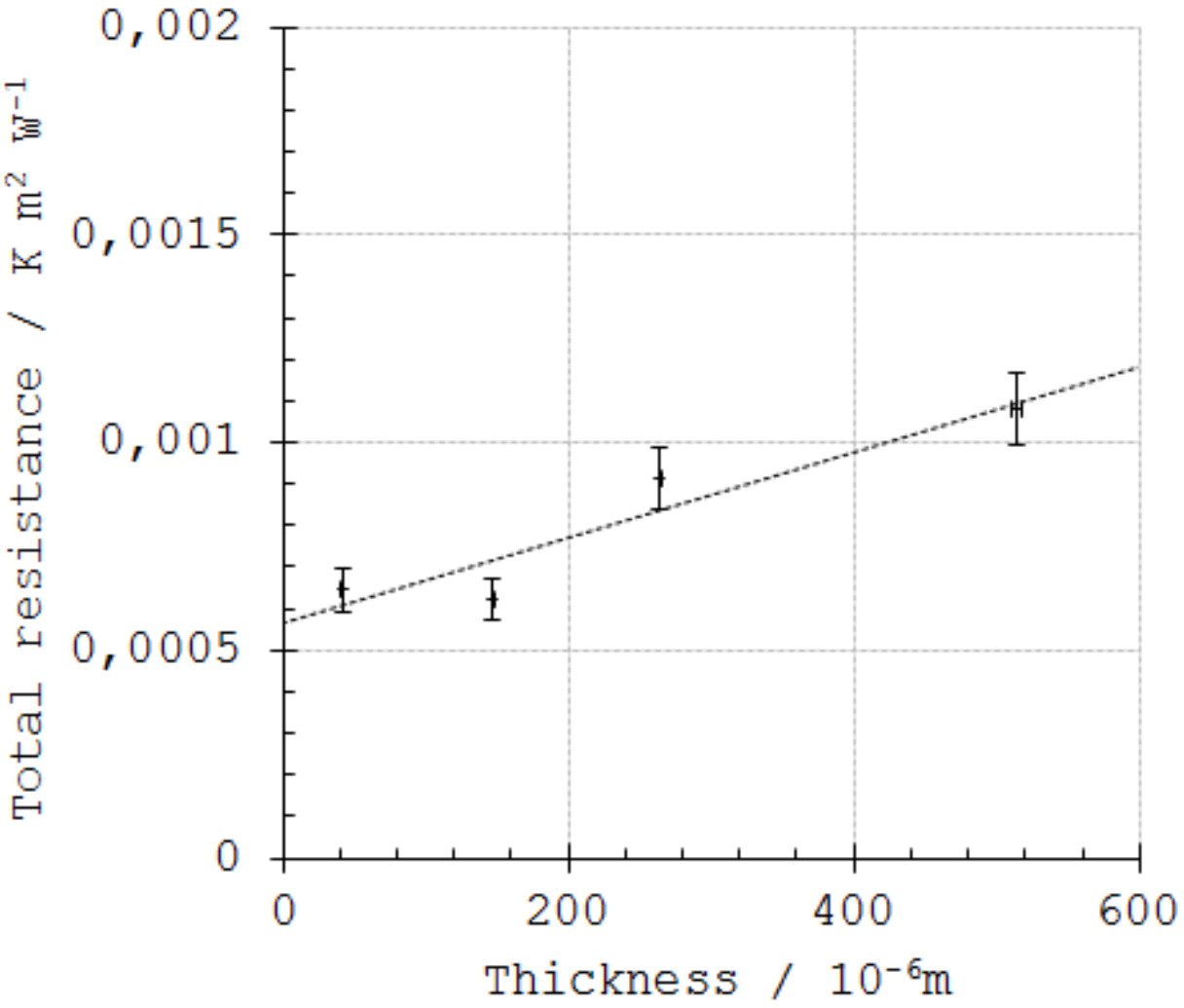

Figure B.2: Plot of the total thermal resistance of four material thicknesses of the aluminium current collectors of the Maxwell PC-10 series supercapacitors, $\mathrm{r_{Al}}$, as a function of the sample thickness, δ_{Al}, at $9.2\,\mathrm{bar}$ compression pressure, with axial and vertical 95% confidence error bars, and linear trendline.

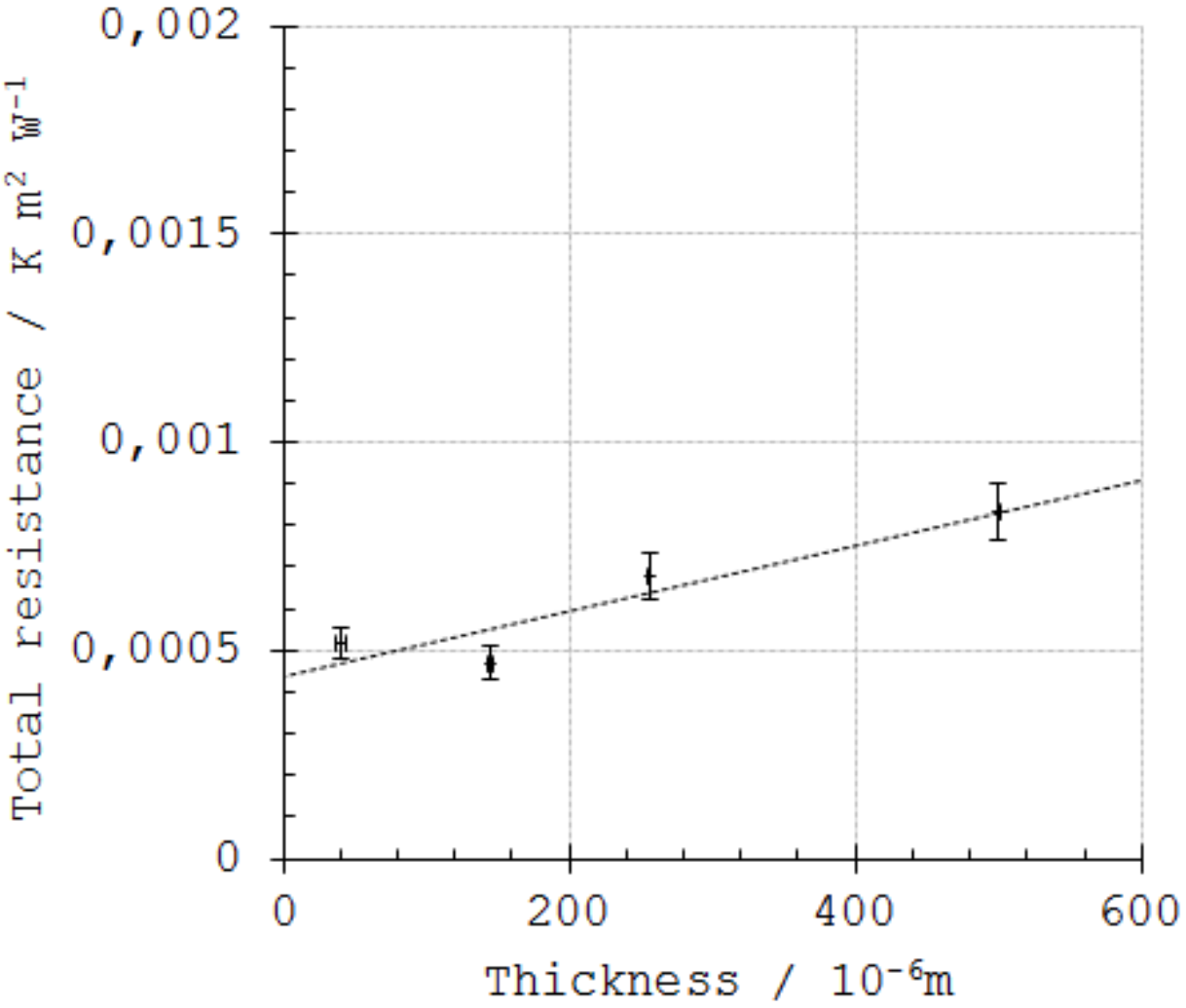

Figure B.3: Plot of the total thermal resistance of four material thicknesses of the aluminium current collectors of the Maxwell PC-10 series supercapacitors, $\mathrm{r_{Al}}$, as a function of the sample thickness, δ_{Al}, at $13.8\,\mathrm{bar}$ compression pressure, with axial and vertical 95% confidence error bars, and linear trendline.

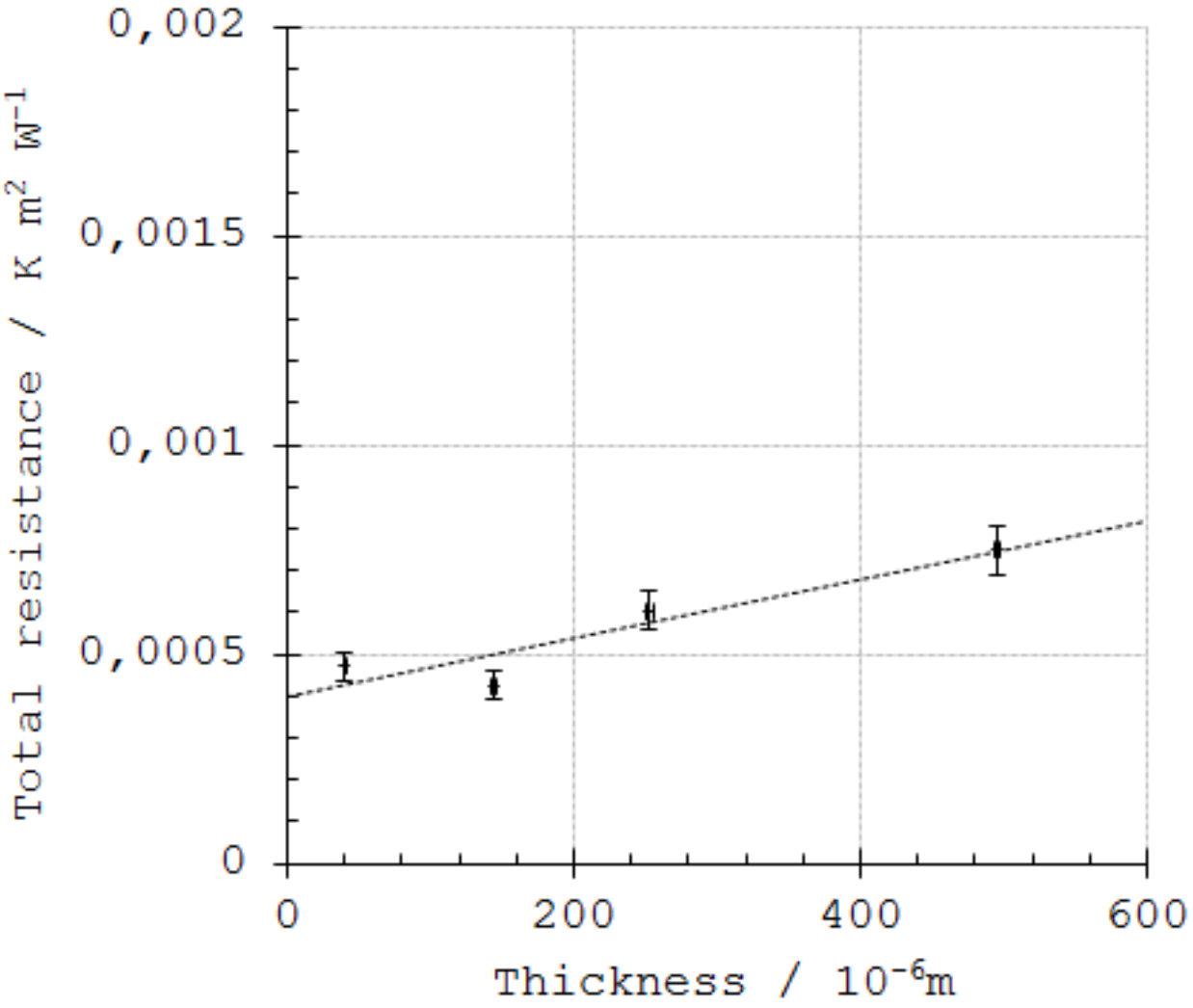

Figure B.4: Plot of the total thermal resistance of four material thicknesses of the aluminium current collectors of the Maxwell PC-10 series supercapacitors, r_{Al}, as a function of the sample thickness, δ_{Al}, at $16.1\,\mathrm{bar}$ compression pressure, with axial and vertical 95% confidence error bars, and linear trendline.

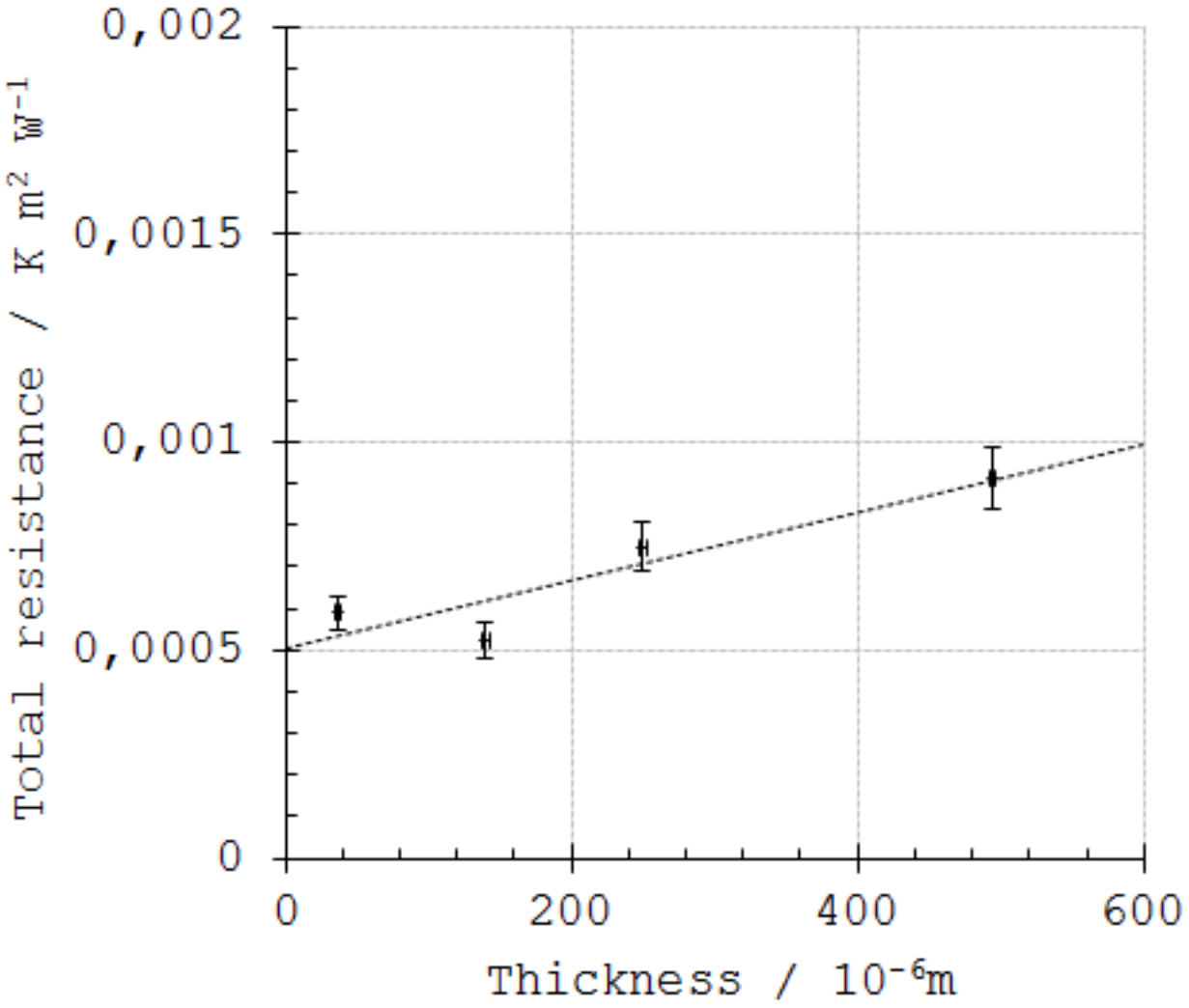

Figure B.5: Plot of the total thermal resistance of four material thicknesses of the aluminium current collectors of the Maxwell PC-10 series supercapacitors, $\mathrm{r_{Al}}$, as a function of the sample thickness, δ_{Al}, at $4.6\,\mathrm{bar}$ compression pressure (during decompression), with axial and vertical 95% confidence error bars, and linear trendline.

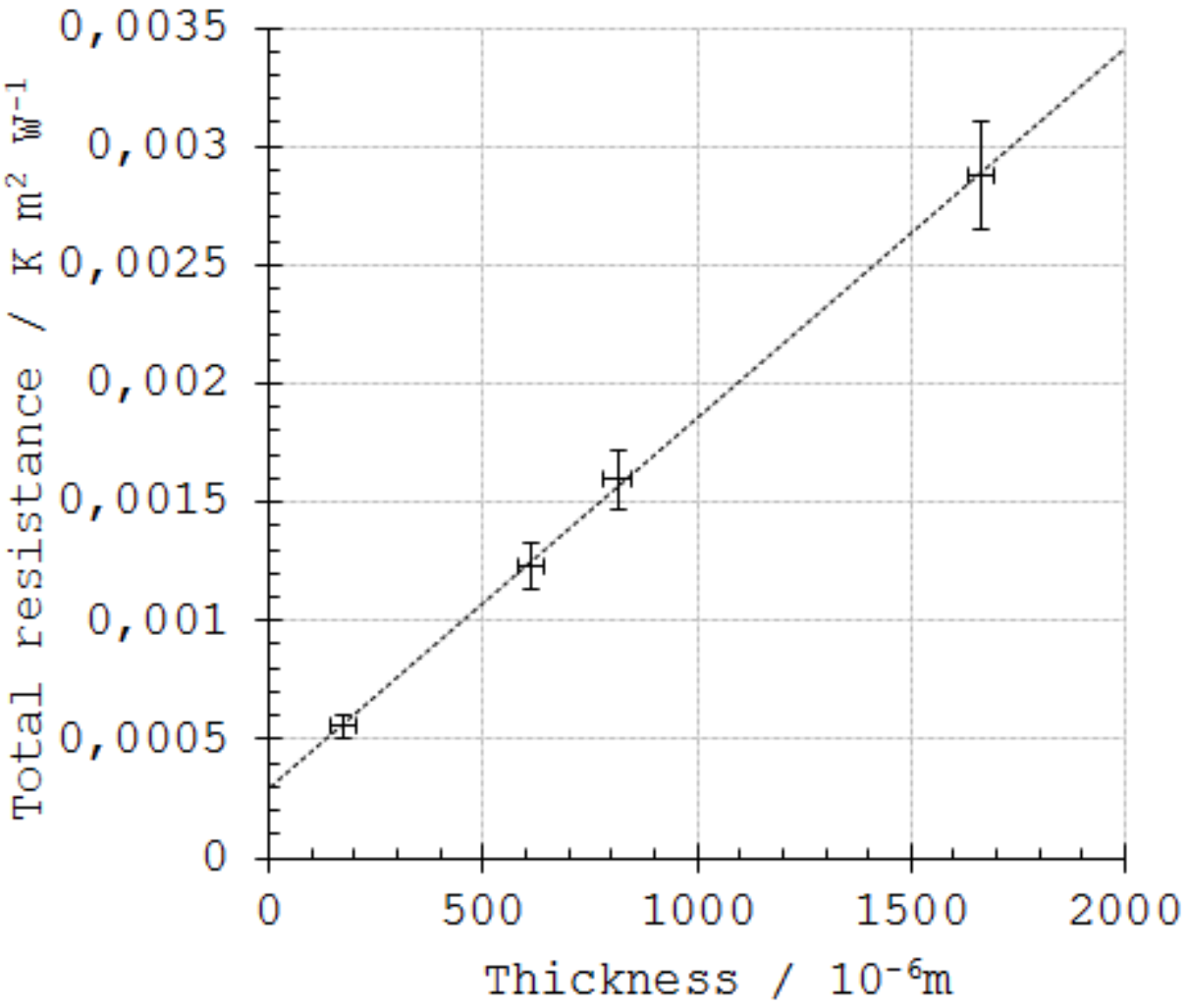

Figure B.6: Plot of the total thermal resistance of four material thicknesses of the activated carbon/aluminium electrodes of the Maxwell PC-10 series supercapacitors, $\mathrm{r_{el}}$, as a function of the sample thickness, δ_{el}, at $4.6\,\mathrm{bar}$ compression pressure, with axial and vertical 95% confidence error bars, and linear trendline.

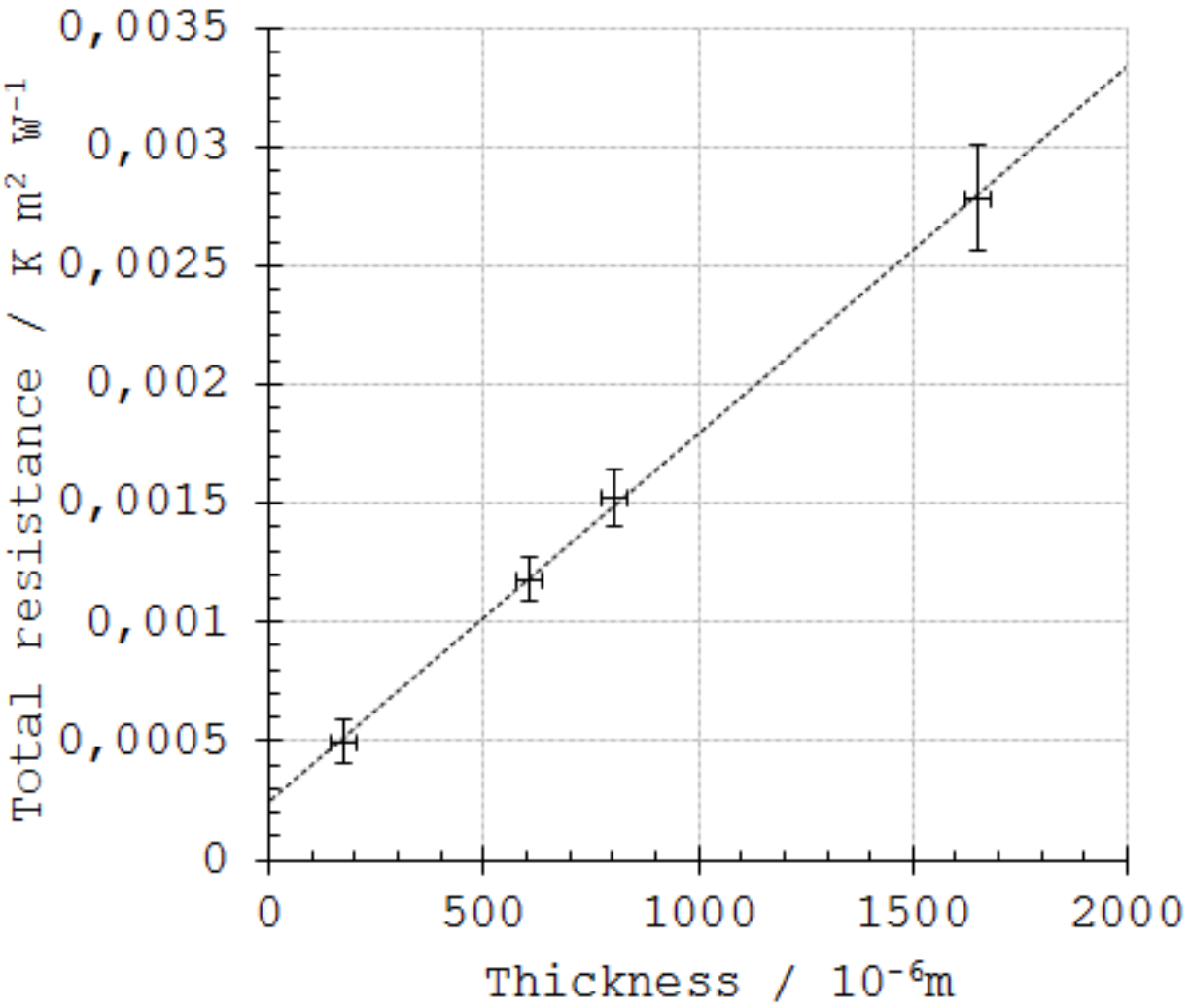

Figure B.7: Plot of the total thermal resistance of four material thicknesses of the activated carbon/aluminium electrodes of the Maxwell PC-10 series supercapacitors, $\mathrm{r_{el}}$, as a function of the sample thickness, δ_{el}, at $9.2\,\mathrm{bar}$ compression pressure, with axial and vertical 95% confidence error bars, and linear trendline.

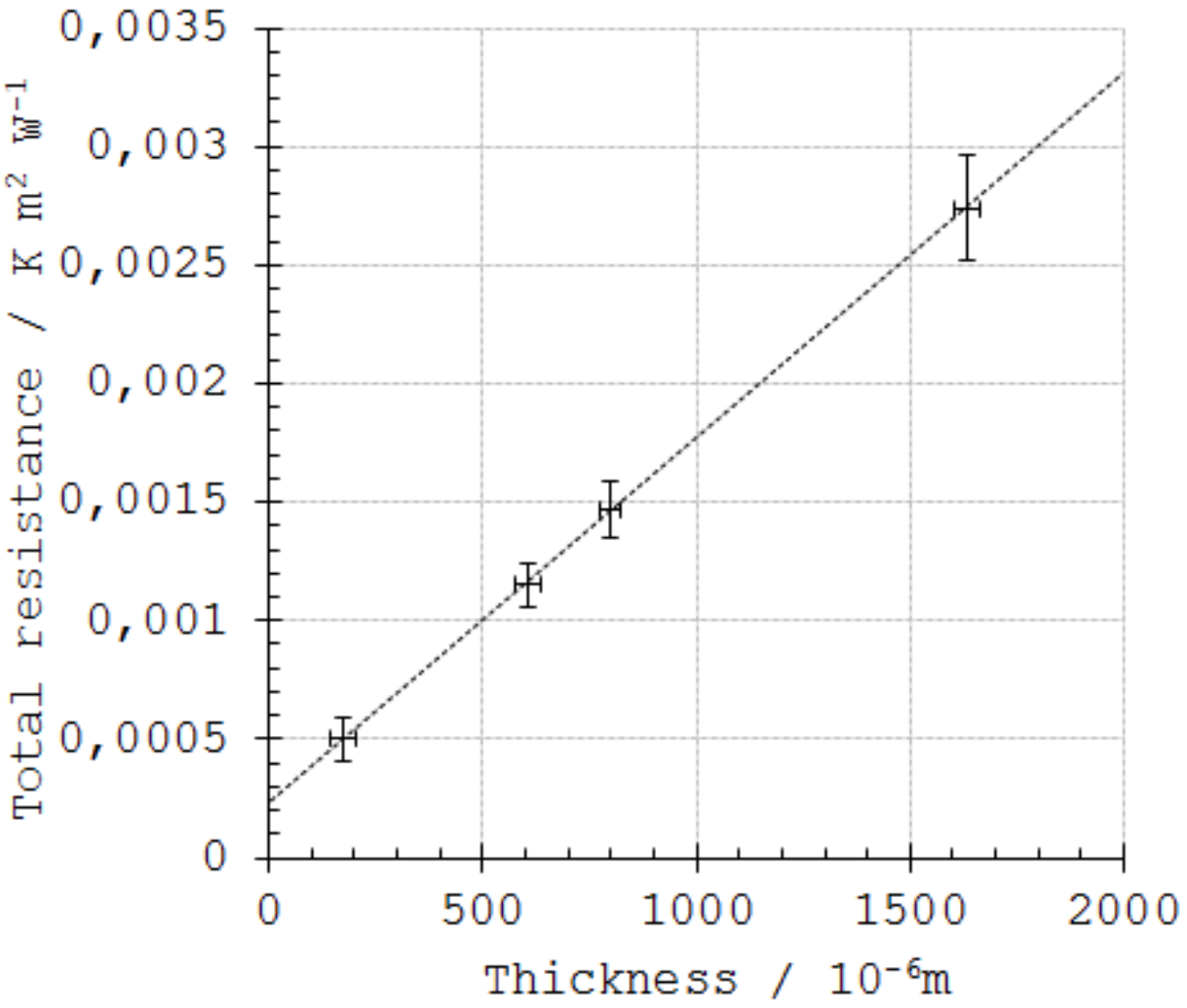

Figure B.8: Plot of the total thermal resistance of four material thicknesses of the activated carbon/aluminium electrodes of the Maxwell PC-10 series supercapacitors, $\mathrm{r_{el}}$, as a function of the sample thickness, δ_{el}, at $13.8\,\mathrm{bar}$ compression pressure, with axial and vertical 95% confidence error bars, and linear trendline.

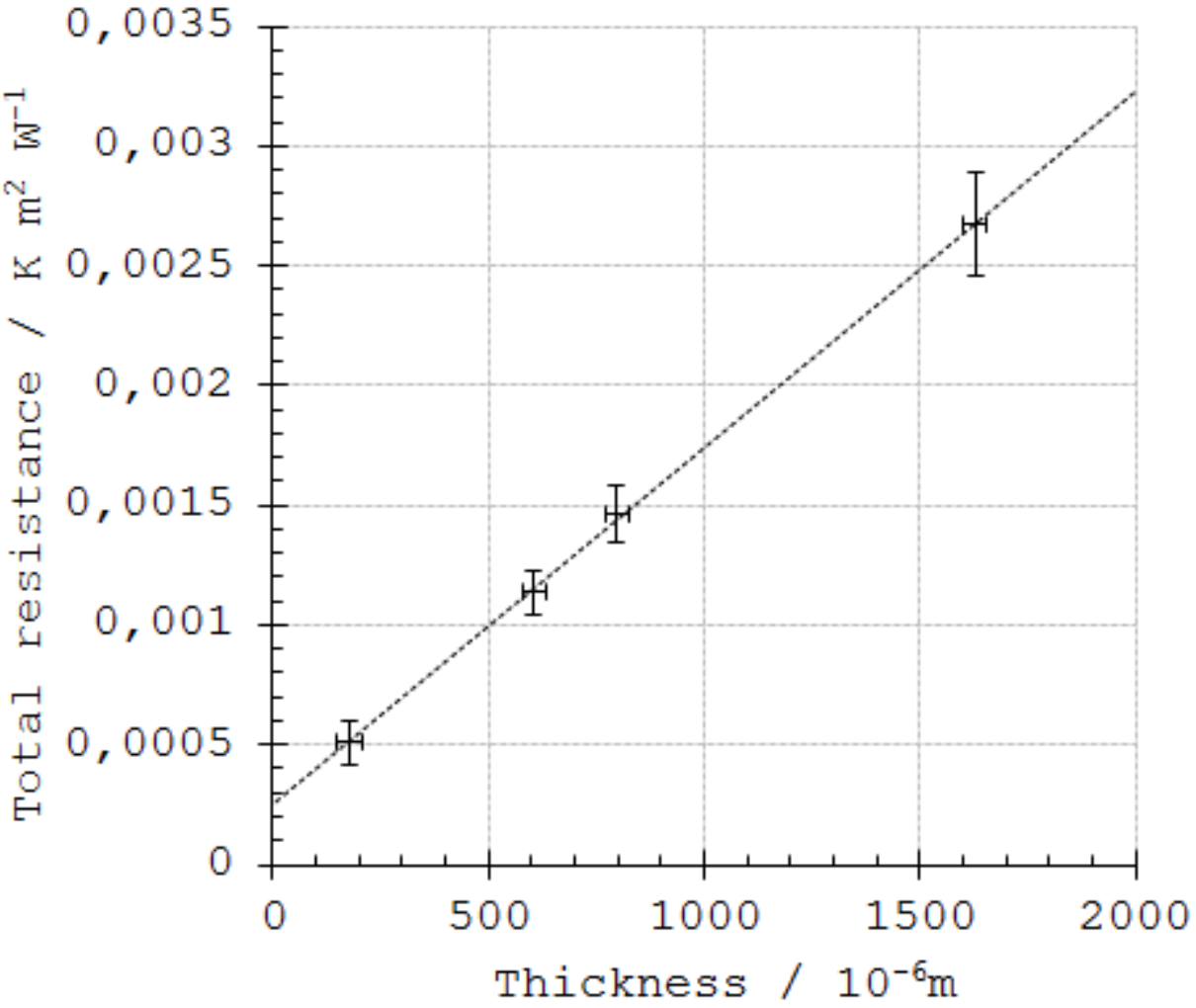

Figure B.9: Plot of the total thermal resistance of four material thicknesses of the activated carbon/aluminium electrodes of the Maxwell PC-10 series supercapacitors, $\mathrm{r_{el}}$, as a function of the sample thickness, δ_{el}, at $16.1\ \mathrm{bar}$ compression pressure, with axial and vertical 95% confidence error bars, and linear trendline.

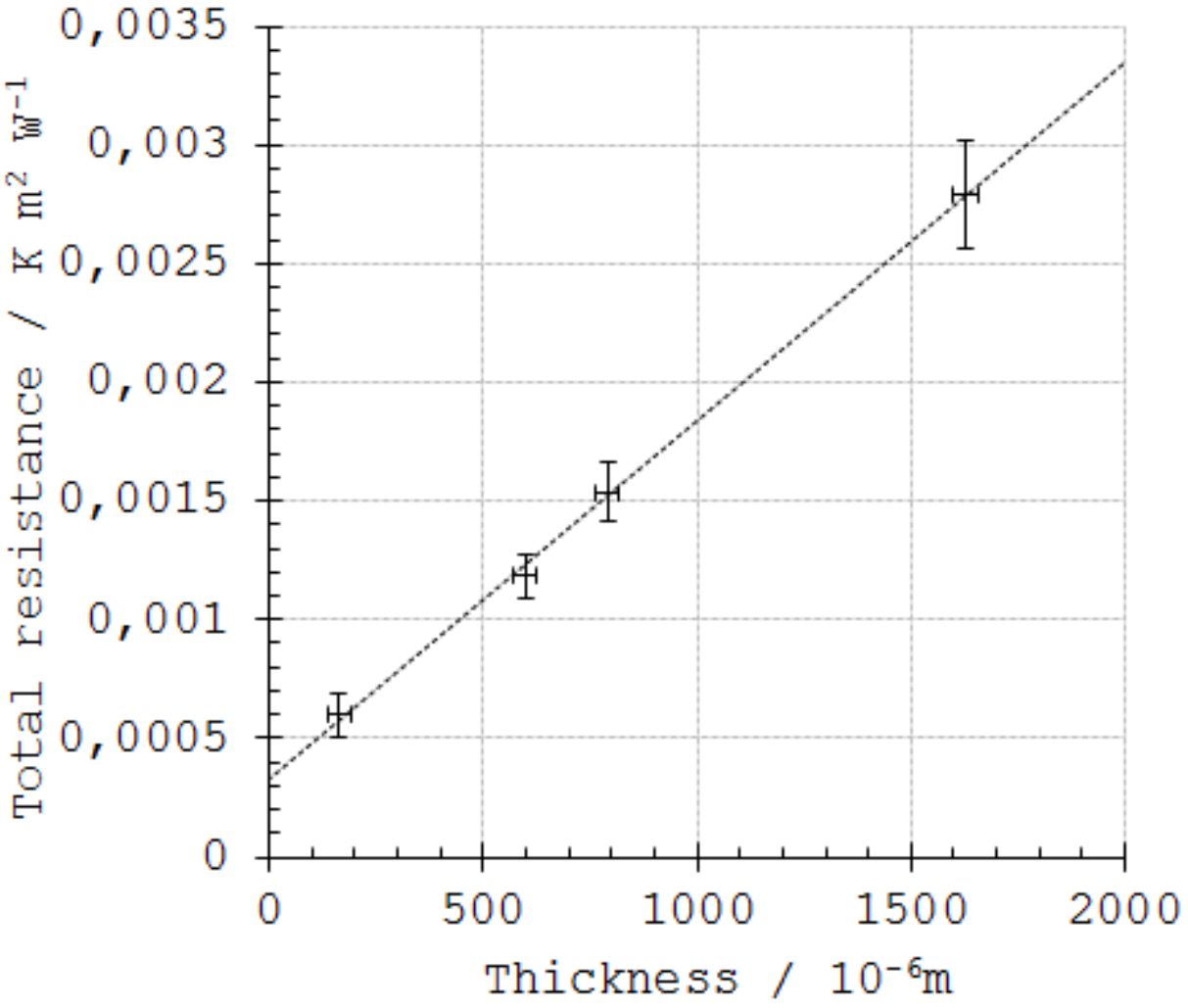

Figure B.10: Plot of the total thermal resistance of four material thicknesses of the activated carbon/aluminium electrodes of the Maxwell PC-10 series supercapacitors, $\mathrm{r_{el}}$, as a function of the sample thickness, δ_{el}, at $4.6\,\mathrm{bar}$ compression pressure (during decompression), with axial and vertical 95% confidence error bars, and linear trendline.

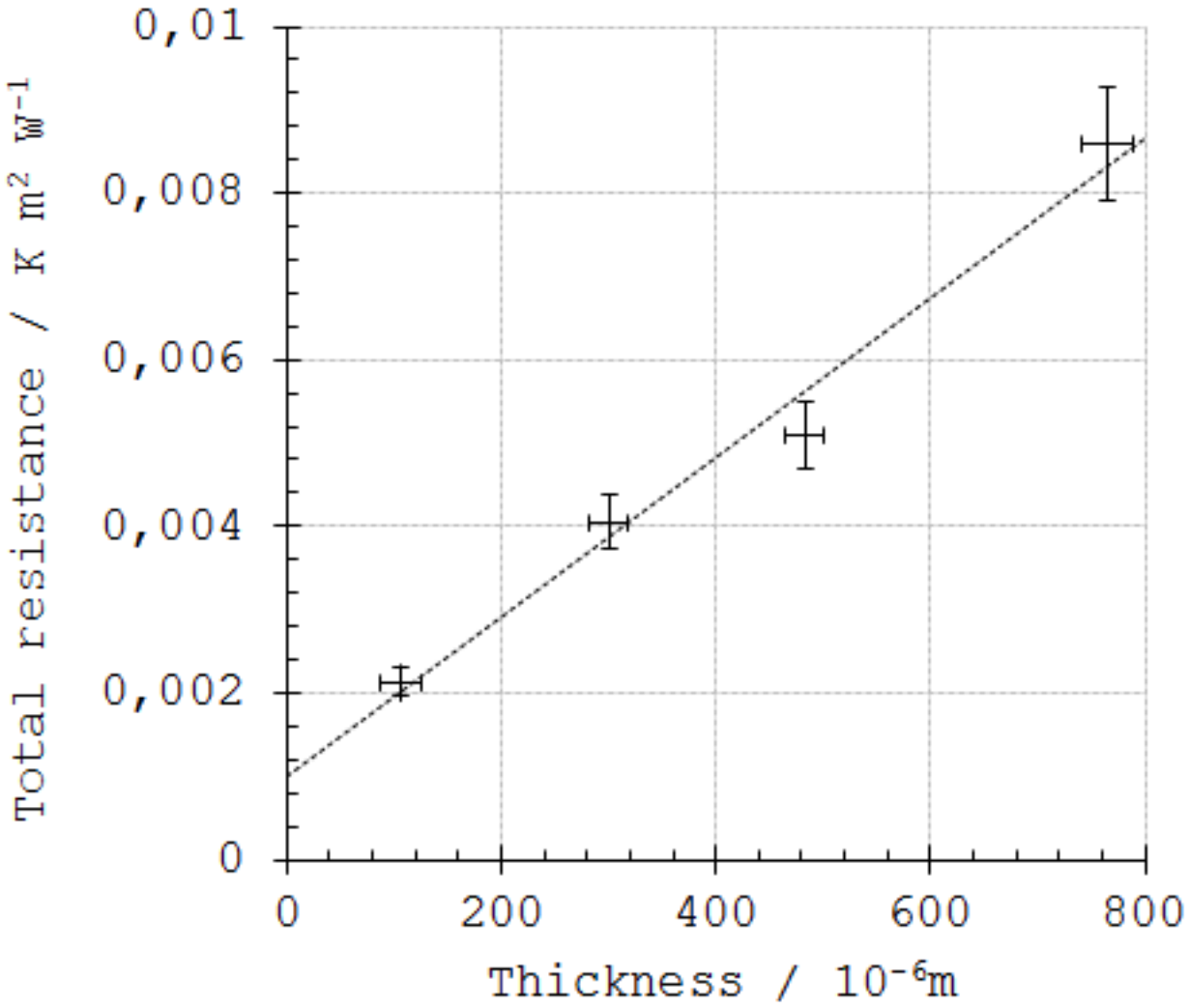

Figure B.11: Plot of the total thermal resistance of four material thicknesses of the plastic coating of the Maxwell PC-10 series supercapacitors, r_{pl}, as a function of the sample thickness, δ_{pl}, at $4.6\,\mathrm{bar}$ compression pressure, with axial and vertical 95% confidence error bars, and linear trendline.

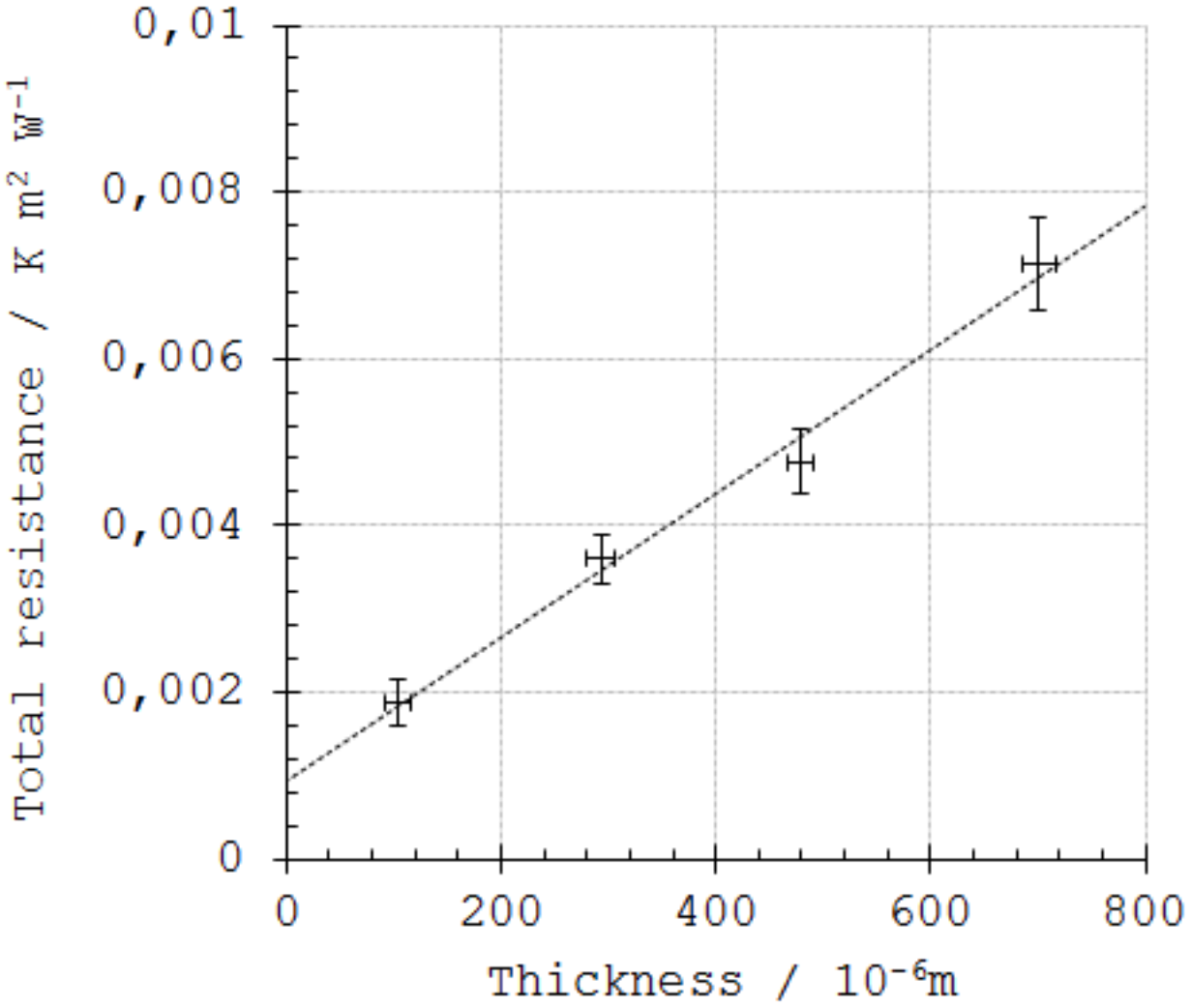

Figure B.12: Plot of the total thermal resistance of four material thicknesses of the plastic coating of the Maxwell PC-10 series supercapacitors, r_{pl}, as a function of the sample thickness, δ_{pl}, at $9.2\,\mathrm{bar}$ compression pressure, with axial and vertical 95% confidence error bars, and linear trendline.

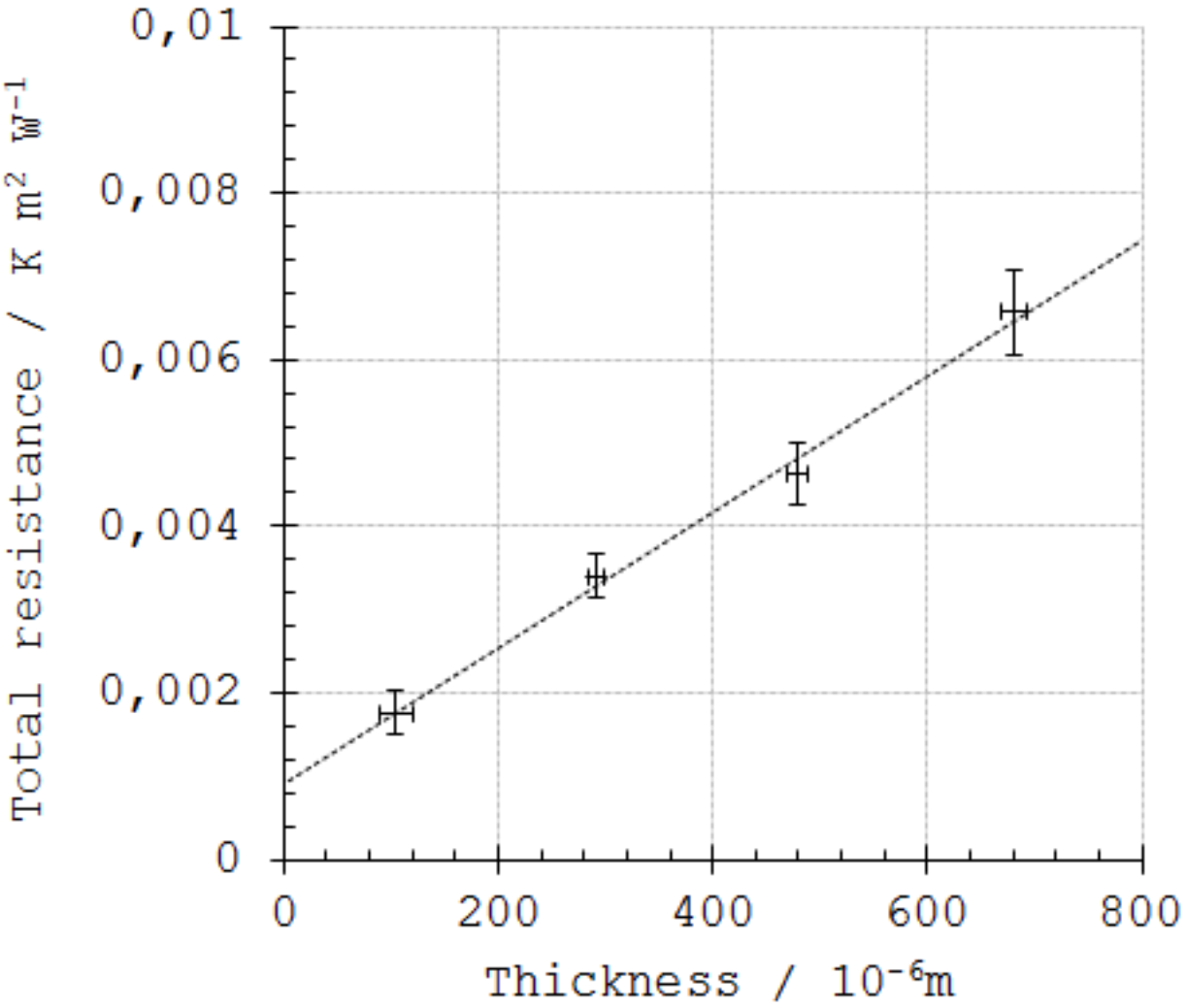

Figure B.13: Plot of the total thermal resistance of four material thicknesses of the plastic coating of the Maxwell PC-10 series supercapacitors, r_{pl}, as a function of the sample thickness, δ_{pl}, at $13.8\,\mathrm{bar}$ compression pressure, with axial and vertical 95% confidence error bars, and linear trendline.

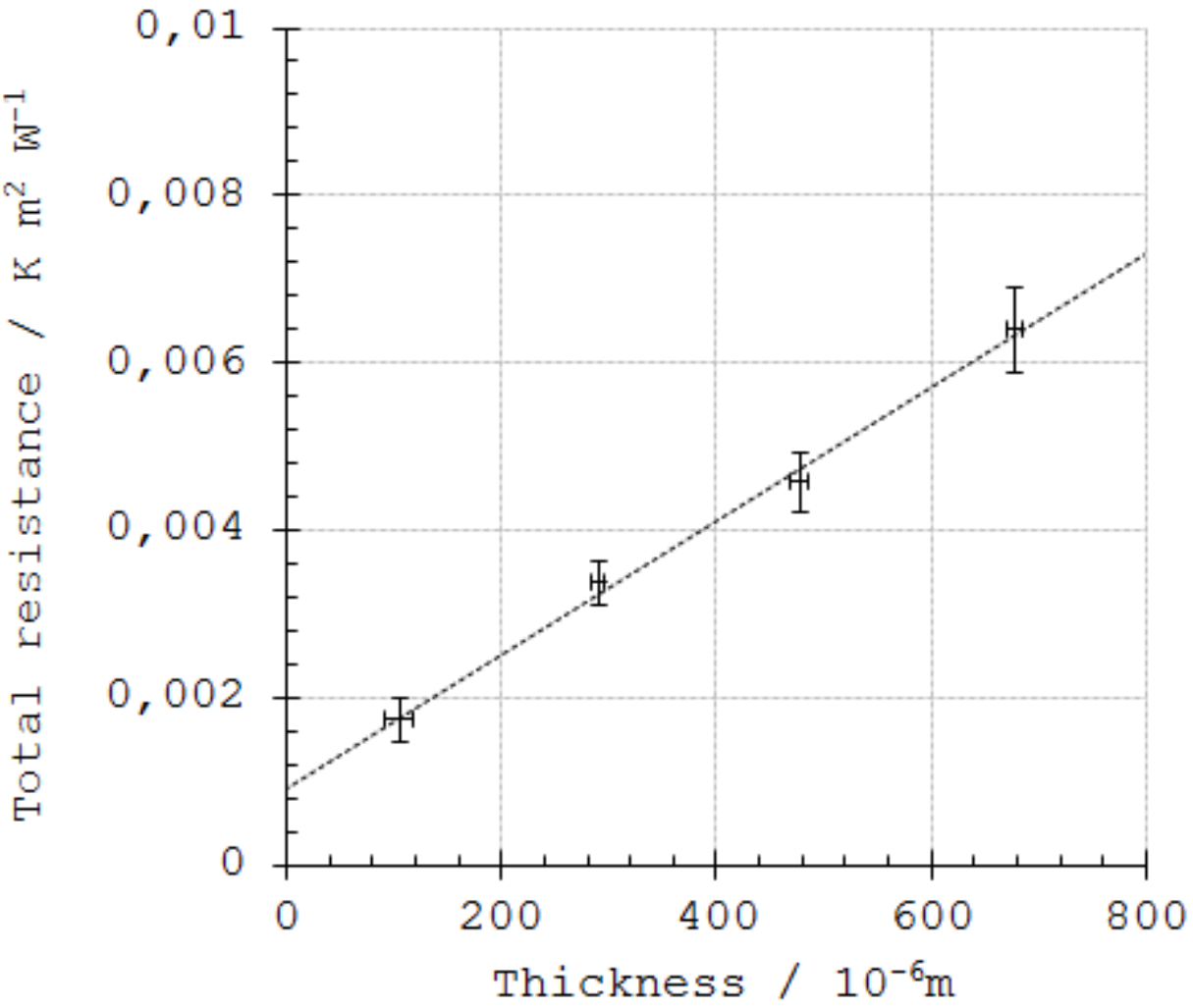

Figure B.14: Plot of the total thermal resistance of four material thicknesses of the plastic coating of the Maxwell PC-10 series supercapacitors, r_{pl}, as a function of the sample thickness, δ_{pl}, at $16.1\,\mathrm{bar}$ compression pressure, with axial and vertical 95% confidence error bars, and linear trendline.

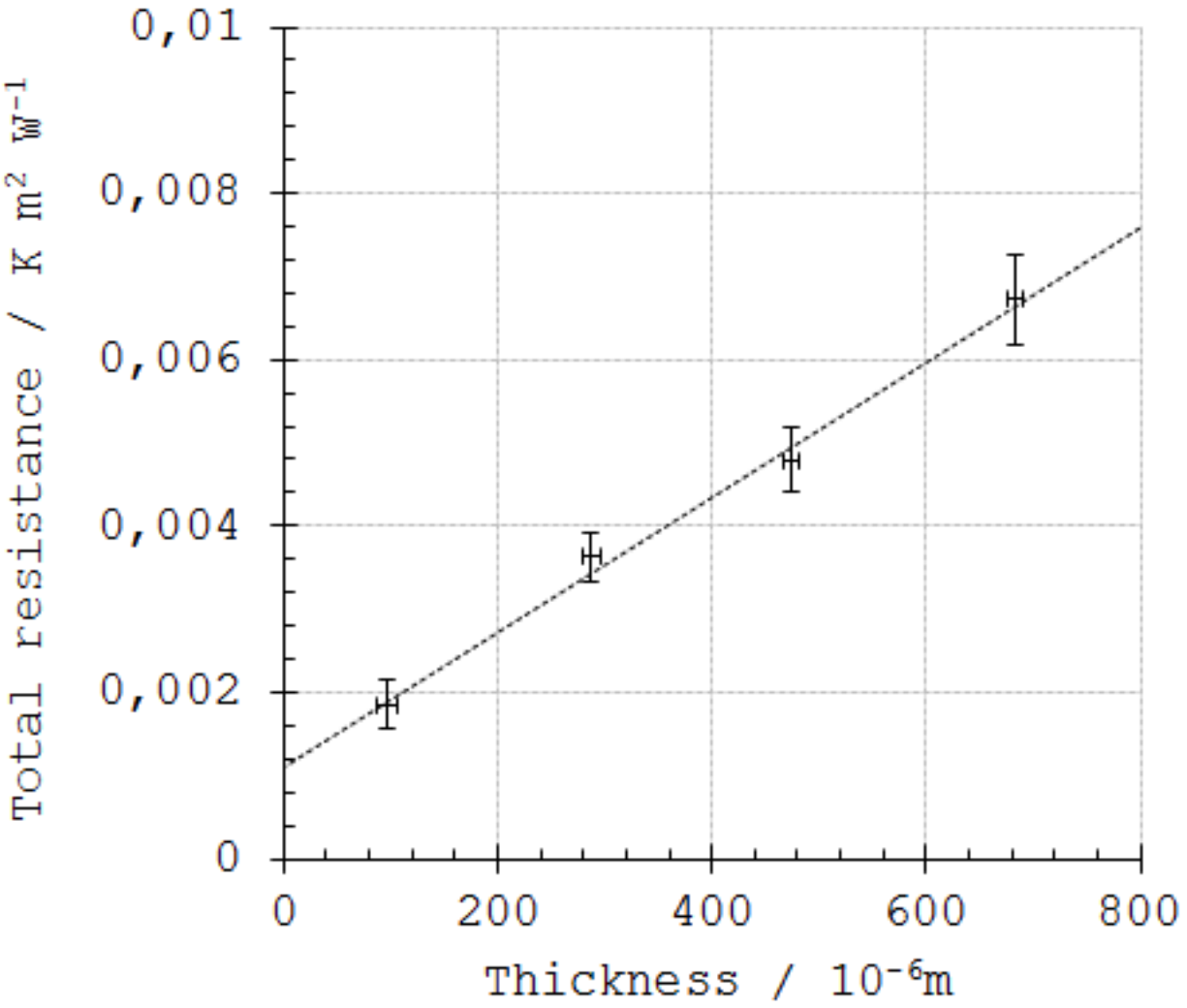

Figure B.15: Plot of the total thermal resistance of four material thicknesses of the plastic coating of the Maxwell PC-10 series supercapacitors, r_{pl}, as a function of the sample thickness, δ_{pl}, at $4.6\,\mathrm{bar}$ compression pressure (during decompression), with axial and vertical 95% confidence error bars, and linear trendline.

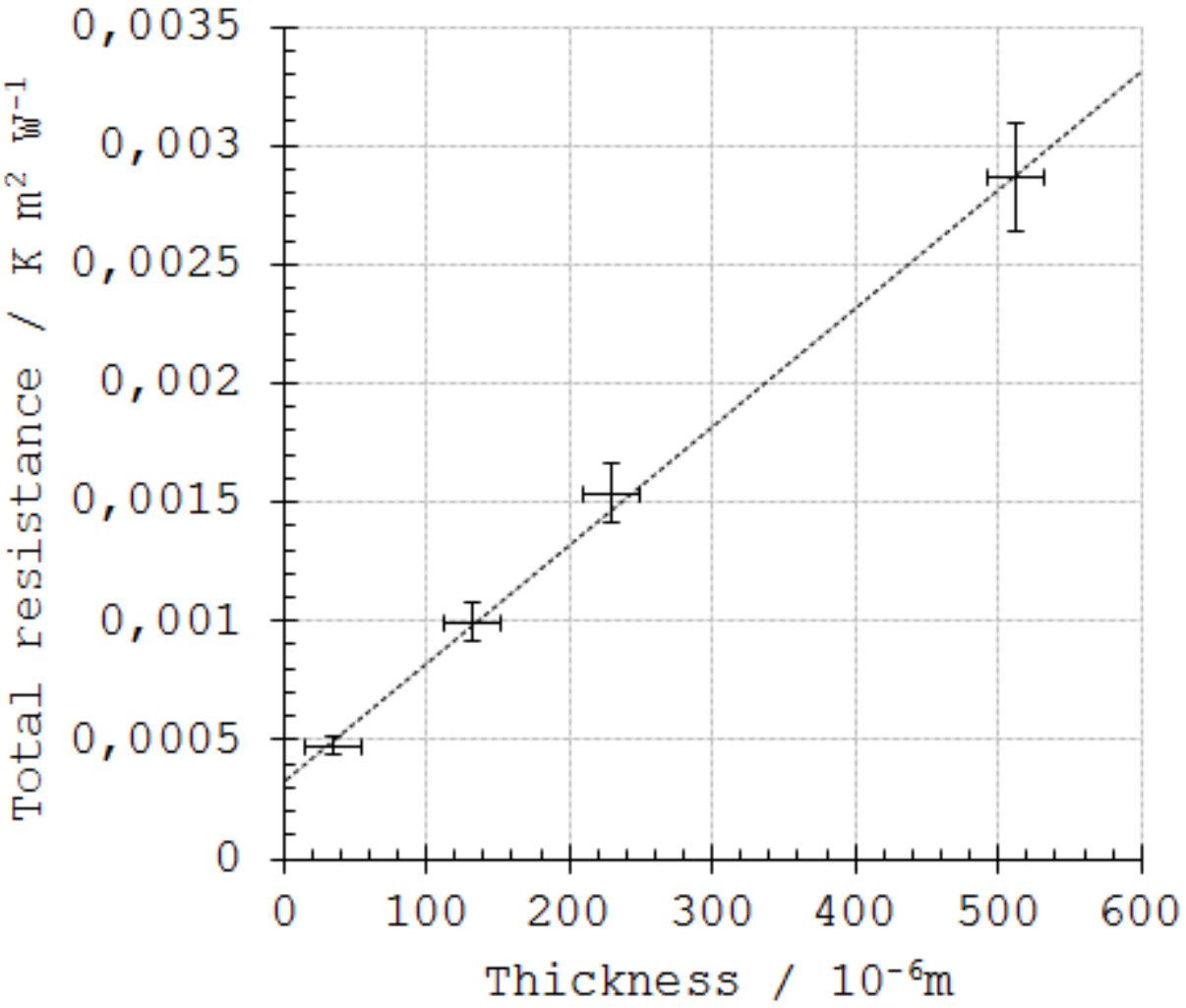

Figure B.16: Plot of the total thermal resistance of four material thicknesses of the separator of the Maxwell PC-10 series supercapacitors, r_{sep}, as a function of the sample thickness, δ_{sep}, at $4.6\,\mathrm{bar}$ compression pressure, with axial and vertical 95% confidence error bars, and linear trendline.

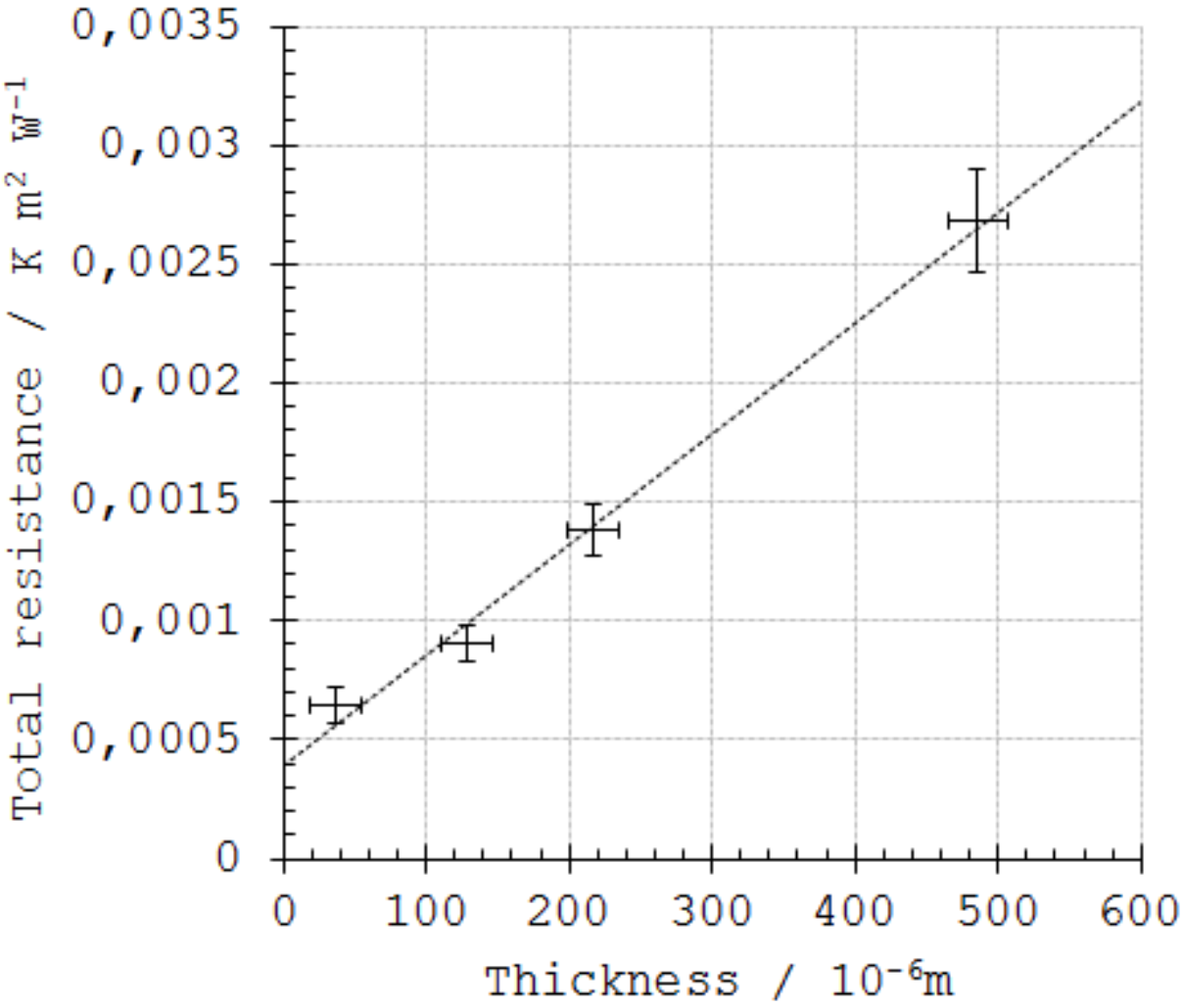

Figure B.17: Plot of the total thermal resistance of four material thicknesses of the separator of the Maxwell PC-10 series supercapacitors, $\mathrm{r_{sep}}$, as a function of the sample thickness, δ_{sep}, at $9.2\,\mathrm{bar}$ compression pressure, with axial and vertical 95% confidence error bars, and linear trendline.

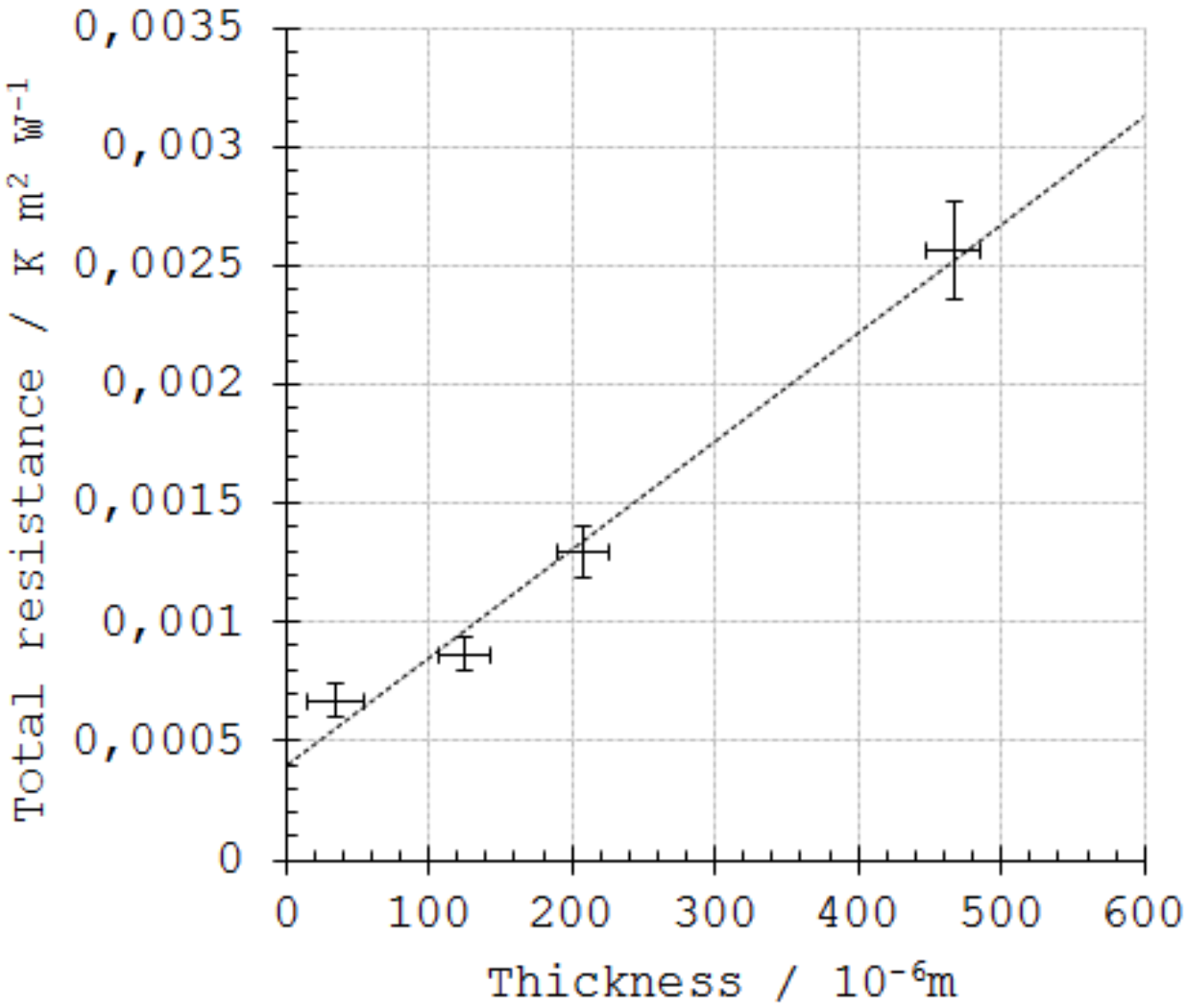

Figure B.18: Plot of the total thermal resistance of four material thicknesses of the separator of the Maxwell PC-10 series supercapacitors, r_{sep}, as a function of the sample thickness, δ_{sep}, at $13.8\,\mathrm{bar}$ compression pressure, with axial and vertical 95% confidence error bars, and linear trendline.

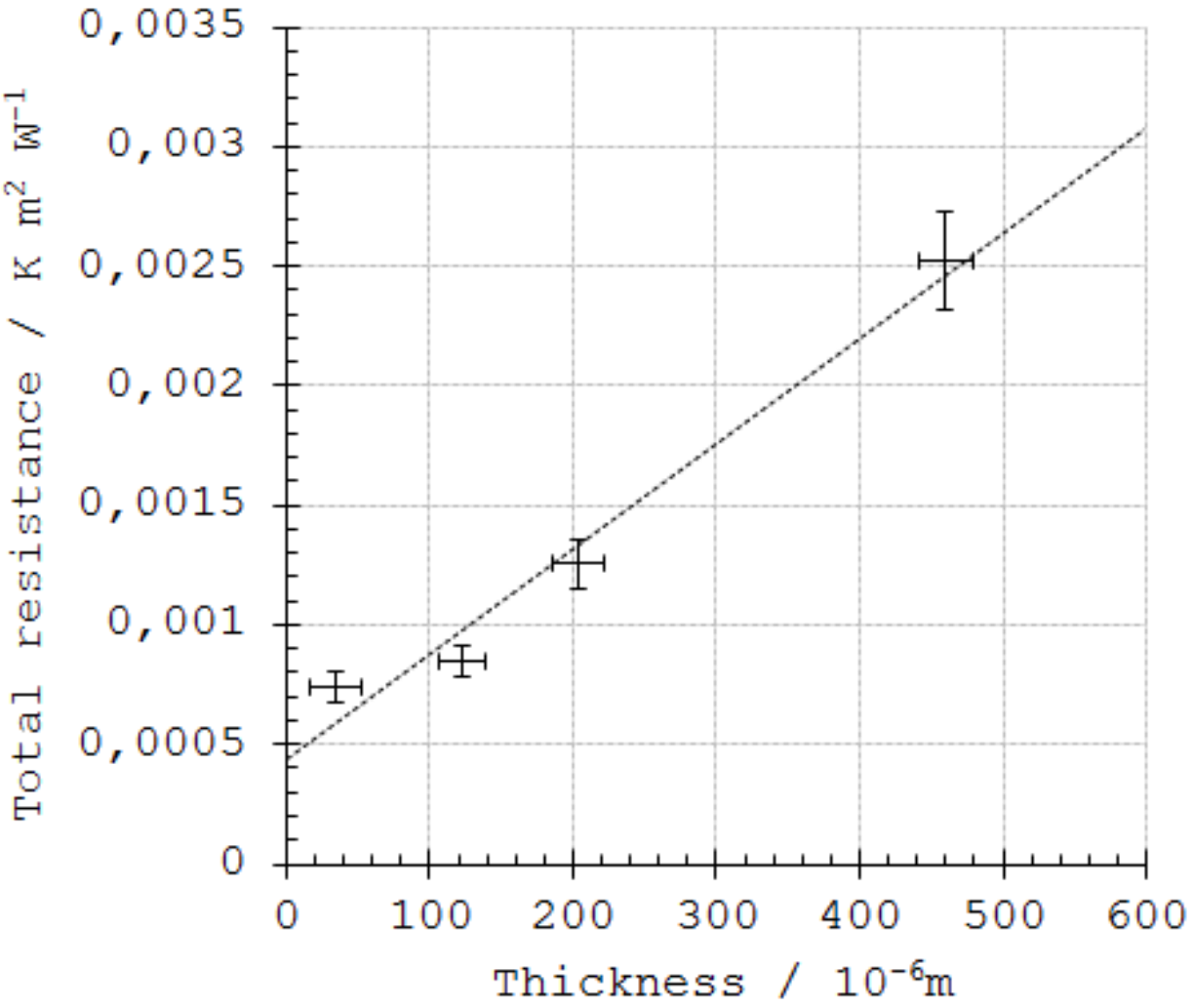

Figure B.19: Plot of the total thermal resistance of four material thicknesses of the separator of the Maxwell PC-10 series supercapacitors, r_{sep}, as a function of the sample thickness, δ_{sep}, at $16.1\,\mathrm{bar}$ compression pressure, with axial and vertical 95% confidence error bars, and linear trendline.

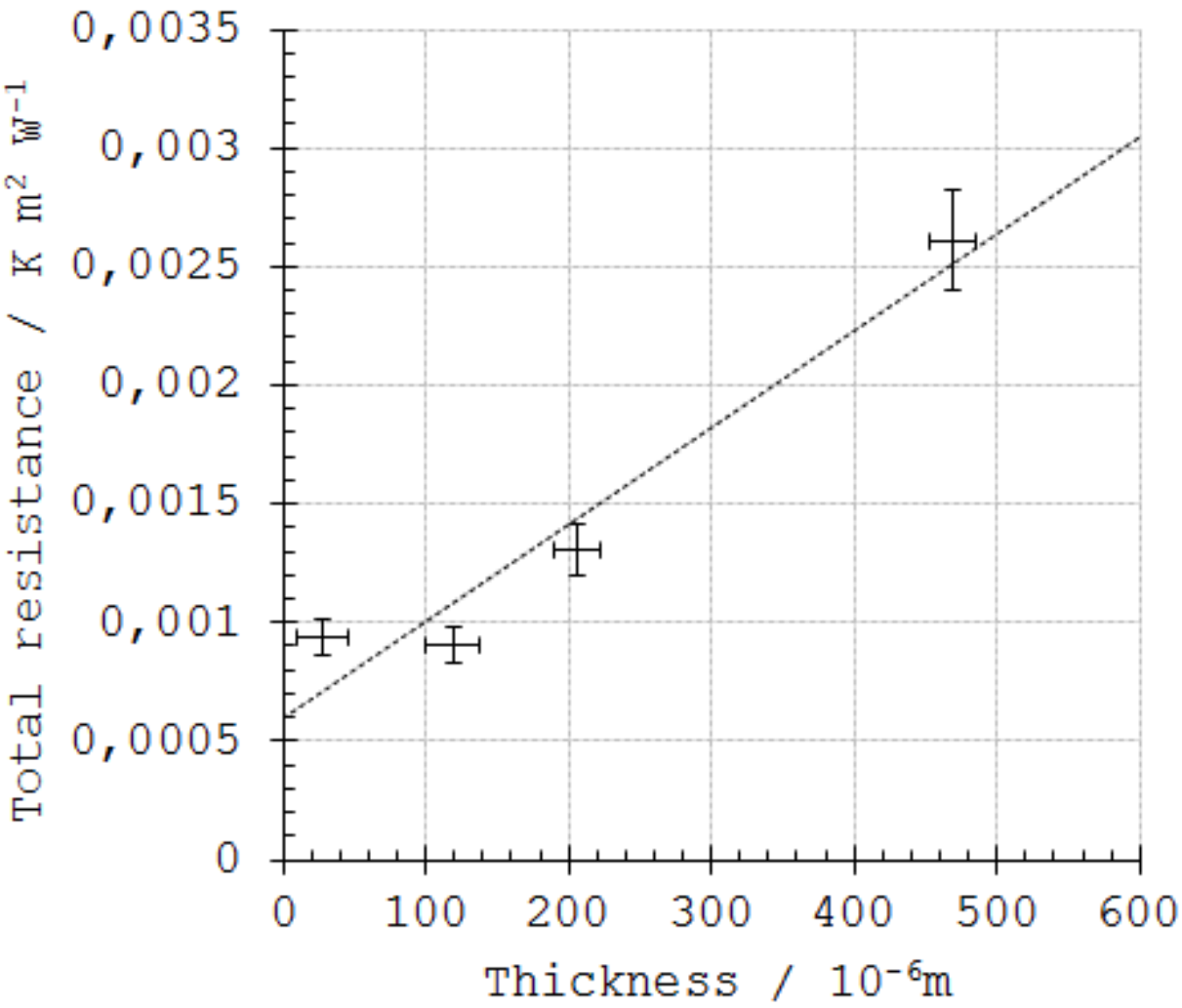

Figure B.20: Plot of the total thermal resistance of four material thicknesses of the separator of the Maxwell PC-10 series supercapacitors, $\mathrm{r_{sep}}$, as a function of the sample thickness, δ_{sep}, at $4.6\,\mathrm{bar}$ compression pressure (during decompression), with axial and vertical 95% confidence error bars, and linear trendline.

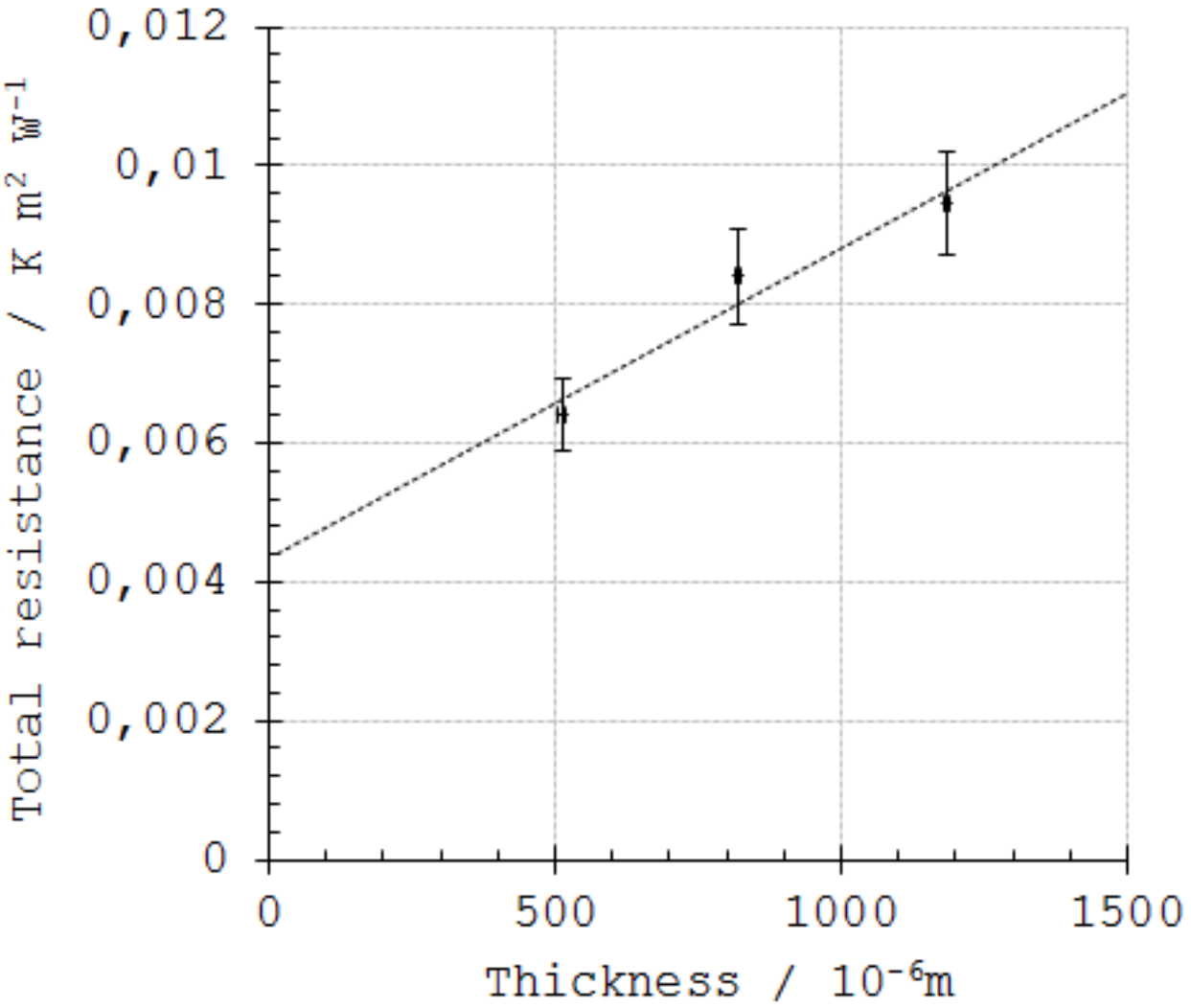

Figure B.21: Plot of the total thermal resistance of three material thicknesses of the steel housing of the Maxwell PC-10 series supercapacitors, r_{sep}, as a function of the sample thickness, δ_{sep}, at $4.6\,\mathrm{bar}$ compression pressure, with axial and vertical 95% confidence error bars, and linear trendline.

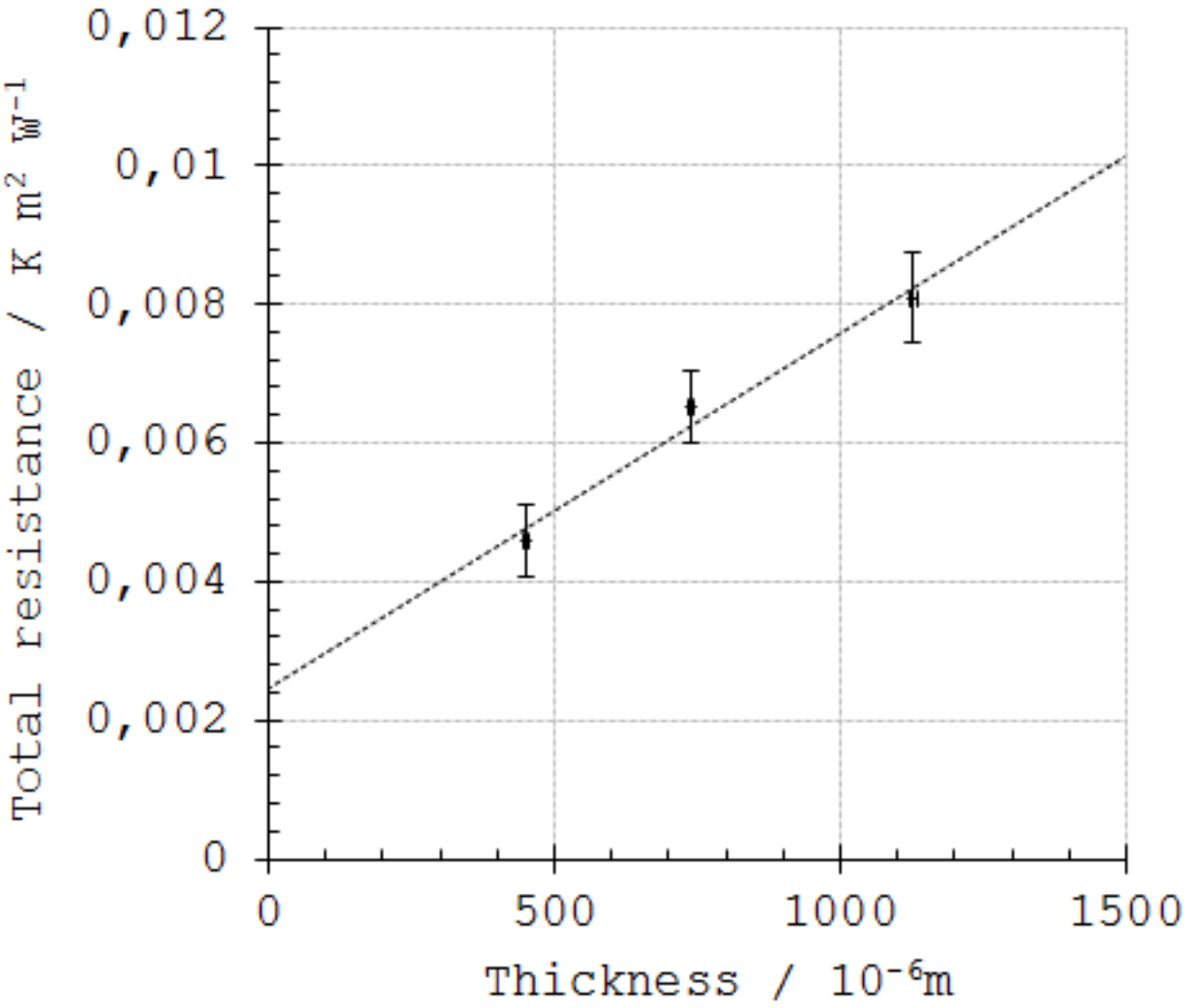

Figure B.22: Plot of the total thermal resistance of three material thicknesses of the steel housing of the Maxwell PC-10 series supercapacitors, r_{sep}, as a function of the sample thickness, δ_{sep}, at $9.2\,\mathrm{bar}$ compression pressure, with axial and vertical 95% confidence error bars, and linear trendline.

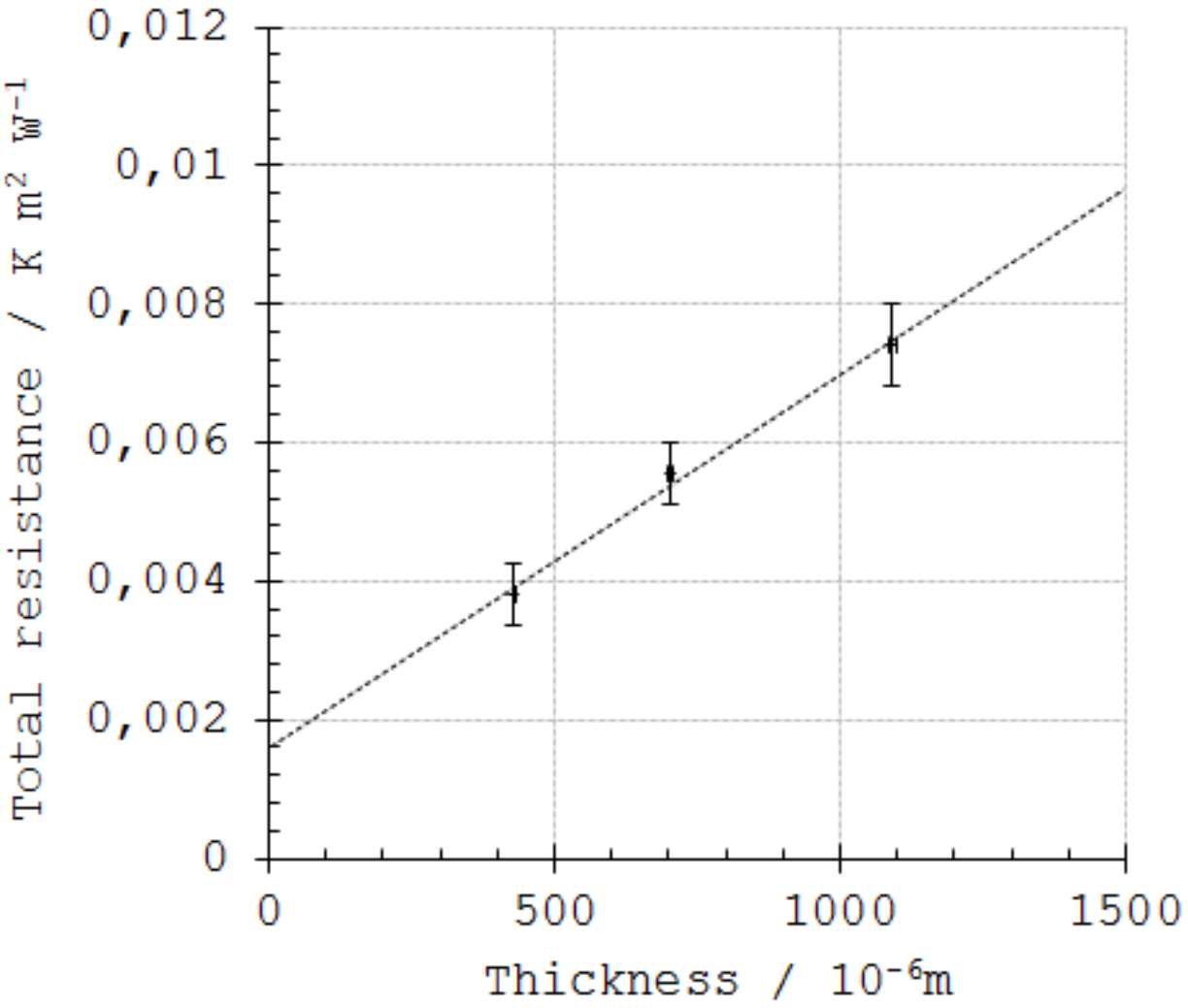

Figure B.23: Plot of the total thermal resistance of three material thicknesses of the steel housing of the Maxwell PC-10 series supercapacitors, $\mathrm{r_{sep}}$, as a function of the sample thickness, δ_{sep}, at $13.8\,\mathrm{bar}$ compression pressure, with axial and vertical 95% confidence error bars, and linear trendline.

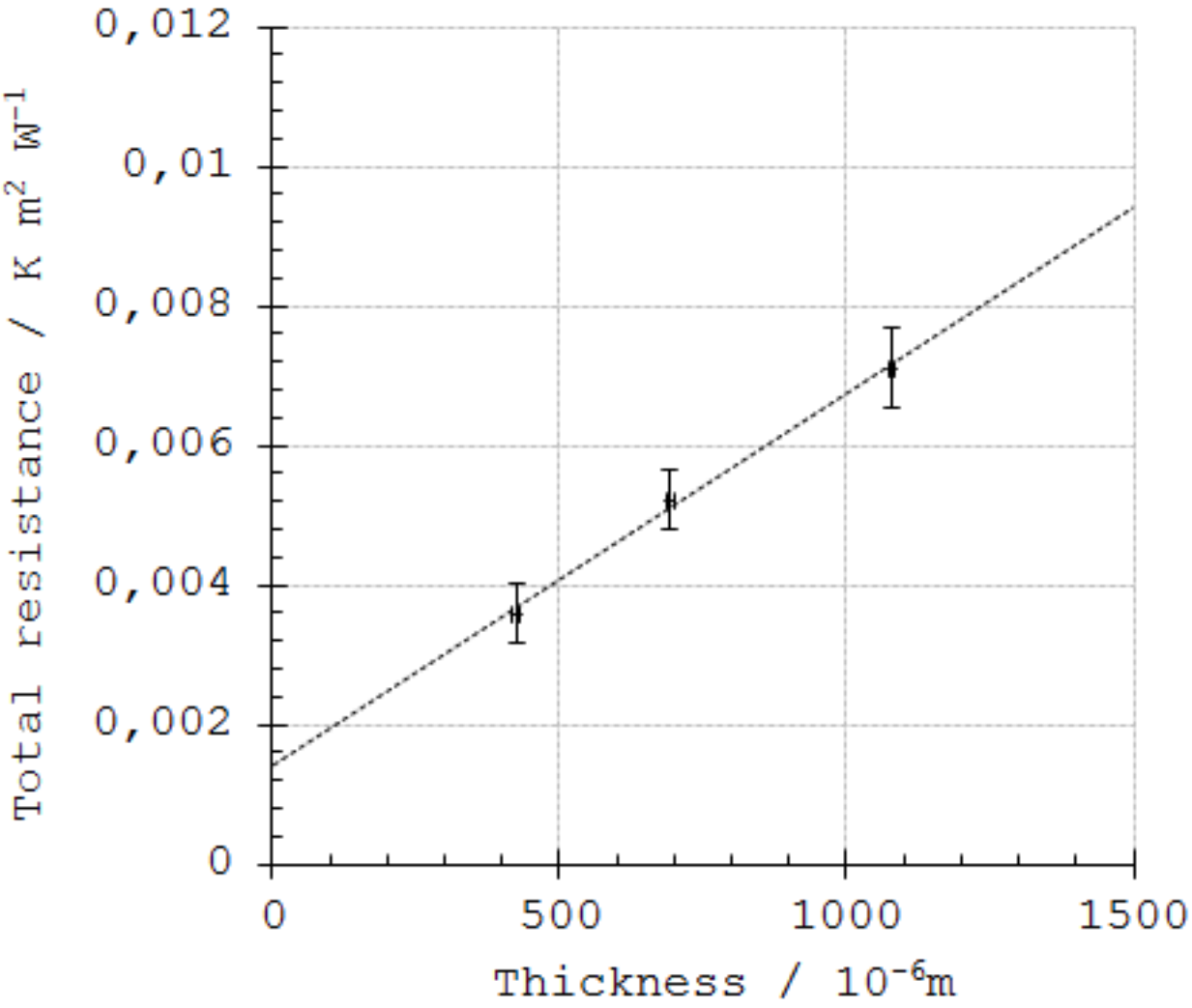

Figure B.24: Plot of the total thermal resistance of three material thicknesses of the steel housing of the Maxwell PC-10 series supercapacitors, r_{sep}, as a function of the sample thickness, δ_{sep}, at $16.1\,\mathrm{bar}$ compression pressure, with axial and vertical 95% confidence error bars, and linear trendline.

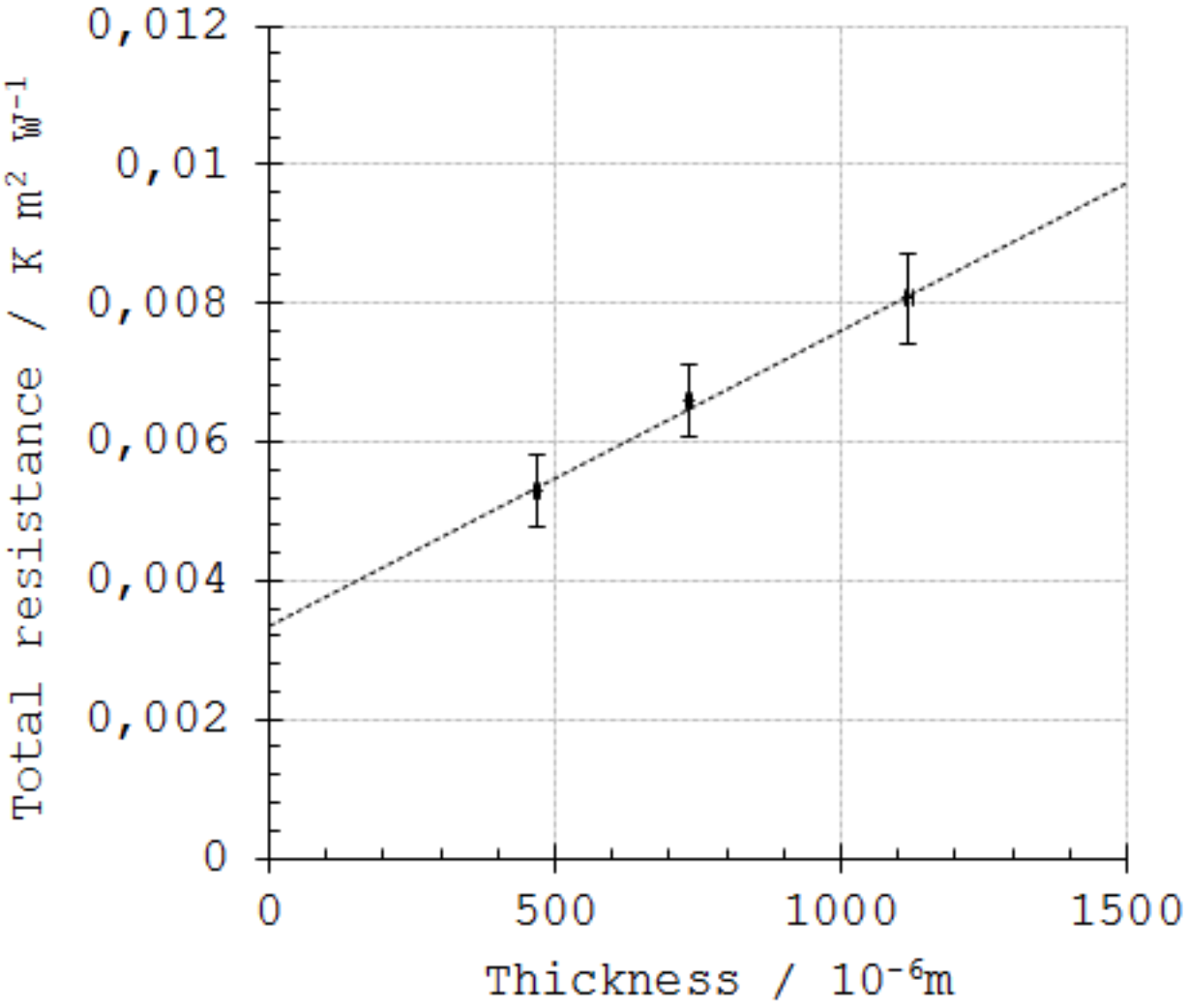

Figure B.25: Plot of the total thermal resistance of three material thicknesses of the steel housing of the Maxwell PC-10 series supercapacitors, r_{sep}, as a function of the sample thickness, δ_{sep}, at $4.6\,\mathrm{bar}$ compression pressure (during decompression), with axial and vertical 95% confidence error bars, and linear trendline.

B.1.2 Calorimetric experiments

Heat Production

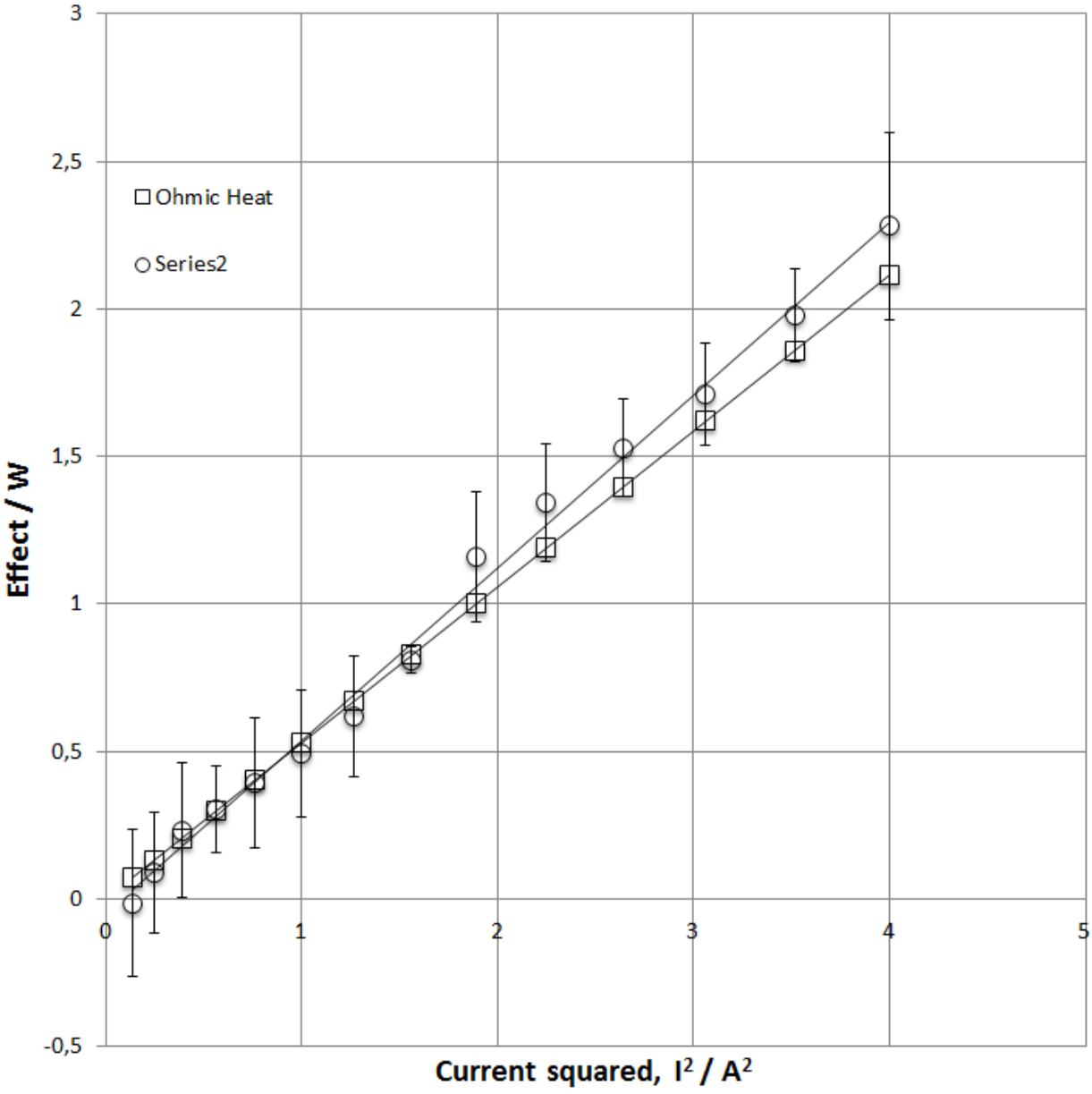

Figure B.26: Total calibrated heat produced by the resistive heating wires inside the heaters of the calorimeter during the first experiment of the A-series (A1), and ohmic heat, RI^2, plotted as a function of the applied current squared, I^2.

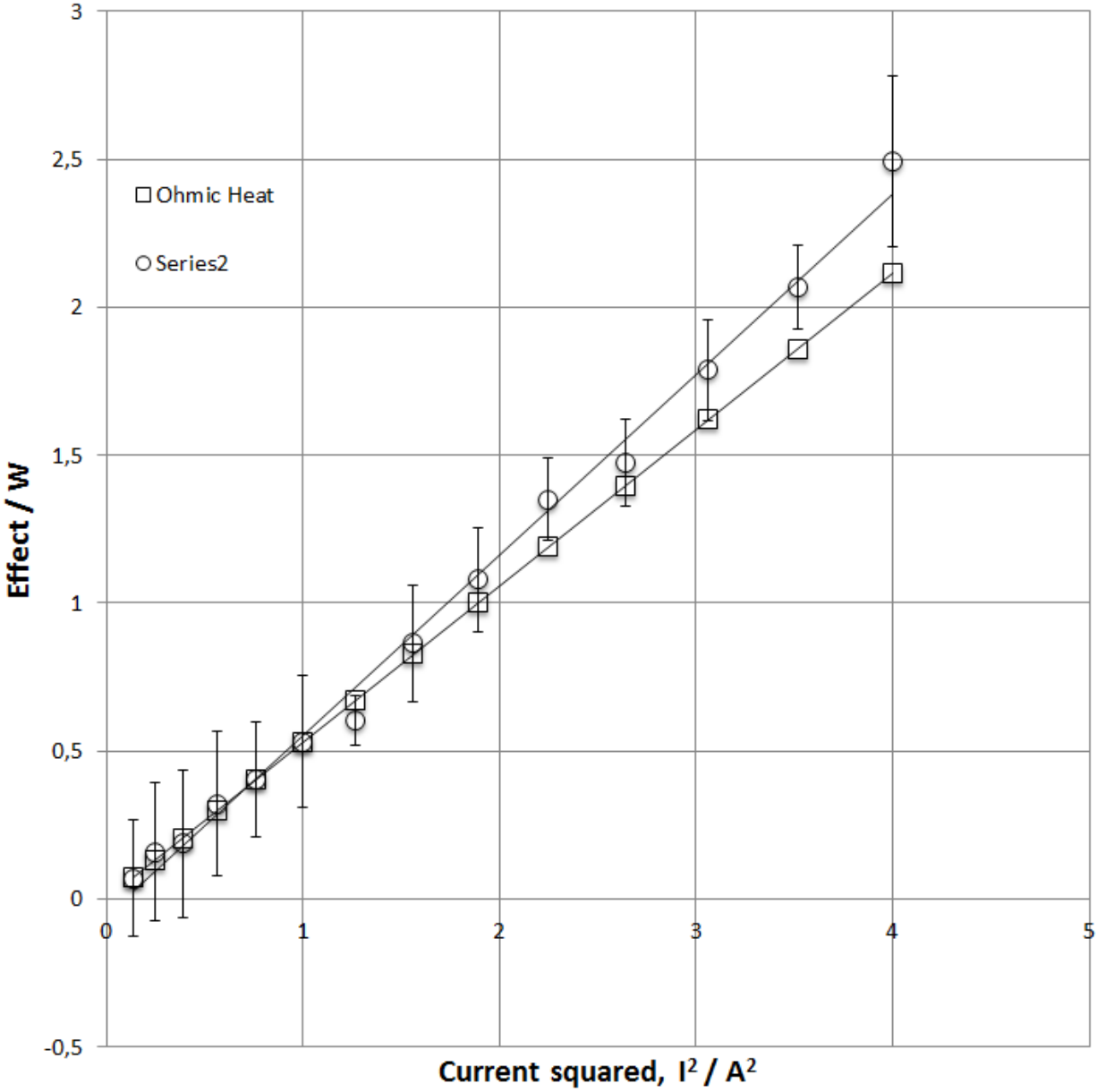

Figure B.27: Total calibrated heat produced by the resistive heating wires inside the heaters of the calorimeter during the second experiment of the A-series (A2), and ohmic heat, RI^2, plotted as a function of the applied current squared, I^2.

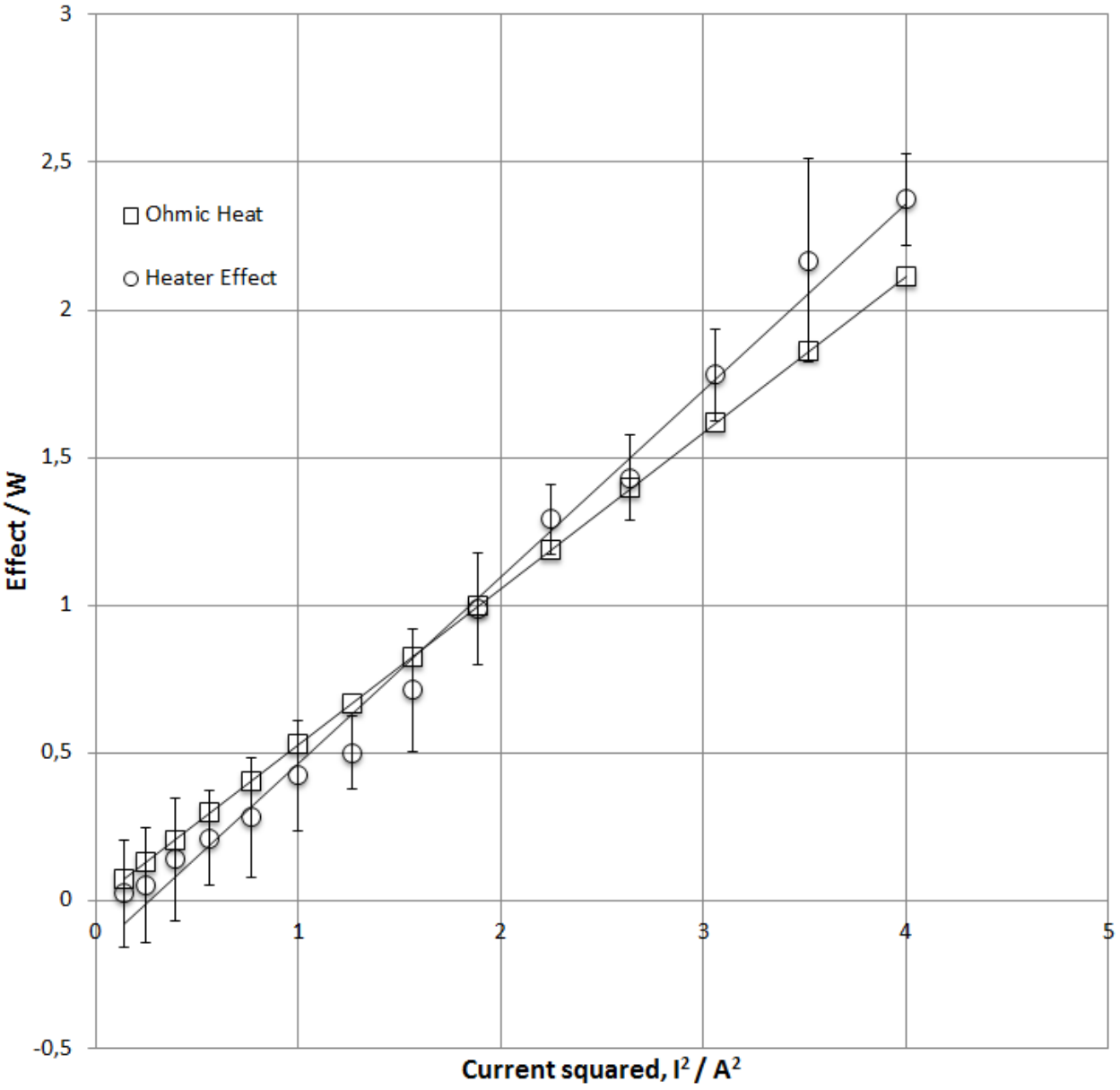

Figure B.28: Total calibrated heat produced by the resistive heating wires inside the heaters of the calorimeter during the third experiment of the A-series (A3), and ohmic heat, RI^2, plotted as a function of the applied current squared, I^2.

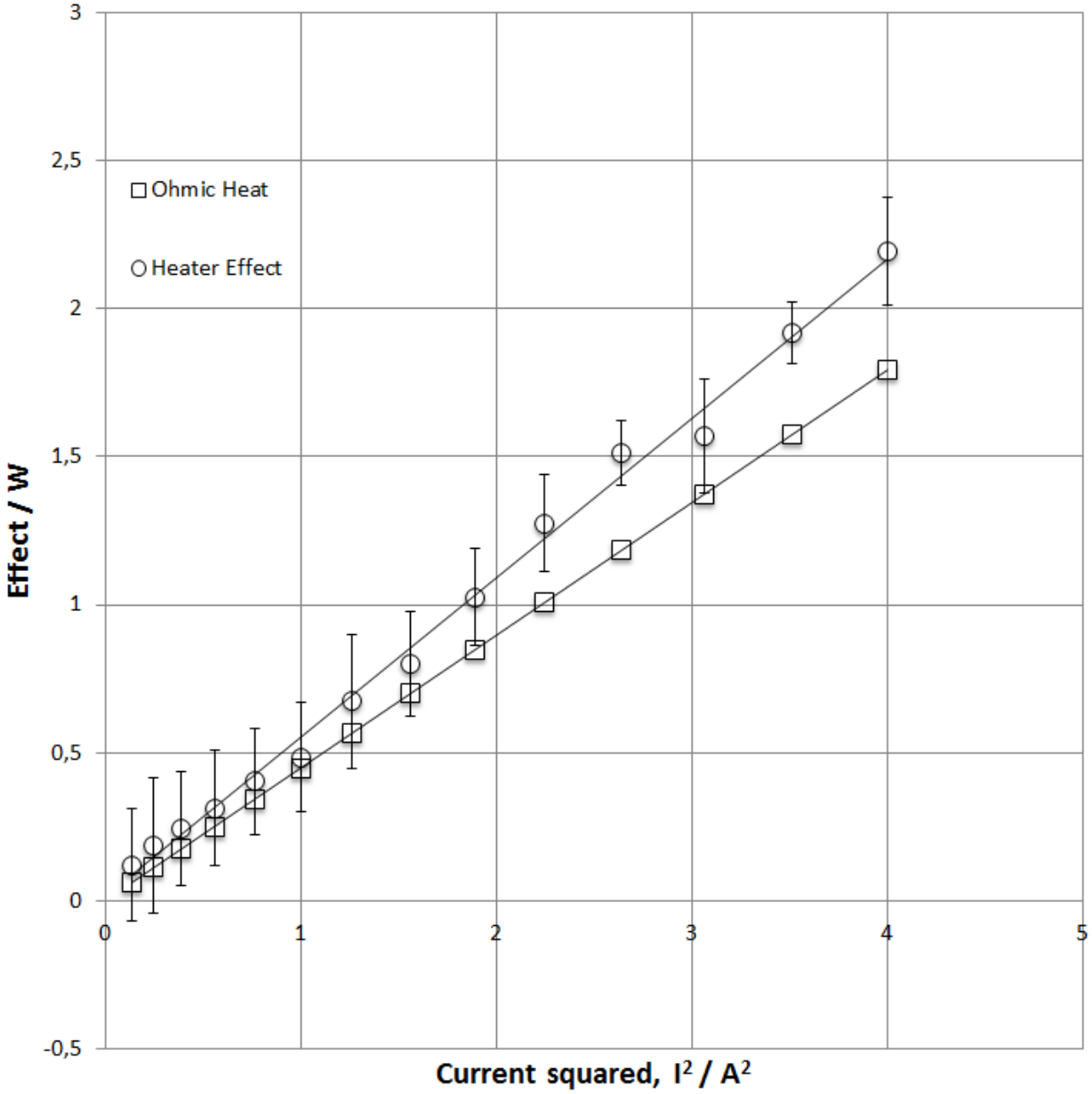

Figure B.29: Total calibrated heat produced by the resistive heating wires inside the heaters of the calorimeter during the first experiment of the B-series (B1), and ohmic heat, RI^2, plotted as a function of the applied current squared, I^2.

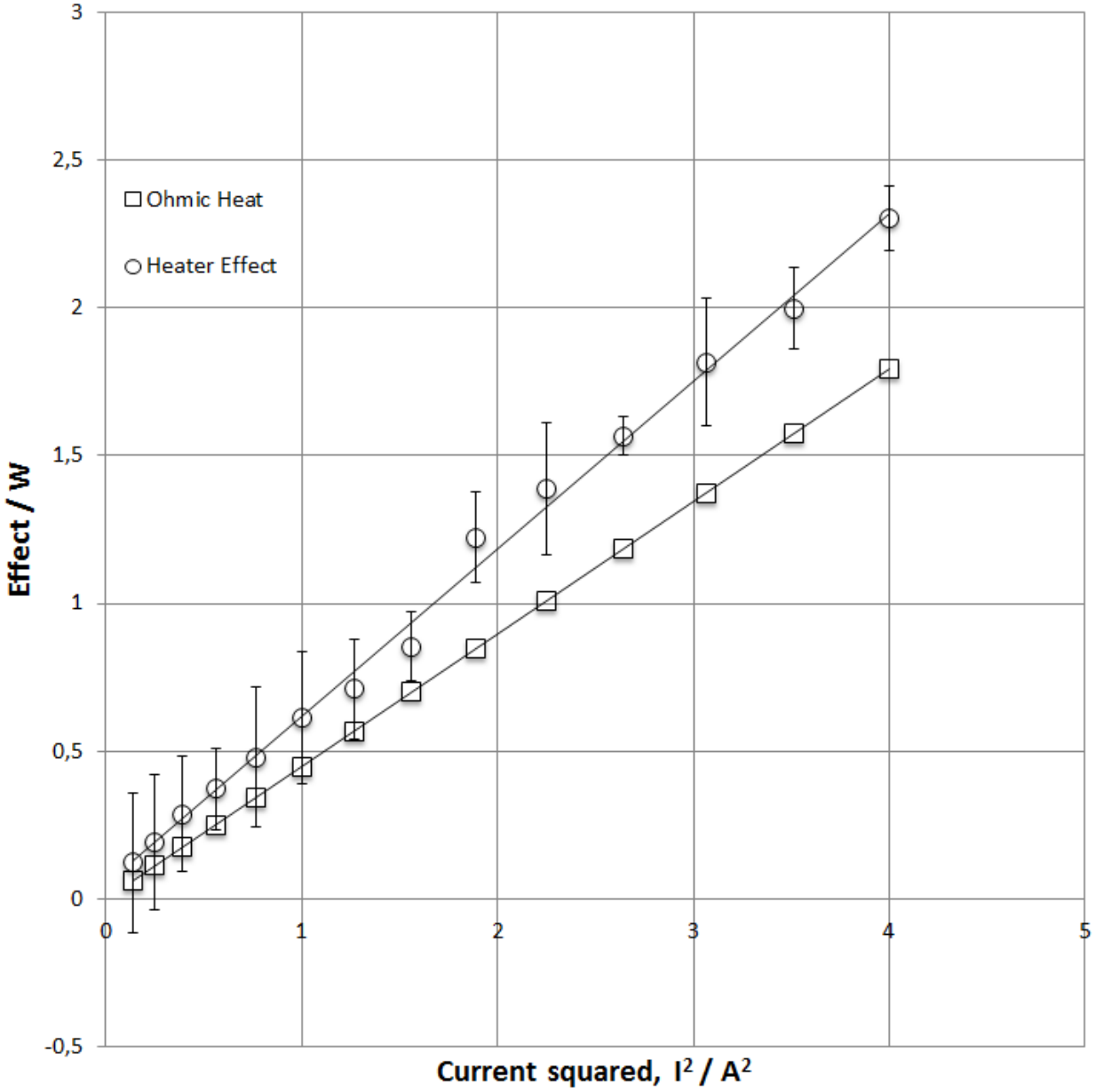

Figure B.30: Total calibrated heat produced by the resistive heating wires inside the heaters of the calorimeter during the second experiment of the B-series (B2), and ohmic heat, RI^2, plotted as a function of the applied current squared, I^2.

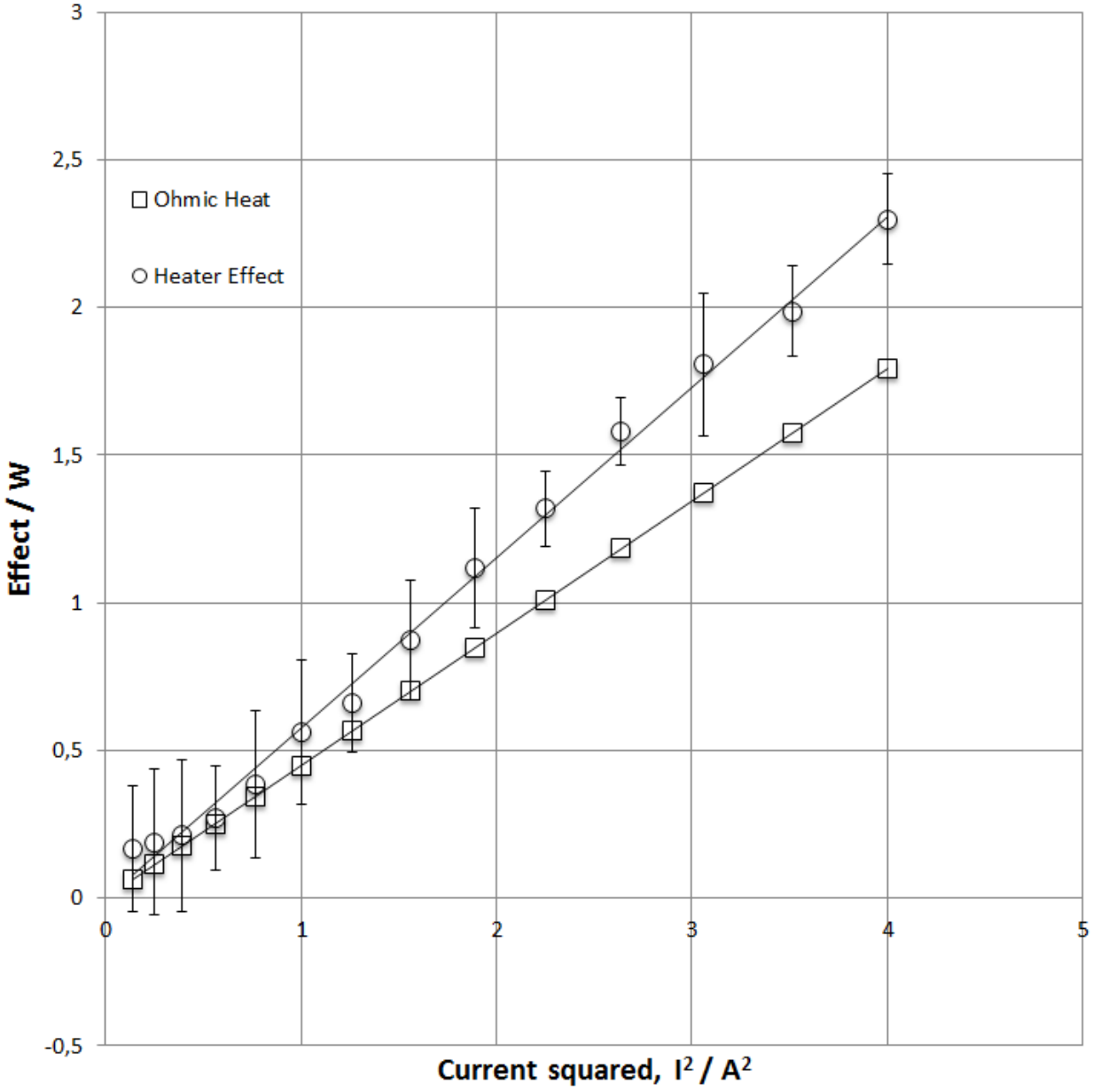

Figure B.31: Total calibrated heat produced by the resistive heating wires inside the heaters of the calorimeter during the third experiment of the B-series (B3), and ohmic heat, RI^2, plotted as a function of the applied current squared, I^2.

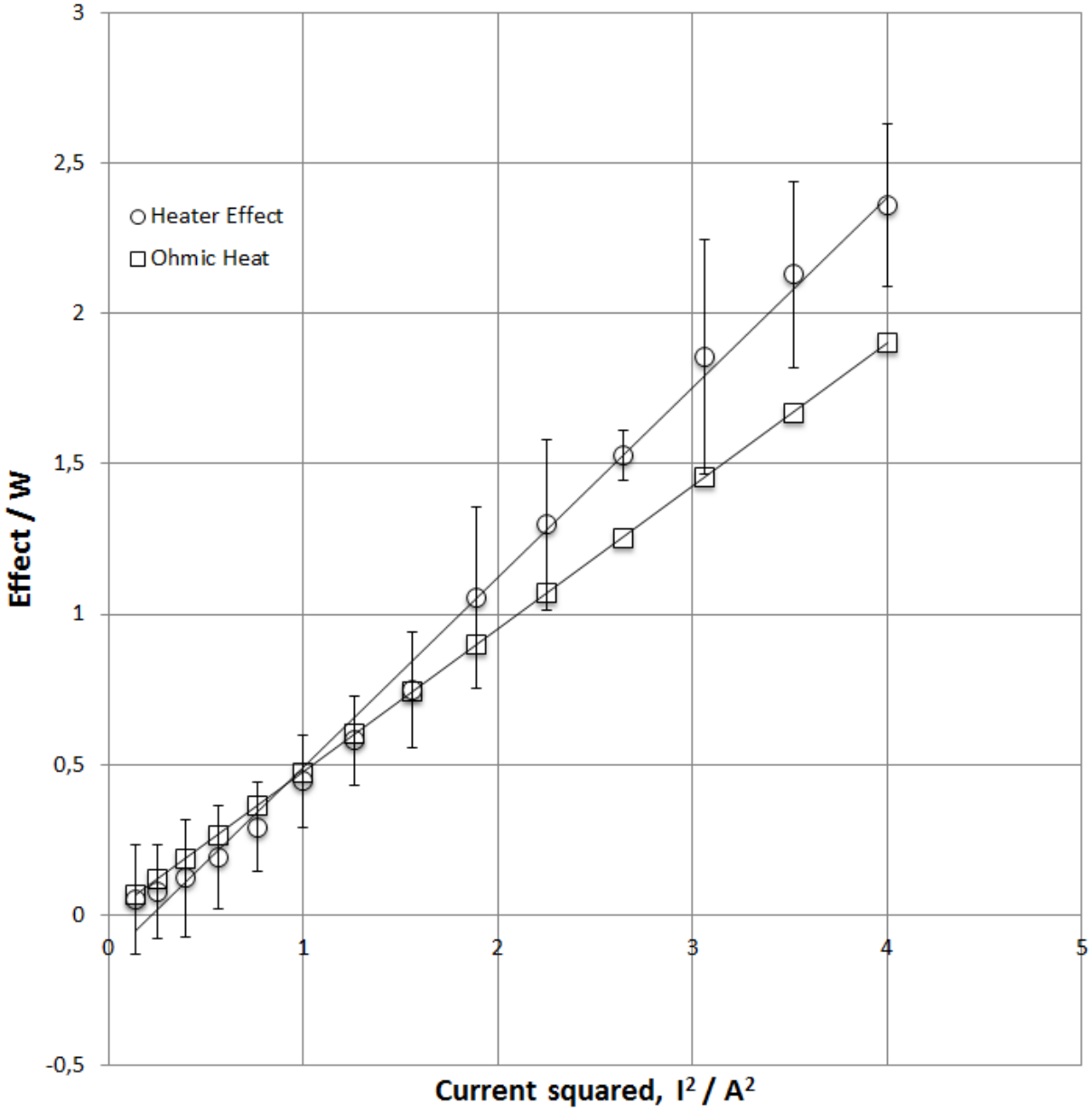

Figure B.32: Total calibrated heat produced by the resistive heating wires inside the heaters of the calorimeter during the first experiment of the C-series (C1), and ohmic heat, RI^2, plotted as a function of the applied current squared, I^2.

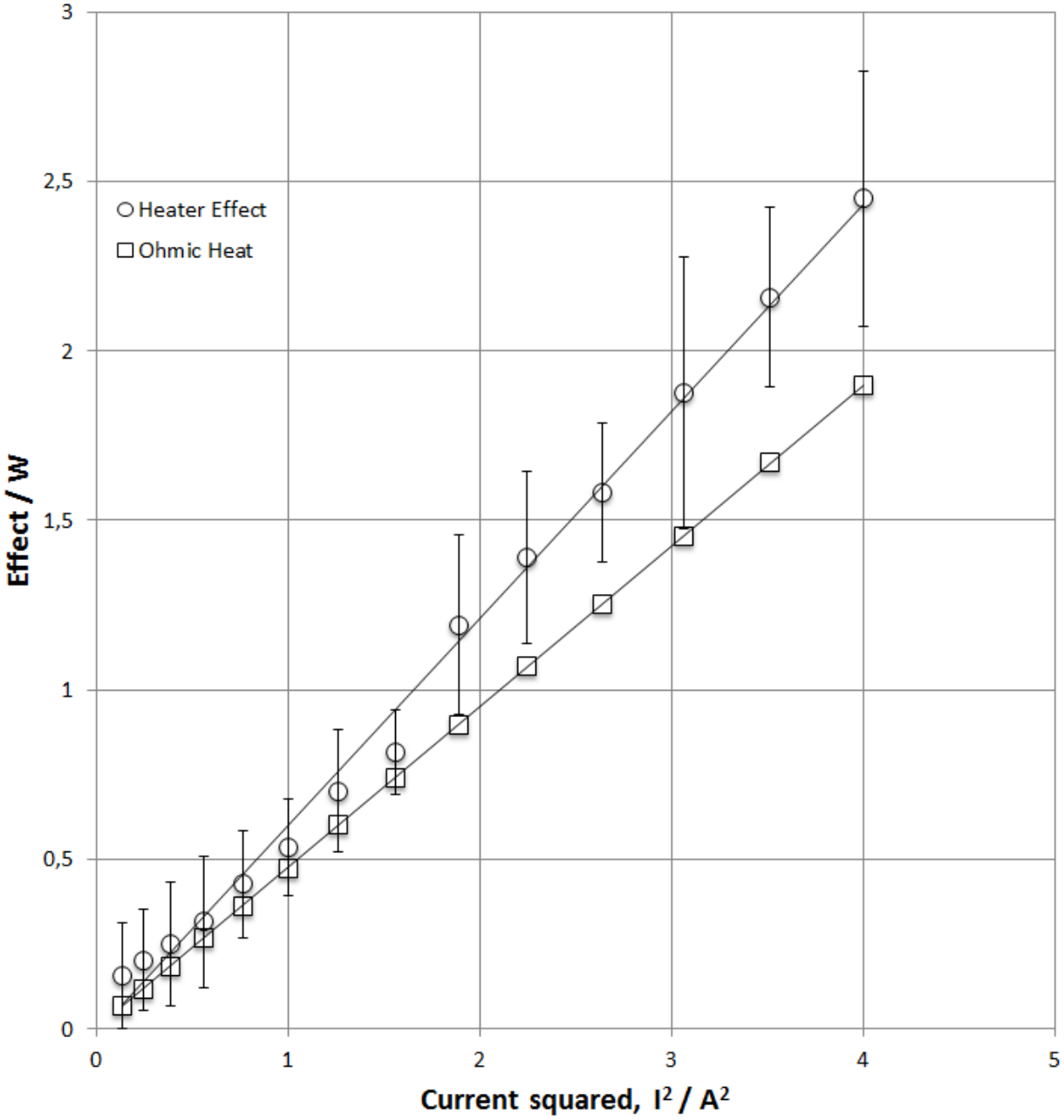

Figure B.33: Total calibrated heat produced by the resistive heating wires inside the heaters of the calorimeter during the second experiment of the C-series (C2), and ohmic heat, RI^2, plotted as a function of the applied current squared, I^2.

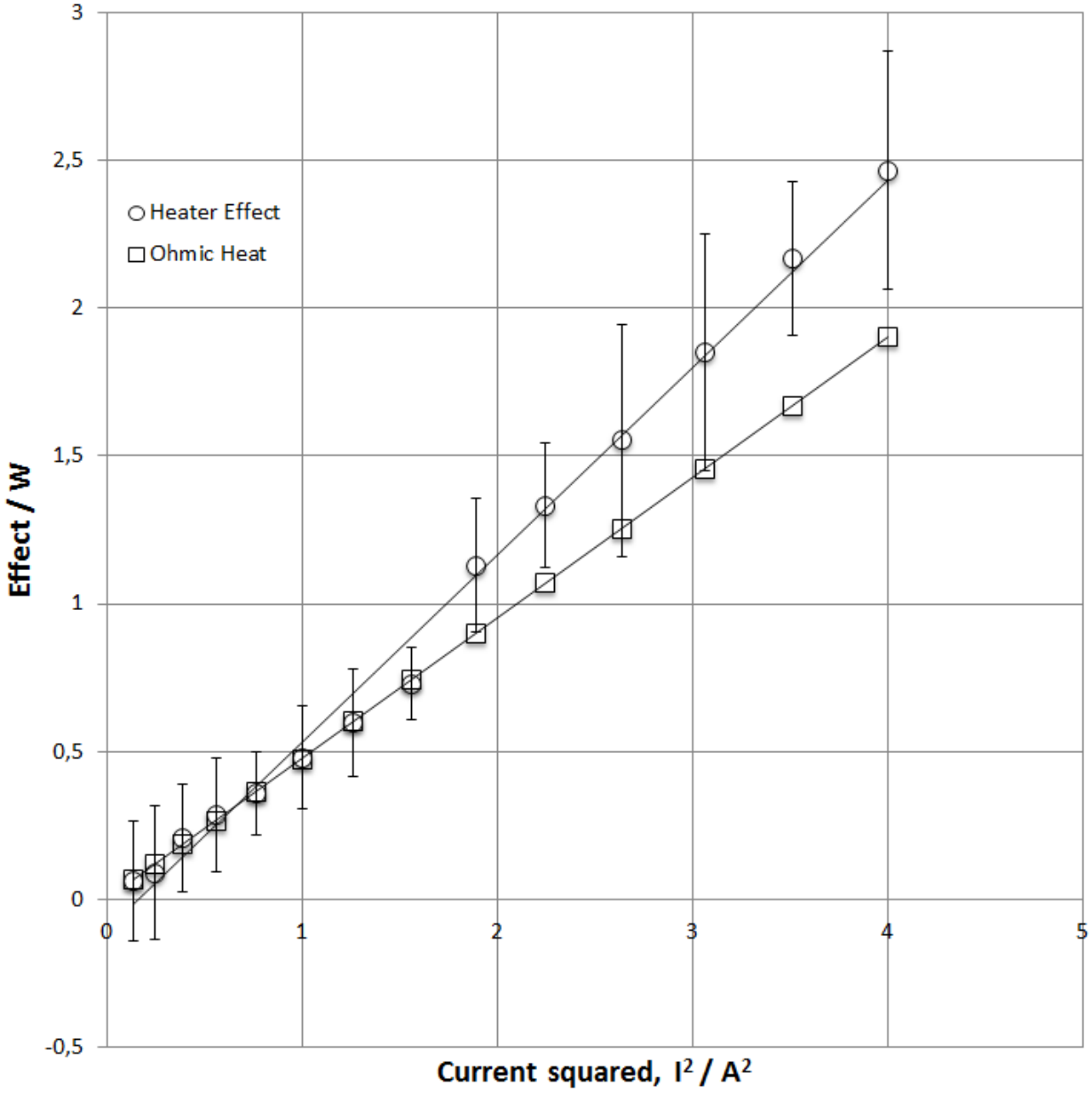

Figure B.34: Total calibrated heat produced by the resistive heating wires inside the heaters of the calorimeter during the third experiment of the C-series (C3), and ohmic heat, RI^2, plotted as a function of the applied current squared, I^2.

Temperature Profiles

In table (B.1) through (B.9) the temperatures measured during the calorimetric experiment series (A, B and C) of the supercapacitors are presented. In figure (B.35), (B.36) and (B.37) the corresponding temperatures are plotted as a function of position across the axial direction in the supercapacitor stack.

Table B.1: Temperature increase at the five thermocouple positions across the supercapacitor stack, ΔT_i, relative to the temperature of approximately $30.0 \pm 0.1°C$ during calibration, as the cycling current is increased stepwise from $0.250\,A$ to $2.000\,A$, during the first experiment of the A-series (A1)

Current $[A]$	ΔT_1 [°C]	ΔT_2 [°C]	ΔT_3 [°C]	ΔT_4 [°C]	ΔT_5 [°C]
0.250	001 ± 0.03	0.05 ± 0.06	0.05 ± 0.05	003 ± 0.03	0.00 ± 0.03
0.375	0.00 ± 0.04	0.16 ± 0.04	0.21 ± 0.06	0.16 ± 0.03	0.00 ± 0.03
0.500	0.00 ± 0.03	0.37 ± 0.12	0.46 ± 0.14	0.35 ± 0.10	0.02 ± 0.03
0.625	0.01 ± 0.03	0.66 ± 0.06	0.84 ± 0.08	0.65 ± 0.07	0.02 ± 0.02
0.750	0.03 ± 0.03	1.01 ± 0.15	1.27 ± 0.18	0.96 ± 0.13	0.04 ± 0.03
0.875	0.07 ± 0.06	1.48 ± 0.08	1.87 ± 0.09	1.44 ± 0.07	0.08 ± 0.06
1.000	008 ± 0.06	1.94 ± 0.14	2.47 ± 0.20	1.91 ± 0.15	0.10 ± 0.06
1.125	0.11 ± 0.04	2.51 ± 0.19	3.19 ± 0.24	2.47 ± 0.17	0.14 ± 0.03
1.250	0.16 ± 0.02	3.27 ± 0.03	4.16 ± 0.02	3.23 ± 0.00	0.18 ± 0.00
1.375	028 ± 0.06	4.77 ± 0.20	6.07 ± 0.26	4.68 ± 0.18	0.26 ± 0.05
1.500	0.32 ± 0.04	5.71 ± 0.18	7.29 ± 0.24	5.60 ± 0.18	0.32 ± 0.03
1.625	0.35 ± 0.03	6.81 ± 0.09	8.75 ± 0.13	6.69 ± 0.09	0.39 ± 0.03
1.750	0.43 ± 0.03	7.79 ± 0.14	9.97 ± 0.17	7.64 ± 0.13	0.45 ± 0.06
1.875	0.46 ± 0.06	9.01 ± 0.18	11.60 ± 0.25	8.88 ± 0.17	0.52 ± 0.01
2.000	0.55 ± 0.02	10.31 ± 0.18	13.35 ± 0.24	10.21 ± 0.18	0.58 ± 0.03

Table B.2: Temperature increase at the five thermocouple positions across the supercapacitor stack, $\Delta \mathrm{T_i}$, relative to the temperature of approximately $30.0 \pm 0.1°\mathrm{C}$ during calibration, as the cycling current is increased stepwise from $0.250\,\mathrm{A}$ to $2.000\,\mathrm{A}$, during the second experiment of the A-series (A2)

Current $[A]$	$\Delta \mathrm{T}_1$ [°C]	$\Delta \mathrm{T}_2$ [°C]	$\Delta \mathrm{T}_3$ [°C]	$\Delta \mathrm{T}_4$ [°C]	$\Delta \mathrm{T}_5$ [°C]
0.250	-0.07 ± 0.06	-0.01 ± 0.03	0.01 ± 0.03	$0.00 \pm 0,03$	-0.02 ± 0.03
0.375	$-0,05 \pm 0.06$	0.13 ± 0.06	0.18 ± 0.07	$0.14 \pm 0,06$	-0.01 ± 0.03
0.500	-0.02 ± 0.03	0.35 ± 0.04	0.47 ± 0.05	$0.35 \pm 0,03$	0.01 ± 0.03
0.625	0.01 ± 0.06	0.65 ± 0.13	0.82 ± 0.17	$0.63 \pm 0,13$	0.03 ± 0.02
0.750	-0.05 ± 0.09	0.93 ± 0.14	1.21 ± 0.17	$0.91 \pm 0,12$	0.01 ± 0.03
0.875	0.01 ± 0.03	1.40 ± 0.16	1.79 ± 0.21	$1.36 \pm 0,16$	0.04 ± 0.03
1.000	0.03 ± 0.03	1.92 ± 0.17	2.46 ± 0.22	$1.85 \pm 0,15$	0.06 ± 0.04
1.125	0.12 ± 0.07	2.51 ± 0.24	3.19 ± 0.29	$2.44 \pm 0,21$	0.12 ± 0.01
1.250	0.13 ± 0.03	3.23 ± 0.06	4.14 ± 0.09	$3.14 \pm 0,05$	0.15 ± 0.02
1.375	0.23 ± 0.03	4.72 ± 0.29	6.03 ± 0.37	$4.62 \pm 0,27$	0.24 ± 0.02
1.500	0.31 ± 0.03	5.81 ± 0.14	7.46 ± 0.17	$5.70 \pm 0,12$	0.31 ± 0.02
1.625	0.36 ± 0.03	6.76 ± 0.23	8.69 ± 0.32	$6.65 \pm 0,22$	0.35 ± 0.03
1.750	0.36 ± 0.03	7.86 ± 0.17	10.18 ± 0.23	$7.82 \pm 0,16$	0.39 ± 0.02
1.875	0.42 ± 0.03	9.17 ± 0.21	11.93 ± 0.27	$9.19 \pm 0,19$	0.49 ± 0.01
2.000	0.53 ± 0.02	10.65 ± 0.15	13.93 ± 0.19	10.79 ± 0.12	0.58 ± 0.02

Table B.3: Temperature increase at the five thermocouple positions across the supercapacitor stack, $\Delta \mathrm{T_i}$, relative to the temperature of approximately $30.0 \pm 0.1°\mathrm{C}$ during calibration, as the cycling current is increased stepwise from $0.250\,\mathrm{A}$ to $2.000\,\mathrm{A}$, during the third experiment of the A-series (A3)

Current $[A]$	$\Delta \mathrm{T}_1$ [°C]	$\Delta \mathrm{T}_2$ [°C]	$\Delta \mathrm{T}_3$ [°C]	$\Delta \mathrm{T}_4$ [°C]	$\Delta \mathrm{T}_5$ [°C]
0.250	-010 ± 0.04	-0.03 ± 0.03	-0.01 ± 0.03	-0.01 ± 0.03	-0.03 ± 0.03
0.375	-0.07 ± 0.06	0.11 ± 0.04	0.17 ± 0.05	0.13 ± 0.04	-0.02 ± 0.03
0.500	-0.04 ± 0.06	0.33 ± 0.06	0.45 ± 0.08	0.34 ± 0.05	-0.01 ± 0.03
0.625	-0.04 ± 0.04	0.63 ± 0.03	0.83 ± 0.06	0.63 ± 0.06	0.00 ± 0.03
0.750	-0.03 ± 0.03	0.99 ± 0.08	1.28 ± 0.08	0.97 ± 0.05	0.02 ± 0.03
0.875	0.01 ± 0.04	1.38 ± 0.27	1.79 ± 0.36	1.37 ± 0.28	0.04 ± 0.03
1.000	0.02 ± 0.02	1.92 ± 0.23	2.48 ± 0.31	1.90 ± 0.24	0.06 ± 0.03
1.125	0.07 ± 0.05	2.53 ± 0.24	3.25 ± 0.30	2.49 ± 0.21	0.09 ± 0.06
1.250	0.08 ± 0.06	3.18 ± 0.27	4.11 ± 0.37	3.15 ± 0.28	0.14 ± 0.03
1.375	0.22 ± 0.04	4.89 ± 0.27	6.30 ± 0.33	4.85 ± 0.25	0.23 ± 0.03
1.500	0.21 ± 0.03	5.88 ± 0.20	7.64 ± 0.25	5.87 ± 0.20	0.26 ± 0.05
1.625	0.33 ± 0.06	6.97 ± 0.29	9.05 ± 0.37	6.99 ± 0.28	0.33 ± 0.02
1.750	0.35 ± 0.04	8.08 ± 0.21	10.58 ± 0.29	8.19 ± 0.21	0.40 ± 0.01
1.875	0.43 ± 0.04	9.49 ± 0.21	12.46 ± 0.31	9.68 ± 0.23	0.45 ± 0.06
2.000	0.52 ± 0.03	10.79 ± 0.13	14.23 ± 0.16	11.15 ± 0.10	0.54 ± 0.03

Table B.4: Temperature increase at the five thermocouple positions across the supercapacitor stack, $\Delta \mathrm{T_i}$, relative to the temperature of approximately $30.0 \pm 0.1°\mathrm{C}$ during calibration, as the cycling current is increased stepwise from $0.250\ \mathrm{A}$ to $2.000\ \mathrm{A}$, during the first experiment of the B-series (B1)

Current $[A]$	$\Delta \mathrm{T}_1$ [°C]	$\Delta \mathrm{T}_2$ [°C]	$\Delta \mathrm{T}_3$ [°C]	$\Delta \mathrm{T}_4$ [°C]	$\Delta \mathrm{T}_5$ [°C]
0.250	-0.04 ± 0.03	-0.01 ± 0.04	0.02 ± 0.06	0.00 ± 0.03	-0.02 ± 0.04
0.375	-0.04 ± 0.03	0.06 ± 0.03	0.14 ± 0.03	0.11 ± 0.02	-0.01 ± 0.03
0.500	-0.03 ± 0.03	0.20 ± 0.05	0.34 ± 0.08	0.24 ± 0.06	0.00 ± 003
0.625	-0.01 ± 0.03	0.42 ± 0.05	0.65 ± 0.05	0.45 ± 0.06	0.02 ± 0.04
0.750	0.04 ± 0.06	0.69 ± 0.08	1.02 ± 0.13	0.69 ± 0.07	0.06 ± 0.06
0.875	0.07 ± 0.02	0.98 ± 0.04	1.48 ± 0.10	0.99 ± 0.07	0.08 ± 0.06
1.000	0.10 ± 0.03	1.33 ± 0.09	1.96 ± 0.15	131 ± 0.10	0.10 ± 0.04
1.125	0.12 ± 0.03	1.72 ± 0.11	2.54 ± 0.20	1.71 ± 0.13	0.14 ± 0.03
1.250	0.16 ± 0.03	2.17 ± 0.14	3.17 ± 0.24	2.12 ± 0.15	0.15 ± 0.02
1.375	0.29 ± 0.04	3.24 ± 0.16	4.72 ± 0.26	3.15 ± 0.15	0.20 ± 0.03
1.500	0.32 ± 0.02	3.84 ± 0.15	5.61 ± 0.24	3.77 ± 0.14	0.29 ± 0.04
1.625	0.34 ± 0.03	4.46 ± 0.16	6.53 ± 0.29	4.38 ± 0.19	0.32 ± 0.03
1.750	0.35 ± 0.03	4.92 ± 0.16	7.17 ± 0.24	4.84 ± 0.15	0.34 ± 0.03
1.875	0.40 ± 0.06	5.68 ± 0.16	8.26 ± 0.27	5.59 ± 0.17	0.39 ± 0.03
2.000	0.53 ± 0.03	6.69 ± 0.06	9.77 ± 0.13	6.56 ± 0.09	0.46 ± 0.06

Table B.5: Temperature increase at the five thermocouple positions across the supercapacitor stack, ΔT_i, relative to the temperature of approximately $30.0 \pm 0.1°C$ during calibration, as the cycling current is increased stepwise from $0.250\,A$ to $2.000\,A$, during the second experiment of the B-series (B2)

Current $[A]$	ΔT_1 [°C]	ΔT_2 [°C]	ΔT_3 [°C]	ΔT_4 [°C]	ΔT_5 [°C]
0.250	-0.07 ± 0.03	-0.07 ± 0.05	-0.01 ± 0.03	-0.01 ± 0.02	-0.02 ± 0.03
0.375	-0.07 ± 0.03	0.03 ± 0.04	0.11 ± 0.04	0.09 ± 0.05	-0.01 ± 0.03
0.500	-0.06 ± 0.04	0.19 ± 0.04	0.32 ± 0.04	0.24 ± 0.04	0.00 ± 0.04
0.625	-0.03 ± 0.03	0.40 ± 0.04	0.63 ± 0.04	0.44 ± 0.04	0.01 ± 0.04
0.750	-0.02 ± 0.02	0.63 ± 0.04	0.97 ± 0.09	0.66 ± 0.06	0.02 ± 0.03
0.875	0.06 ± 0.07	0.96 ± 0.06	1.42 ± 0.11	0.94 ± 0.06	0.06 ± 0.06
1.000	0.02 ± 0.05	1.29 ± 0.02	1.93 ± 0.06	1.27 ± 0.03	0.05 ± 0.05
1.125	0.08 ± 0.02	1.69 ± 0.05	2.51 ± 0.07	1.66 ± 0.04	0.09 ± 0.04
1.250	0.12 ± 0.03	2.16 ± 0.09	3.18 ± 0.14	2.11 ± 0.09	0.13 ± 0.03
1.375	0.26 ± 0.07	3.31 ± 0.03	4.79 ± 0.07	3.17 ± 0.06	0.18 ± 0.03
1.500	0.28 ± 0.04	3.84 ± 0.12	5.61 ± 0.18	3.73 ± 0.12	0.24 ± 0.06
1.625	0.29 ± 0.00	4.47 ± 0.12	6.49 ± 0.19	4.35 ± 0.13	0.30 ± 0.03
1.750	0.40 ± 0.07	5.24 ± 0.04	7.62 ± 0.09	5.07 ± 0.05	0.33 ± 0.03
1.875	0.45 ± 0.05	6.02 ± 0.12	8.72 ± 0.16	5.82 ± 0.09	0.39 ± 0.03
2.000	0.51 ± 0.02	6.85 ± 0.11	9.86 ± 0.17	6.57 ± 0.11	0.42 ± 0.05

Table B.6: Temperature increase at the five thermocouple positions across the supercapacitor stack, $\Delta \mathrm{T_i}$, relative to the temperature of approximately $30.0 \pm 0.1°\mathrm{C}$ during calibration, as the cycling current is increased stepwise from $0.250\,\mathrm{A}$ to $2.000\,\mathrm{A}$, during the third experiment of the B-series (B3)

Current $[A]$	$\Delta \mathrm{T}_1$ [°C]	$\Delta \mathrm{T}_2$ [°C]	$\Delta \mathrm{T}_3$ [°C]	$\Delta \mathrm{T}_4$ [°C]	$\Delta \mathrm{T}_5$ [°C]
0.250	-0.05 ± 0.03	-0.01 ± 0.04	0.00 ± 0.04	0.00 ± 0.03	-0.02 ± 0.03
0.375	-0.04 ± 0.03	0.07 ± 0.03	0.13 ± 0.03	0.10 ± 0.03	-0.01 ± 0.04
0.500	-0.02 ± 0.04	0.22 ± 0.04	0.35 ± 0.06	0.24 ± 0.05	-0.01 ± 0.03
0.625	-0.01 ± 0.02	0.41 ± 0.02	0.64 ± 0.02	0.44 ± 0.03	0.01 ± 0.03
0.750	0.01 ± 0.03	0.67 ± 0.06	1.00 ± 0.05	0.66 ± 0.04	0.02 ± 0.06
0.875	0.04 ± 0.06	0.96 ± 0.07	1.41 ± 0.12	0.92 ± 0.07	0.03 ± 0.03
1.000	0.05 ± 0.06	1.32 ± 0.03	1.94 ± 0.06	1.28 ± 0.04	0.06 ± 0.06
1.125	0.12 ± 0.04	1.77 ± 0.10	2.54 ± 0.09	1.68 ± 0.08	0.11 ± 0.03
1.250	0.14 ± 0.01	2.21 ± 0.08	3.20 ± 0.14	2.11 ± 0.09	0.14 ± 0.03
1.375	0.30 ± 0.04	3.35 ± 0.10	4.79 ± 0.16	3.17 ± 0.10	0.20 ± 0.03
1.500	0.30 ± 0.03	3.95 ± 0.10	5.64 ± 0.14	3.72 ± 0.07	0.23 ± 0.07
1.625	0.32 ± 0.01	4.64 ± 0.06	6.67 ± 0.12	4.39 ± 0.05	0.27 ± 0.06
1.750	0.39 ± 0.04	5.35 ± 0.13	7.64 ± 0.20	5.05 ± 0.13	0.32 ± 0.03
1.875	0.49 ± 0.05	6.18 ± 0.23	8.76 ± 0.33	5.80 ± 0.18	0.37 ± 0.03
2.000	0.53 ± 0.03	6.98 ± 0.12	9.93 ± 0.22	6.58 ± 0.14	0.41 ± 0.04

Table B.7: Temperature increase at the five thermocouple positions across the supercapacitor stack, ΔT_i, relative to the temperature of approximately $30.0 \pm 0.1°C$ during calibration, as the cycling current is increased stepwise from 0.250 A to 2.000 A, during the first experiment of the C-series (C1)

Current $[A]$	ΔT_1 [°C]	ΔT_2 [°C]	ΔT_3 [°C]	ΔT_4 [°C]	ΔT_5 [°C]
0.250	-0.02 ± 0.03	0.00 ± 0.04	0.02 ± 0.05	0.02 ± 0.06	-0.01 ± 0.03
0.375	-0.03 ± 0.03	0.05 ± 0.04	0.09 ± 0.04	0.09 ± 0.04	0.00 ± 0.03
0.500	-0.03 ± 0.03	0.16 ± 0.06	0.24 ± 0.05	0.22 ± 0.05	0.01 ± 0.03
0.625	-0.02 ± 0.03	0.33 ± 0.05	0.44 ± 0.06	0.37 ± 0.07	0.01 ± 0.03
0.750	0.00 ± 0.04	0.54 ± 0.04	0.72 ± 0.08	0.60 ± 0.05	0.05 ± 0.06
0.875	0.03 ± 0.07	0.80 ± 0.04	1.02 ± 0.07	0.83 ± 0.03	0.08 ± 0.04
1.000	0.02 ± 0.06	1.05 ± 0.05	1.36 ± 0.07	1.13 ± 0.05	0.09 ± 0.03
1.125	0.07 ± 0.03	1.42 ± 0.07	1.79 ± 0.05	1.45 ± 0.03	0.12 ± 0.01
1.250	0.09 ± 0.01	1.83 ± 0.01	2.30 ± 0.01	1.87 ± 0.06	0.16 ± 0.02
1.375	0.19 ± 0.08	2.76 ± 0.08	3.42 ± 0.08	2.74 ± 0.05	0.21 ± 0.01
1.500	0.19 ± 0.05	3.21 ± 0.20	4.01 ± 0.33	3.25 ± 0.18	0.30 ± 0.03
1.625	0.27 ± 0.03	3.80 ± 0.12	4.72 ± 0.19	3.84 ± 0.10	0.34 ± 0.02
1.750	0.28 ± 0.01	4.42 ± 0.02	5.52 ± 0.06	4.44 ± 0.05	0.37 ± 0.00
1.875	0.34 ± 0.01	5.12 ± 0.10	6.35 ± 0.15	5.12 ± 0.08	0.46 ± 0.01
2.000	0.42 ± 0.04	5.79 ± 0.06	7.20 ± 0.11	5.78 ± 0.05	0.50 ± 0.03

Table B.8: Temperature increase at the five thermocouple positions across the supercapacitor stack, $\Delta \mathrm{T_i}$, relative to the temperature of approximately $30.0 \pm 0.1°\mathrm{C}$ during calibration, as the cycling current is increased stepwise from $0.250\,\mathrm{A}$ to $2.000\,\mathrm{A}$, during the second experiment of the C-series (C2)

Current $[A]$	$\Delta \mathrm{T}_1$ [°C]	$\Delta \mathrm{T}_2$ [°C]	$\Delta \mathrm{T}_3$ [°C]	$\Delta \mathrm{T}_4$ [°C]	$\Delta \mathrm{T}_5$ [°C]
0.250	-0.05 ± 0.03	-0.04 ± 0.06	-0.02 ± 0.06	0.00 ± 0.05	-0.01 ± 0.02
0.375	-0.04 ± 0.03	0.04 ± 0.03	0.08 ± 0.03	0.09 ± 0.02	-0.01 ± 0.02
0.500	-0.01 ± 0.04	0.20 ± 0.03	0.26 ± 0.03	0.24 ± 0.02	0.02 ± 0.03
0.625	-0.01 ± 0.03	0.36 ± 0.03	0.45 ± 0.03	0.39 ± 0.04	0.02 ± 0.02
0.750	0.00 ± 0.07	0.55 ± 0.04	0.71 ± 0.07	0.59 ± 0.04	0.04 ± 0.06
0.875	0.05 ± 0.04	0.80 ± 0.02	1.02 ± 0.03	0.84 ± 0.03	0.09 ± 0.01
1.000	0.07 ± 0.04	1.12 ± 0.05	1.39 ± 0.04	1.14 ± 0.02	0.10 ± 0.03
1.125	0.10 ± 0.03	1.48 ± 0.05	1.85 ± 0.08	1.51 ± 0.05	0.15 ± 0.02
1.250	0.14 ± 0.03	1.86 ± 0.05	2.32 ± 0.07	1.89 ± 0.05	0.18 ± 0.01
1.375	0.19 ± 0.05	2.78 ± 0.04	3.44 ± 0.07	2.78 ± 0.07	0.27 ± 0.01
1.500	0.25 ± 0.02	3.32 ± 0.02	4.13 ± 0.03	3.33 ± 0.06	0.31 ± 0.02
1.625	0.30 ± 0.02	3.89 ± 0.07	4.83 ± 0.09	3.90 ± 0.04	0.35 ± 0.03
1.750	0.29 ± 0.04	4.44 ± 0.04	5.53 ± 0.08	4.45 ± 0.05	0.37 ± 0.03
1.875	0.34 ± 0.01	5.14 ± 0.06	6.37 ± 0.06	5.12 ± 0.04	0.43 ± 0.06
2.000	0.44 ± 0.05	5.85 ± 0.10	7.25 ± 0.12	5.82 ± 0.07	0.50 ± 0.03

Table B.9: Temperature increase at the five thermocouple positions across the supercapacitor stack, $\Delta \mathrm{T_i}$, relative to the temperature of approximately $30.0 \pm 0.1°\mathrm{C}$ during calibration, as the cycling current is increased stepwise from $0.250\,\mathrm{A}$ to $2.000\,\mathrm{A}$, during the third experiment of the C-series (C3)

Current $[A]$	$\Delta \mathrm{T}_1$ [°C]	$\Delta \mathrm{T}_2$ [°C]	$\Delta \mathrm{T}_3$ [°C]	$\Delta \mathrm{T}_4$ [°C]	$\Delta \mathrm{T}_5$ [°C]
0.250	-0.02 ± 0.05	0.00 ± 0.04	0.03 ± 0.04	0.03 ± 0.06	0.00 ± 0.02
0.375	-0.02 ± 0.04	0.06 ± 0.03	0.10 ± 0.03	0.10 ± 0.03	0.00 ± 0.03
0.500	0.00 ± 0.07	0.19 ± 0.05	0.26 ± 0.04	0.23 ± 0.04	0.01 ± 0.03
0.625	-0.01 ± 0.04	0.34 ± 0.03	0.45 ± 0.04	0.39 ± 0.05	0.02 ± 0.04
0.750	0.00 ± 0.03	0.55 ± 0.03	0.71 ± 0.07	0.59 ± 0.05	0.04 ± 0.05
0.875	0.06 ± 0.05	0.81 ± 0.03	1.04 ± 0.07	0.84 ± 0.04	0.08 ± 0.04
1.000	0.06 ± 0.04	1.09 ± 0.07	1.39 ± 0.06	1.14 ± 0.04	0.10 ± 0.04
1.125	0.08 ± 0.03	1.43 ± 0.07	1.81 ± 0.08	1.46 ± 0.06	0.13 ± 0.03
1.250	0.12 ± 0.01	1.85 ± 0.03	2.31 ± 0.03	1.87 ± 0.06	0.15 ± 0.02
1.375	0.15 ± 0.01	2.74 ± 0.06	3.43 ± 0.06	2.77 ± 0.05	0.27 ± 0.02
1.500	0.19 ± 0.04	3.26 ± 0.08	4.07 ± 0.12	3.28 ± 0.05	0.30 ± 0.02
1.625	0.28 ± 0.05	3.87 ± 0.09	4.81 ± 0.11	3.88 ± 0.05	0.34 ± 0.01
1.750	0.29 ± 0.03	4.44 ± 0.05	5.53 ± 0.09	4.45 ± 0.06	0.37 ± 0.01
1.875	0.36 ± 0.03	5.16 ± 0.06	6.39 ± 0.09	5.14 ± 0.07	0.47 ± 0.03
2.000	0.40 ± 0.07	5.81 ± 0.07	7.22 ± 0.07	5.79 ± 0.06	0.51 ± 0.03

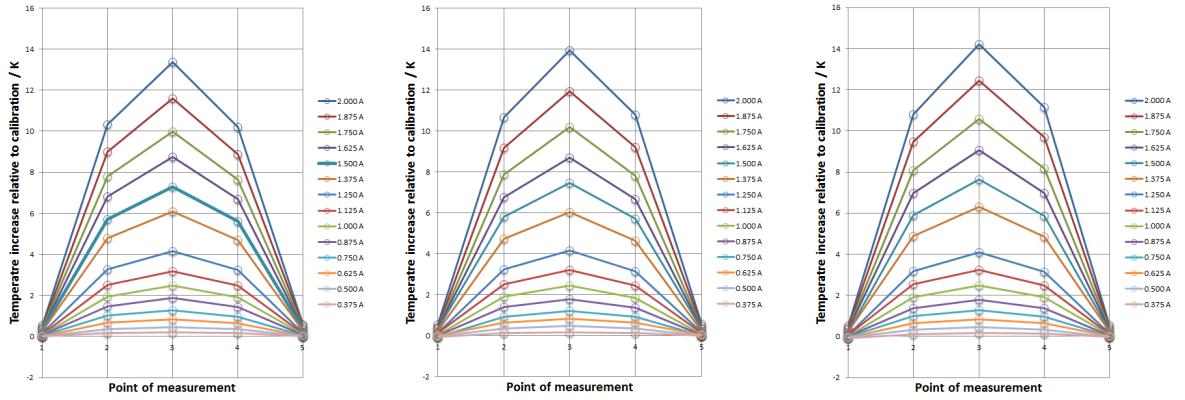

(a) Experiment A1 (b) Experiment A2 (c) Experiment A3

Figure B.35: Temperature increase at the five intrinsic and external positions of the thermocouples in the supercapacitor stack, ΔT_i, plotted as a function of their relative position between the respective supercapacitor units across the axial direction of the stack, at applied currents from $0.375\,\mathrm{A}$ to $2.000\,\mathrm{A}$, for the A series experiments.

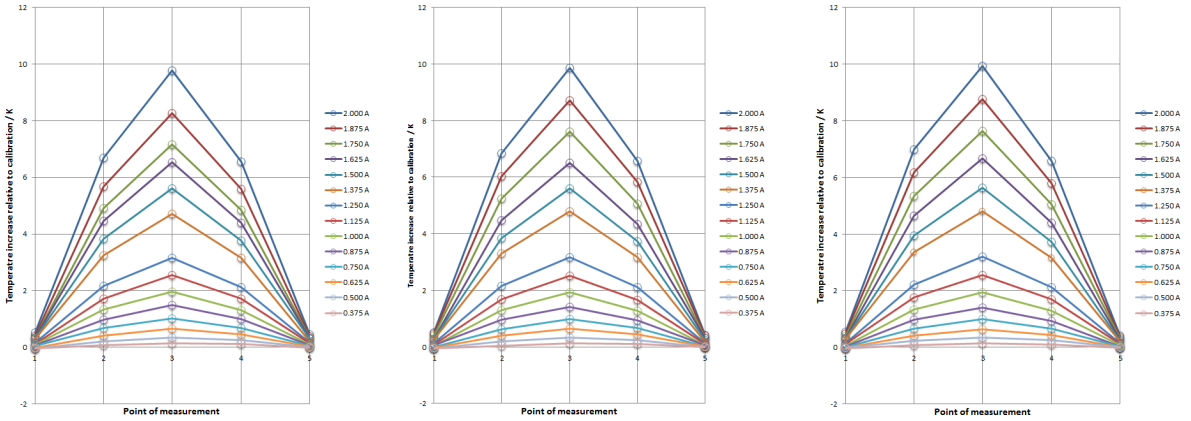

(a) Experiment B1 (b) Experiment B2 (c) Experiment B3

Figure B.36: Temperature increase at the five intrinsic and external positions of the thermocouples in the supercapacitor stack, ΔT_i, plotted as a function of their relative position between the respective supercapacitor units across the axial direction of the stack, at applied currents from $0.375\,\mathrm{A}$ to $2.000\,\mathrm{A}$, for the B series experiments.

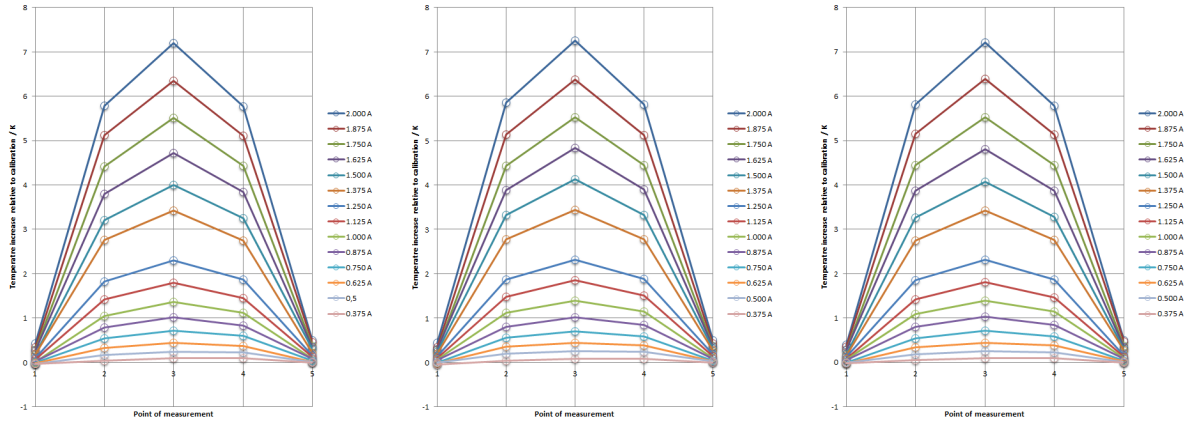

(a) Experiment C1 (b) Experiment C2 (c) Experiment C3

Figure B.37: Temperature increase at the five intrinsic and external positions of the thermocouples in the supercapacitor stack, ΔT_i, plotted as a function of their relative position between the respective supercapacitor units across the axial direction of the stack, at applied currents from $0.375\,\mathrm{A}$ to $2.000\,\mathrm{A}$, for the C series experiments.

B.2 Thermoelectric Module Experiments

B.2.1 Experiment On Isothermal Internal Ohmic Resistance

Table B.10: Overview of calculated average temperatures, $\overline{\mathrm{T}}$, measured temperatures at the hot and the cold side of the device, $\mathrm{T_h}$ and $\mathrm{T_c}$, and measured total ohmic resistance, R, graphically displayed in figure (3.6), with 95 % confidence interval values.

$\overline{\mathrm{T}}$	$\mathrm{T_h}$	$\mathrm{T_c}$	R
[°C]	[°C]	[°C]	Ω
20.038 ± 0.019	20.068 ± 0.053	20.008 ± 0.055	1.554 ± 0.021
22.044 ± 0.014	22.073 ± 0.042	22.015 ± 0.034	1.570 ± 0.028
23.992 ± 0.015	23.968 ± 0.041	24.016 ± 0.044	1.584 ± 0.005
26.029 ± 0.017	26.097 ± 0.056	25.962 ± 0.036	1.599 ± 0.026
27.956 ± 0.012	27.949 ± 0.031	27.964 ± 0.038	1.614 ± 0.021
29.971 ± 0.030	29.978 ± 0.113	29.964 ± 0.033	1.630 ± 0.011
32.025 ± 0.013	32.039 ± 0.041	32.012 ± 0.030	1.646 ± 0.005
34.027 ± 0.015	34.041 ± 0.049	34.014 ± 0.032	1.661 ± 0.007
35.954 ± 0.043	35.900 ± 0.166	36.009 ± 0.047	1.676 ± 0.013
37.990 ± 0.039	37.925 ± 0.151	38.054 ± 0.043	1.693 ± 0.017
40.054 ± 0.018	40.041 ± 0.052	40.067 ± 0.050	1.708 ± 0.017
42.052 ± 0.014	42.037 ± 0.034	42.066 ± 0.045	1.724 ± 0.012
43.958 ± 0.021	43.934 ± 0.075	43.983 ± 0.034	1.739 ± 0.022
45.961 ± 0.019	45.957 ± 0.071	45.964 ± 0.033	1.756 ± 0.004
47.977 ± 0.014	47.965 ± 0.045	47.990 ± 0.031	1.772 ± 0.026
49.923 ± 0.029	49.881 ± 0.107	49.965 ± 0.046	1.788 ± 0.020
51.999 ± 0.041	51.999 ± 0.155	51.999 ± 0.050	1.803 ± 0.018
54.048 ± 0.024	54.079 ± 0.088	54.016 ± 0.038	1.819 ± 0.017
56.081 ± 0.025	56.134 ± 0.094	56.029 ± 0.034	1.836 ± 0.019
58.069 ± 0.023	58.105 ± 0.084	58.034 ± 0.036	1.852 ± 0.017
60.058 ± 0.039	60.083 ± 0.150	60.033 ± 0.041	1.868 ± 0.014

Appendix C

Calibration of the Heaters

During previous work by Takla [2] and Hauge [1] it was evident that the sensitivity of the heaters of the calorimeter had to be improved. Two measures to obtain this was taken; an AC/DC signal calibration of the DC potential at the heaters compared to the AC signal read in the LabView setup, and also a calibration of the sensitivity of the heaters was carried out.

C.1 AC/DC Conversion Calibration

The effect applied to the heaters by the Eurotherm PID-controllers, through the resistive wires inside the heaters, are interpreted in the LabView setup as an AC potential squared divided by the ohmic resistance of the wire, $\mathrm{P} = \frac{\left(\mathrm{E}^{\mathrm{AC}}\right)^2}{\mathrm{R}}$. Before entering the LabView setup the AC potential is transformed into a DC potential, and a conversion parameter is therefore needed in order to determine the actual AC potential applied on the resistive wire. In order to determine the conversion parameters the effect from the heaters was increased stepwise from the minimum to the maximum effect, with intervals of 5 % of the total applicable effect, while measuring the AC potential in the circuit of the resistive wire with a Biltema multimeter, and regestering the corresponding DC potential displayed in the LabView setup. The AC potential conversion parameter, EAC, was obtained by plotting the actual measured AC potential as a function of the DC potential, E^{DC}, registered in the LabView setup, as presented in figure (C.1). This procedure was carried out for both heaters, heater A and B, and the obtained parameters are found as the slopes of the potential curves. The ohmic resistances were also measured with the Biltema multimeter, and found to be $10.4\,\Omega$ for heater A and $10.0\,\Omega$ for heater B. The actual effect applied by the heaters can hence be displayed equation (**??** and (**??** for heater A and

B, respectively.

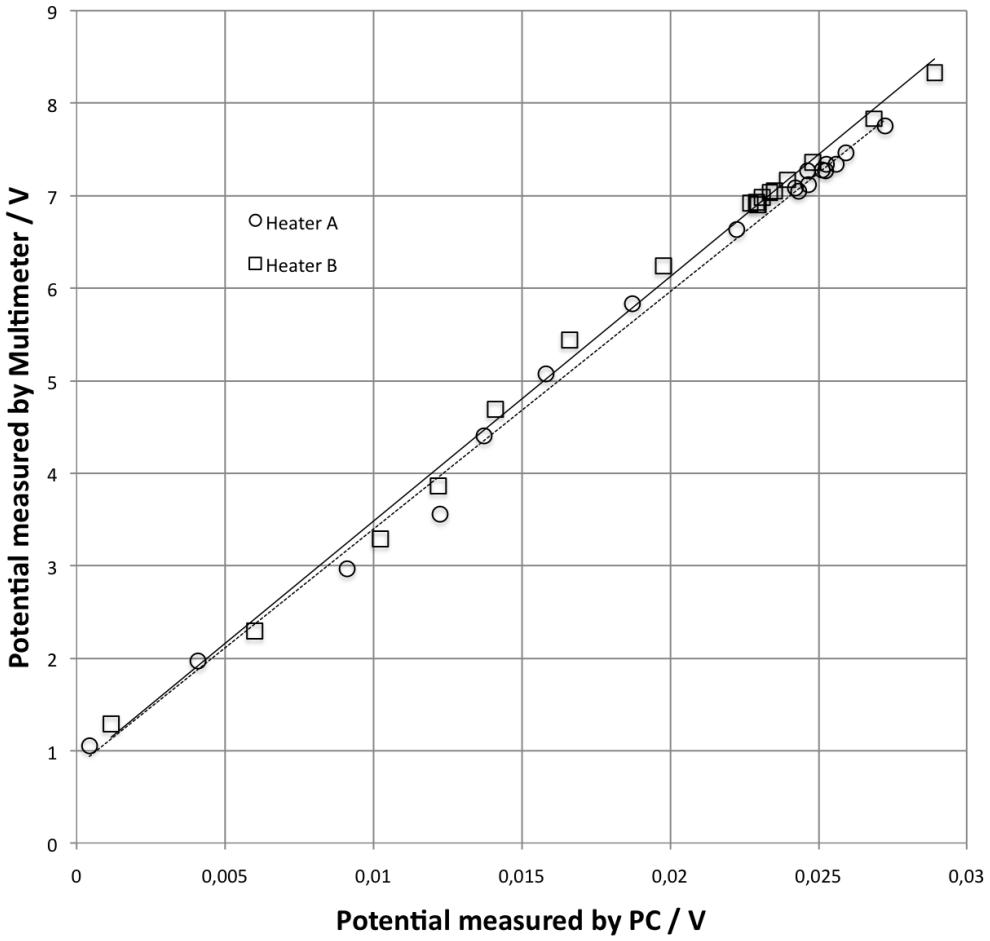

Figure C.1: Calibration of the AC to DC potential from the Eurotherm PID-controllers to the LabView setup.

$$P_A^{AC} = \frac{\left(256.6\, E^{DC} + 0.826\, V\right)^2}{10.4\,\Omega} \tag{C.1}$$

$$P_B^{AC} = \frac{\left(264.2\, E^{DC} + 0.835\, V\right)^2}{10.0\,\Omega} \tag{C.2}$$

C.2 Heat Sensitivity Calibration

The heat measured by the thermostatically controlled heaters, corresponding to the reduction in their applied potential to the resistive heating wires, was measured in response to the ohmic heat produced by a $10.42\,\Omega$ resistive wire sandwiched as a serpentine between the aluminium heating plates of the calorimeter when the PAR 263A applied current in a galvanostatic mode at an isothermal temperature of approximately $30\,^{\circ}\mathrm{C}$. This was done both for the total heat sensitivity of the two heaters combined, and also for each single heater, using a piece of expanded polyester to isolate the other heater while measuring the response from each single heater. The effect measured by the heaters was then compared to the ohmic heating from the sandwiched resistive wire, $\mathrm{Q_{ohmic}} = \mathrm{R\,I^2}$, through three calibrations at applied currents from $0.1\,\mathrm{A}$ to $0.6\,\mathrm{A}$, for one hour at each $0.1\,\mathrm{A}$ interval. The ratio of the average heat registered by the heaters divided by the actual ohmic heat applied to the heaters was hence determined. The heat measurements in the calorimetric studies of the supercapacitors and the thermoelectric module were adjusted, accordingly, to be equal to the measured heat divided by the obtained ratio of the measured heat compared to the applied heat, in order to determine the actual heat produced between the heaters. In the calorimetric studies of the supercapacitors the heat measurements are adjusted according to the ratio of the combined sensitivity of the two heaters, while in the calorimetric studies of the thermoelectric generators the heat sensitivity of each single heater had to be determined, as the heat flux through the device had to be determined. The plots of the ohmic heats applied to the resistive wire, and the corresponding absolute values of the decrease in potential applied to the resistive heating wires in the calorimeter are plotted as a function of the squared value of the current applied to the sandwiched resistive heating wire. The plot for the combined heat measurements are presented in figure (C.2), while the corresponding heat measurements for each single heater, heater A and B, is presented in figure (C.3) and (C.4), respectively. The heat ratios are obtained by dividing the average measured potential applied to the heaters by the average ohmic heat from the resistive heating wire, for applied currents between $0.3\,\mathrm{A}$ and $0.6\,\mathrm{A}$, where the heat is considered to be significant and the maximum effect of the heaters is still not reached. For the combined heat compensation of the two heaters, the heat ratio is found to be 0.4202, and for heater A and B, independently, the ratio is found to be 0.3782 and 0.4200, respectively.

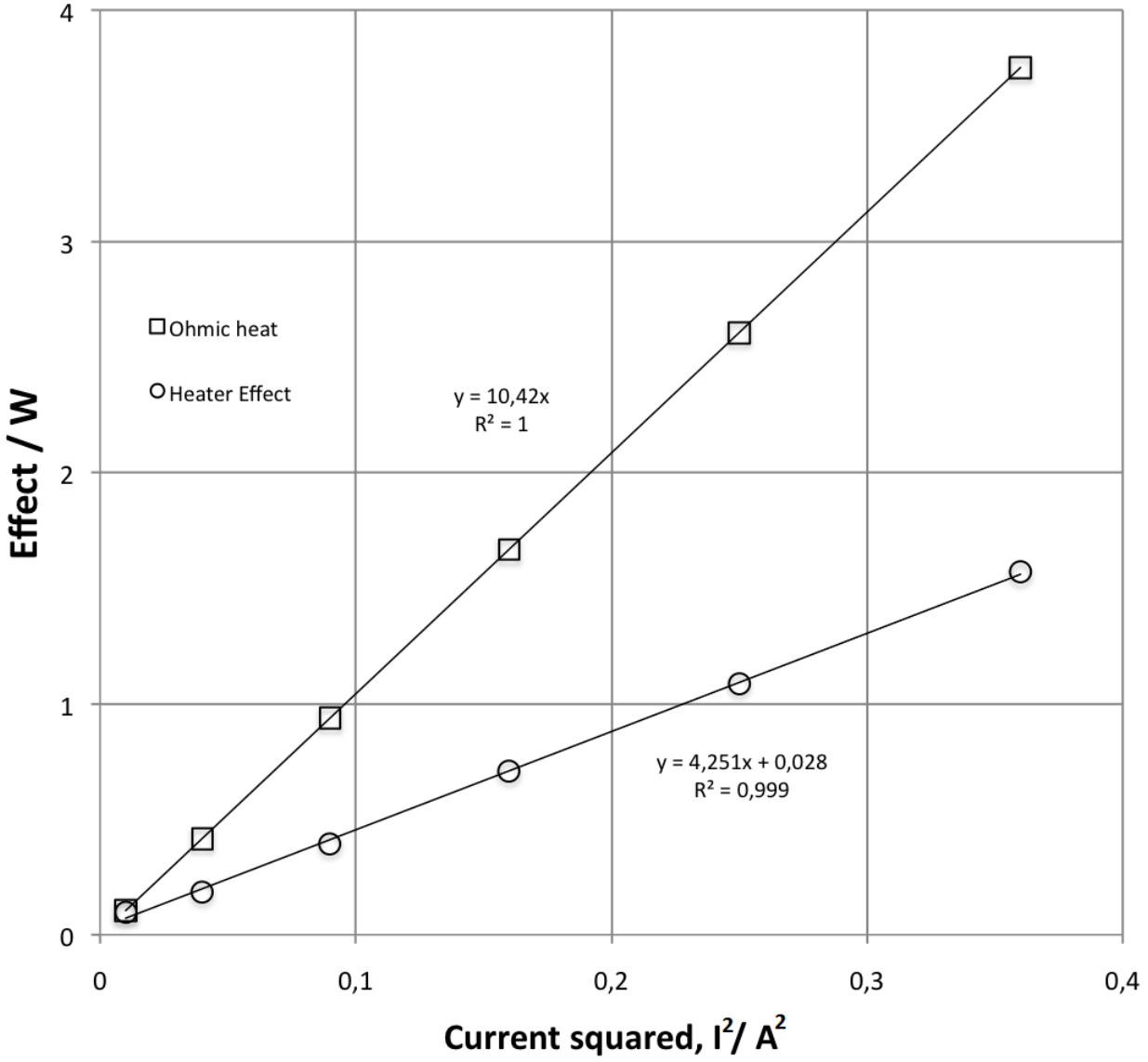

Figure C.2: The absolute value of the total effect applied to the two heaters and the corresponding ohmic heat applied from the resistive wire, $\mathrm{R\,I^2}$, plotted as a function of the applied current squared, $\mathrm{I^2}$.

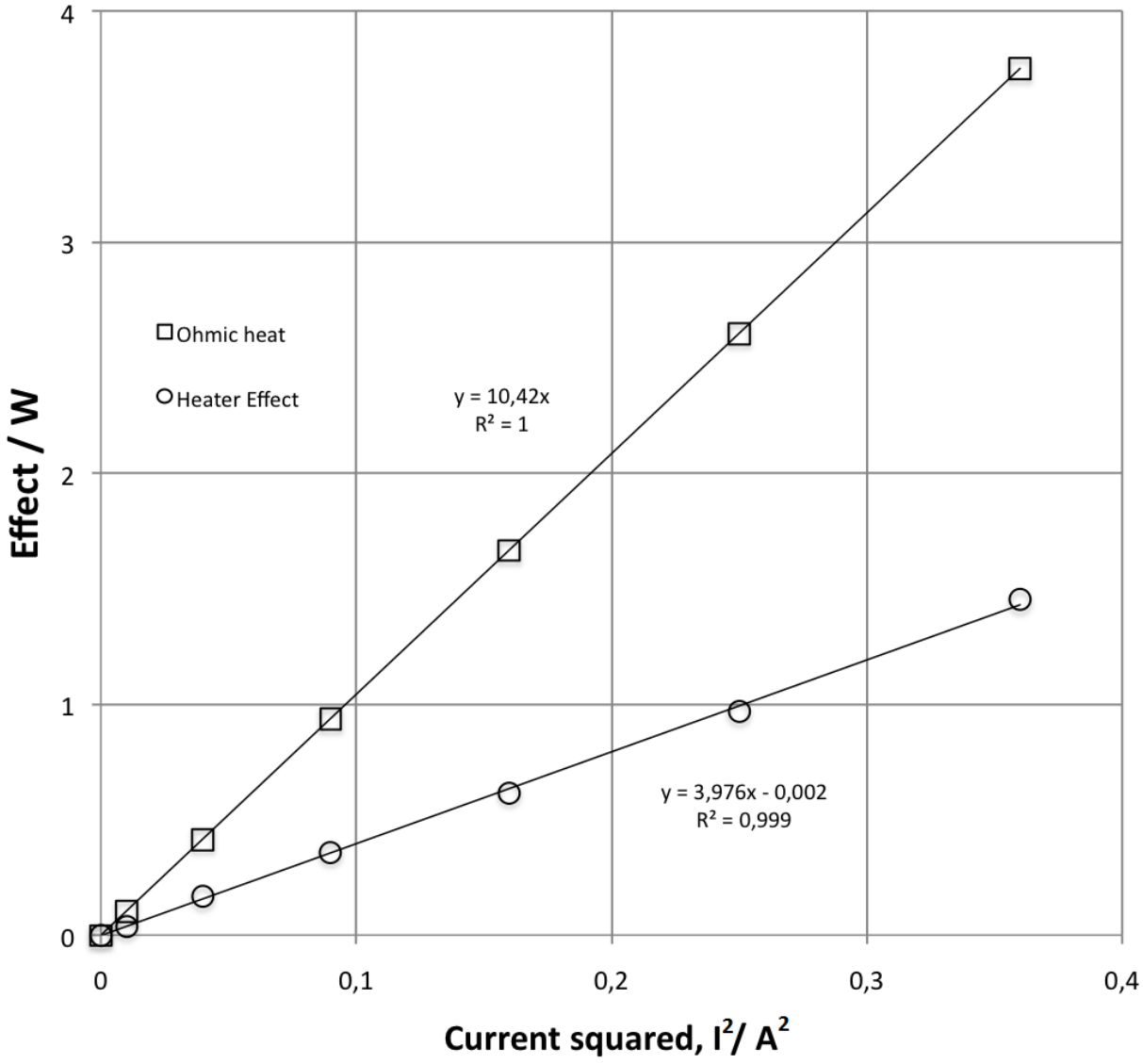

Figure C.3: The absolute value of the effect applied to heater A and the corresponding ohmic heat applied from the resistive wire, $\mathrm{R\,I^2}$, plotted as a function of the applied current squared, $\mathrm{I^2}$.

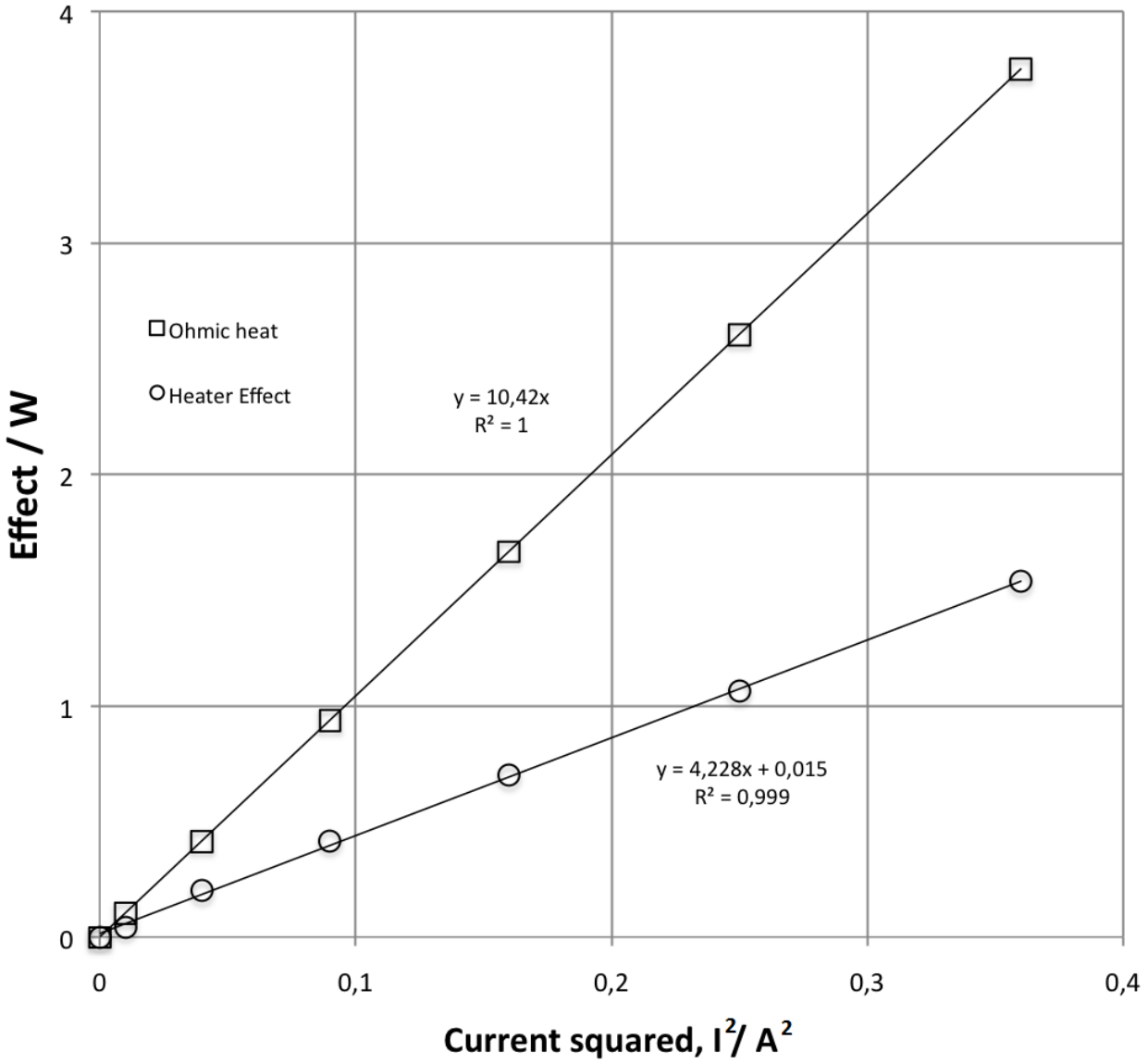

Figure C.4: The absolute value of the effect applied to heater B and the corresponding ohmic heat applied from the resistive wire, $\mathrm{R\,I^2}$, plotted as a function of the applied current squared, $\mathrm{I^2}$.

Appendix D

Evaluation of Risk of the Experimental Procedures

The schemes of risk evaluation concerning the experimental work carried out in the lab (Skjema for Sikker Jobb Analyse (SJA)) are presented in figure (D.1) and (D.2) in order to give information on the safety of the experiments.

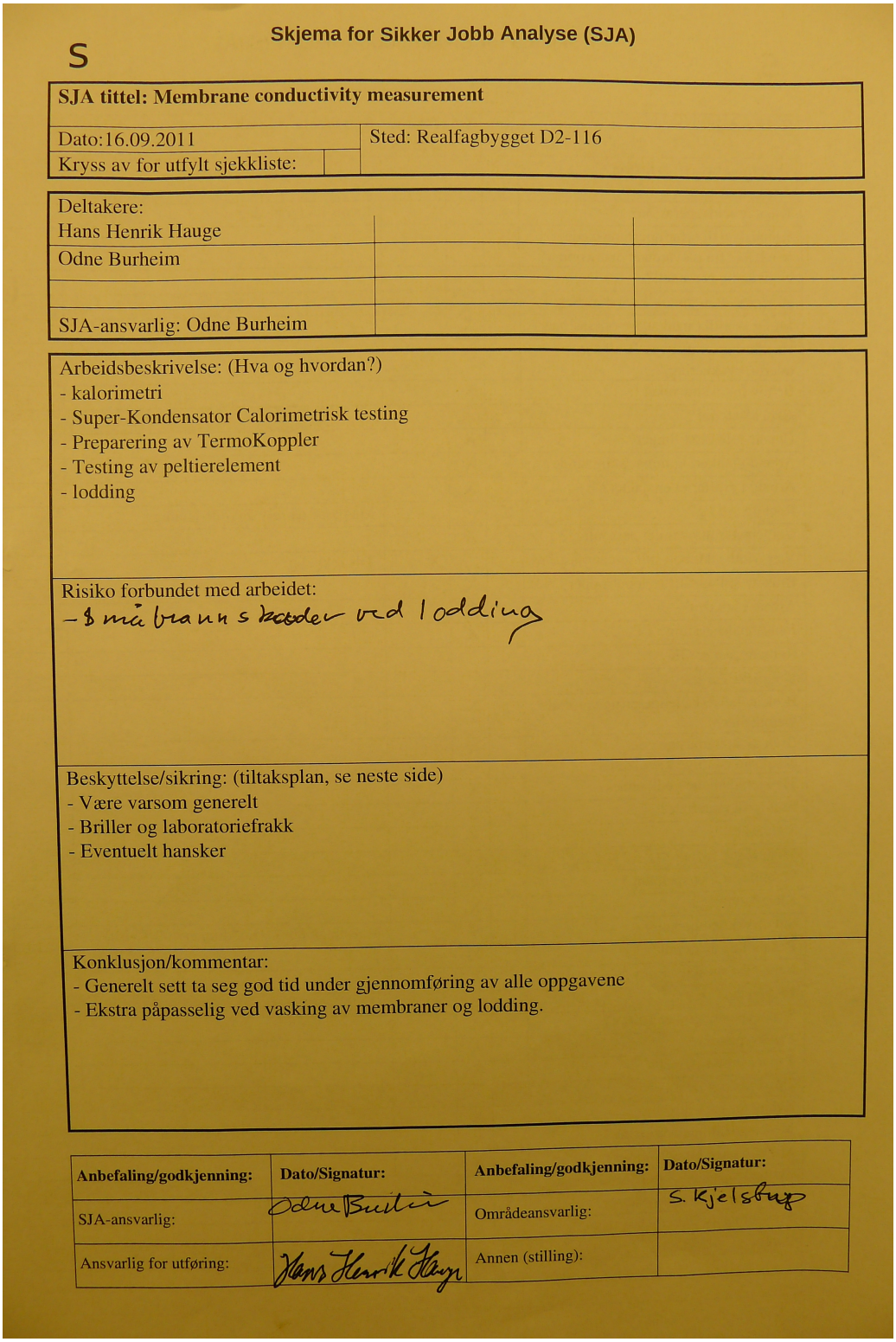

S

Skjema for Sikker Jobb Analyse (SJA)

SJA tittel: Membrane conductivity measurement	
Dato: 16.09.2011	Sted: Realfagbygget D2-116
Kryss av for utfylt sjekkliste:	

Deltakere:		
Hans Henrik Hauge		
Odne Burheim		
SJA-ansvarlig: Odne Burheim		

Arbeidsbeskrivelse: (Hva og hvordan?)
- kalorimetri
- Super-Kondensator Calorimetrisk testing
- Preparering av TermoKoppler
- Testing av peltierelement
- lodding

Risiko forbundet med arbeidet:
- Småbrannskader ved lodding

Beskyttelse/sikring: (tiltaksplan, se neste side)
- Være varsom generelt
- Briller og laboratoriefrakk
- Eventuelt hansker

Konklusjon/kommentar:
- Generelt sett ta seg god tid under gjennomføring av alle oppgavene
- Ekstra påpasselig ved vasking av membraner og lodding.

Anbefaling/godkjenning:	Dato/Signatur:	Anbefaling/godkjenning:	Dato/Signatur:
SJA-ansvarlig:	Odne Burheim	Områdeansvarlig:	S. Kjelstrup
Ansvarlig for utføring:	Hans Henrik Hauge	Annen (stilling):	

Figure D.1: Page 1/2 of the scheme, in Norwegian, for evaluation of the risks concerning the experimental procedures of the lab work (Skjema for Sikker Jobb Analyse (SJA)).

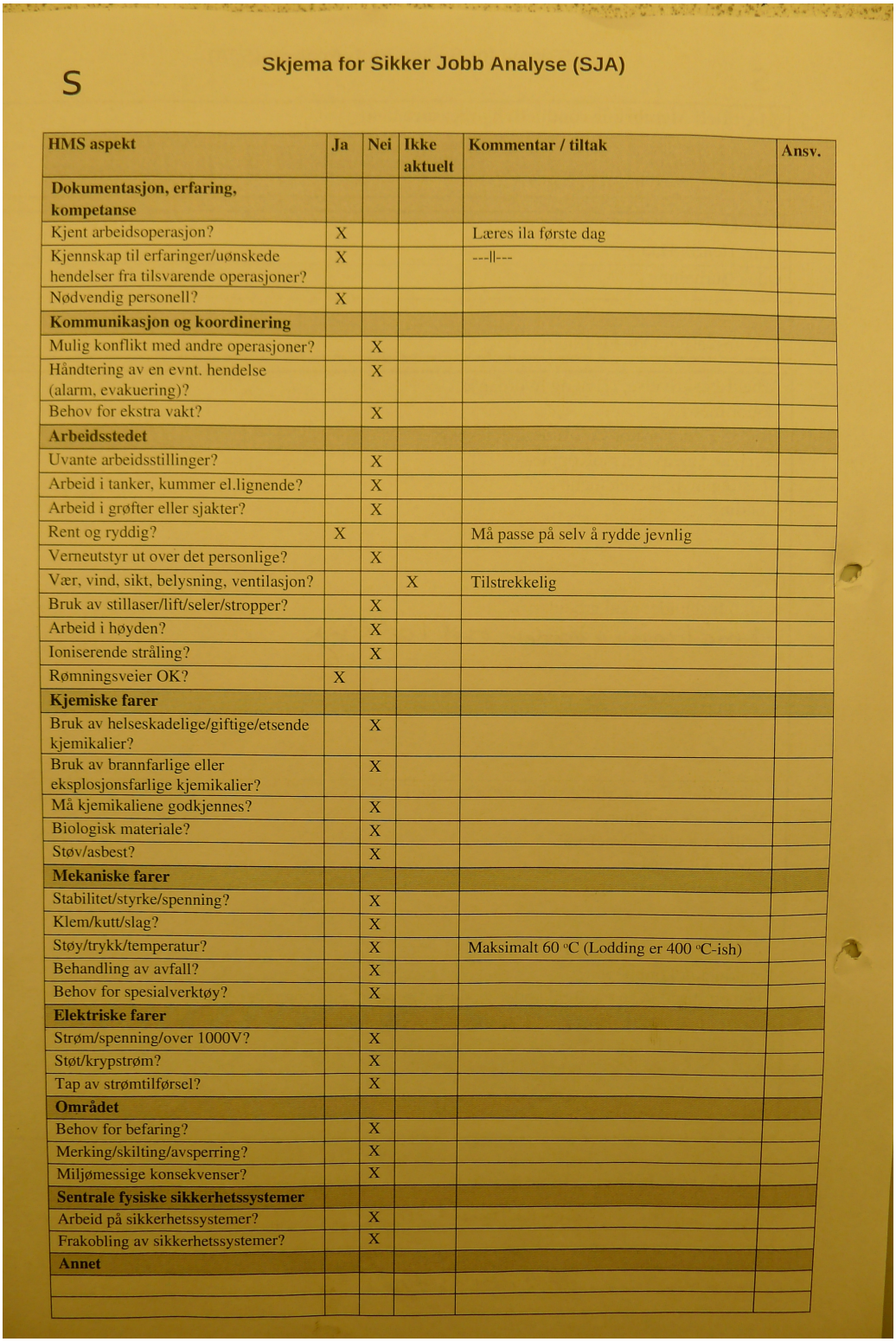

S

Skjema for Sikker Jobb Analyse (SJA)

HMS aspekt	Ja	Nei	Ikke aktuelt	Kommentar / tiltak	Ansv.
Dokumentasjon, erfaring, kompetanse					
Kjent arbeidsoperasjon?	X			Læres ila første dag	
Kjennskap til erfaringer/uønskede hendelser fra tilsvarende operasjoner?	X			---||---	
Nødvendig personell?	X				
Kommunikasjon og koordinering					
Mulig konflikt med andre operasjoner?		X			
Håndtering av en evnt. hendelse (alarm, evakuering)?		X			
Behov for ekstra vakt?		X			
Arbeidsstedet					
Uvante arbeidsstillinger?		X			
Arbeid i tanker, kummer el.lignende?		X			
Arbeid i grøfter eller sjakter?		X			
Rent og ryddig?	X			Må passe på selv å rydde jevnlig	
Verneutstyr ut over det personlige?		X			
Vær, vind, sikt, belysning, ventilasjon?			X	Tilstrekkelig	
Bruk av stillaser/lift/seler/stropper?		X			
Arbeid i høyden?		X			
Ioniserende stråling?		X			
Rømningsveier OK?	X				
Kjemiske farer					
Bruk av helseskadelige/giftige/etsende kjemikalier?		X			
Bruk av brannfarlige eller eksplosjonsfarlige kjemikalier?		X			
Må kjemikaliene godkjennes?		X			
Biologisk materiale?		X			
Støv/asbest?		X			
Mekaniske farer					
Stabilitet/styrke/spenning?		X			
Klem/kutt/slag?		X			
Støy/trykk/temperatur?		X		Maksimalt 60 °C (Lodding er 400 °C-ish)	
Behandling av avfall?		X			
Behov for spesialverktøy?		X			
Elektriske farer					
Strøm/spenning/over 1000V?		X			
Støt/krypstrøm?		X			
Tap av strømtilførsel?		X			
Området					
Behov for befaring?		X			
Merking/skilting/avsperring?		X			
Miljømessige konsekvenser?		X			
Sentrale fysiske sikkerhetssystemer					
Arbeid på sikkerhetssystemer?		X			
Frakobling av sikkerhetssystemer?		X			
Annet					

Figure D.2: Page 2/2 of the scheme, in Norwegian, for evaluation of the risks concerning the experimental procedures of the lab work (Skjema for Sikker Jobb Analyse (SJA)).